A thesis submitted for the degree of Doctor of Philosophy

Fluorescent nanodiamonds for nanosensing and single-molecule imaging

Maabur Sow

Linacre College

17th February 2021

In memory of my mother, Mathel Ba,
whose countless sacrifices allowed me to do this PhD

Abstract

Unlike ensemble measurements where individual behaviours are averaged and therefore inaccessible, single-molecule microscopy allows researchers to obtain real-time information about a biomolecule's intracellular localisation, interactions or conformational changes. The observation time of individual biomolecules, typically a few seconds to a few minutes, depends on the photostability of the fluorescent molecules used as imaging probes. The limitation of the observation time prevents us to gain precious insight on long-term individual biomolecular behaviours as biological processes like bacterial cell division take at least 20 minutes to occur.

The fluorescent nitrogen-vacancy defect in nanodiamond (ND) can emit light for hours and is an established nanoscale probe for quantum sensing (*e.g.*, magnetometry); as a result, there has been much interest in using NDs in biological imaging. Nevertheless, the implementation of fluorescent NDs (FNDs) in single-molecule imaging has been limited by the lack of single-molecule characterisation methods and the low brightness of 10-nm FNDs.

In this thesis, we first report the development of a photophysical characterisation method for FNDs down to 5-10 nm in size and present the discovery of the 10-nm ND's potential as direct pH nanosensors. We then pursue the establishment of a new characterisation technique for diffusing NDs and describe an innovative routine to estimate the proportion of FNDs among all the NDs. An optimised biofunctionalisation approach is detailed, thus allowing us to perform *in vitro* single-molecule work with the smallest conjugated FNDs ever manufactured (10-15 nm). Finally, we explore the application of these small functionalised FNDs for quantum sensing and present *in vivo* experiments using conjugated FNDs in bacteria.

Statement of Originality

I declare that the work detailed in this thesis is my own. Any contributions made to this project by my collaborators is explicitly acknowledged in the text (in materials and methods or in captions). The pronoun 'we' is used instead of 'I' throughout this thesis for stylistic reasons, although the latter would be more accurate. The major contributions to this thesis include:

-Oliver Williams, Laia Ginés and Soumen Mandal prepared the surface termination of the detonation nanodiamonds and the 50-nm high-pressure high-temperature nanodiamonds used in chapters 3 and 4.

-Barak Gilboa and Horst Steuer wrote the localisation and tracking software for the analysis of nanodiamonds presented in chapters 3 and 4.

-Shazeaa Ishmael took the optically detected magnetic resonance measurements on raw and functionalised nanodiamonds shown in chapter 6.

Acknowledgment

First, I would like to thank my supervisor Achillefs N. Kapanidis for giving me the opportunity to do my Dphil in his laboratory. His kindness and passion for science are inspirations to me both as a scientist and a person. I am very grateful to everyone in the Kapanidis group especially Barak Gilboa and Horst Steuer with whom I collaborated closely.

The help provided by Jason Smith and his team (Oxford materials), Shazeaa Ishmael and Sanmi Adekanye in particular, on the photophysical characterisation of nanodiamonds was very helpful. I am also thankful to Oliver Williams (Cardiff University) whose laboratory prepared many nanodiamonds samples for me and happily advised whenever I needed.

This research project would also not have been possible without the dedicated staff of the condensed matter physics sub-department and the diamond science and technology doctoral training centre especially Mark Newton, Julie Macpherson, Claire Hurley, Yasmin Kosar and Brian Patton. I would like to thank the EPSRC for their generous financial support.

Finally, great thanks to my remarkable family, my precious friends from college and the CDT, Angelina, Romain and Laura for their love and socially distant support.

Dissemination

Publications:

- M. Sow, H. Steuer, B. Gilboa, S. Adekanye, L. Gines, S. Mandal, O. A. Williams, J. M. Smith, A. N. Kapanidis. High-throughput nitrogen-vacancy center imaging for nanodiamond photophysical characterization and pH nanosensing. Nanoscale, 2020, 12, 21821-21831.

- B. Gilboa, B. Jing, T. Cui, centerM. Sow, A. Plochowietz, A. Mazumder, and A. N. Kapanidis. Confinement-free wide-field ratiometric tracking of single fluorescent molecules. The Biophysical Journal, 2019, 117, 2141–2153.

Conference Presentations:

- M. Sow, H. Steuer, A. Mazumder, L. Ginés, S. Mandal, O. A. Williams, A. N. Kapanidis. Single Nitrogen-vacancy Imaging in Nanodiamonds for Multimodal Bio-Sensing. Diamond Conference (Coventry, UK) July 2019.

- M. Sow, H. Steuer, B. Gilboa, S. Adekanye, L. Gines, S. Mandal, O. A. Williams, J. M. Smith, A. N. Kapanidis. Single Nitrogen-Vacancy Imaging in Nanodiamonds for Multimodal Sensing. Biophysical society meeting (Baltimore, USA) March 2019.

- M. Sow, H. Steuer, S. Adekanye, L. Gines, O. Williams, J. M. Smith, A. N.

Kapanidis. High-Throughput Photophysical Characterisation of Nanodiamonds. De Beers Diamond Conference (Coventry, UK) July 2018.

- M. Sow, B. Gilboa, L. Gines, O. Williams, A. Kapanidis. Size and Photophysical Characterisation of Nanodiamonds Using Fluorescence Wide-field Single-particle Imaging. PicoQuant International Workshop on "Single Molecule Spectroscopy and Super-resolution Microscopy in the Life Sciences" (Berlin, Germany) September 2017.

Conference Posters:

- M. Sow, H. Steuer, S. Adekanye, L. Gines, O. Williams, J. M. Smith, A. N. Kapanidis. High-Throughput Photophysical Characterisation of Nanodiamonds. Oxford photonics day (Oxford, UK) April 2018.

- M. Sow, B. Gilboa, L. Gines, O. A. Williams and A. Kapanidis. Characterisation of Size and Fluorescence Properties of Nanodiamonds Using Single-particle Imaging. De Beers Diamond Conference (Coventry, UK) July 2017.

Award:

- Arthur H. Cooke Memorial Prize for the best 1st year of DPhil in the condensed matter physics sub-department.

Contents

List of abbreviations

- AFM: atomic force microscopy
- bp: base pair
- CVD: chemical vapor deposition
- Cy3: indocarbocyanine
- DLS: dynamic light scattering
- DND: detonation nanodiamond
- *E. coli*: *Escherichia coli*
- EDC: 1-ethyl-3-(-3-dimethylaminopropyl) carbodiimide hydrochloride
- FND: nanodiamonds containing at least one NV centre
- HEPES: 4-(2-hydroxyethyl)-1-piperazineethanesulfonic acid
- HMM: Hidden Markov Model
- HPHT: high-pressure high-temperature
- MES: 2-[N-morpholino]ethane sulfonic acid
- MSD: mean square displacement

- ND: nanodiamond
- NHS: N-hydroxysuccinimide
- NV: nitrogen-vacancy centre
- ODMR: optically detected magnetic resonance
- PBS: phosphate buffered saline
- PSF: point-spread function
- R/G ratio: red/green ratio
- RNAP: RNA-Polymerase, the holoenzyme unless specified
- *S. cerevisiae*: *Saccharomyces cerevisiae*
- SD: standard deviation
- SPT: single-particle tracking
- TEM: transmission electronic microscopy
- TGF-β: transforming growth factor-beta
- ZFS: zero-field splitting
- ZPL: zero-phonon line

Chapter 1

Introduction

To gain an accurate understanding of biological processes, it is essential to observe and manipulate the fundamental units making the machinery of life: biomolecules. Investigating the interactions between such molecules (*e.g.,* DNA and proteins) can not only expand our knowledge of biology but can also lead to new technologies and therapies. In the past century, the fields of biochemistry, molecular biology and biophysics have all greatly expanded our knowledge and technology. For instance, the discovery of the Taq polymerase in bacteria led to the development of the polymerase chain reaction, which has revolutionized the way we study gene expression and is now commonly used in clinical and forensic science [1]. One issue with most of the current techniques used in molecular biology are based on the measurement of a signal (*e.g.,* fluorescence) originating from an ensemble of molecules. The averaging of the signal originating from individual molecules causes loss of precious information as biomolecules can exhibit quite heterogeneous or dynamic behaviour. Techniques to study individual molecules include atomic force microscopy [2, 3] and different types of transmission electron microscopy (*e.g.,* cryogenic electron microscopy) [4, 5, 6] but to explore the dynamic behaviour of biomolecules techniques like patch clamp, optical tweezers and

single-molecule fluorescence microscopy are usually preferred [7, 8, 9, 10]. Each of these techniques exploits different physical effects generated by individual molecules (*e.g.,* electrical current, force or fluorescence), thus providing complementary information on the dynamic structure of biomolecules. Single-molecule imaging has recently gained popularity as it is a versatile technique and offers the possibility to study the activity and localisation of biomolecules in their native environment (*i.e.* live cell) [11, 12, 13]. For example, through single-molecule imaging, Uphoff *et. al* were able to track individual enzymes repairing DNA inside living cells and measure kinetic information such as the duration of a single DNA repair event [14].

The implementation of single-molecule imaging involves three important steps. The first one is to label the biomolecule of interest with a single fluorophore such as an organic molecule or a quantum dot. The second step is to image the fluorescent probes with an extra dimension that permits us to distinguish single emitters within a diffraction-limited spot. The extra dimension could be the excitation wavelength or the time at which the fluorophores are photoactivated [15, 16]. Finally, super-resolution is achieved by fitting the fluorescence distribution to localise its centroid with a typical accuracy of 50 nm in the XY plane. The more photons are collected from the probe, the better the accuracy will be and that is why the choice of the probe is paramount in single-molecule imaging experiments.

Organic fluorophores make very bright probes and are commonly used in super-resolution imaging especially due to their photo-switchable properties [17]. However, their photostability is low compared to quantum dots, which is an important feature in single-molecule tracking experiments. For this reason, quantum dots are better suited to long tracking experiments (up to a few minutes) and have become popular probes [18]. Nonetheless, working with such nanoparticles can be challenging because of the intermittency of their fluorescence, which limits time resolution and may cause the loss

of relevant information in live cell single-molecule tracking. Furthermore, being made of semiconductors (*e.g.,* cadmium) the particles may be toxic to the cell and need to be encapsulated, which makes their bio-conjugation more complex [19]. The need to address these limitations has led to many improvements including non-blinking quantum dot [20] and the discovery of a new type of nanocrystal that shows great potential in bioimaging: fluorescent nanodiamonds (FNDs). FNDs have gained a growing interest over the past decade owing to their remarkable photostability, rich coupling chemistry and biocompatibility [21, 22, 23]. Moreover, the fluorescent defect inside nanodiamonds (*i.e.* the nitrogen vacancy) has a unique electronic structure, which can be harnessed to measure, with nanotesla precision, the magnetic field in its nano-environment (for more details see chapter 6 on page 89) [24, 25, 26].

The goal of this PhD project is to use FNDs to probe the nano-environment and study biomolecular interactions at a single-molecule level. First, this thesis will give an overview of the use of FNDs in bioimaging and bio-sensing. Secondly, the FNDs will be characterised in the context of single-molecule imaging (size and photophysics) thus revealing their potential as pH sensing probes. Finally, the bio-functionalisation of small FNDs is reported as well as *in vivo* single-particle experiments with a view to using functionalised FNDs for gene transcription studies.

Chapter 2

Nanodiamonds as fluorescent probes

2.1 Single-molecule microscopy

Since the works of Robert Hooke, Antonie van Leeuwenhoek and Marcello Malpigi in the 17th century, light microscopy has been an essential technique for biologists to investigate the inner working of living organisms [27]. Following such seminal studies of microscopic structures and organisms, microscopy has been very much improved in terms of resolution, one of the most crucial characteristics of the instrument; nevertheless, until the end of the 20th century light microscopists were generally limited to a lateral resolution of approximately 250 nm [28].

The resolution of a microscope can be defined by the minimal distance at which two point sources can be distinguished. Each point sources appear as diffraction patterns (a.k.a. Airy pattern) when imaged by the microscope because light diffracts when going through a lens. The size of the Airy pattern is different for each microscope and because it describes how a point-light source is imaged by the optical system the term point-spread function (PSF) is generally used when referring to the diffraction pattern. Reducing the size of the PSF is the main strategy to improve the resolution of the

imaging system but there is a limit on how small the distance between two resolvable point-light sources can be; this is the diffraction limit and it was discovered by Ernst Abbe at the end of the 19th century:

$$d = \frac{\lambda}{2n \sin \theta} \tag{2.1}$$

Where d is the estimated resolution, λ is the wavelength and $nsin\theta$ is the numerical aperture of the objective. The diffraction limit was overcome about three decades ago using very innovative approaches to physical chemistry, optics and image processing [9, 16, 17, 29]. Imaging techniques that offer sub-diffraction capabilities are named super-resolution microscopies; the most powerful of far field super-resolution techniques can be split into two types: deterministic and stochastic. The deterministic techniques rely on the physical reduction of the PSF using non-linear response of fluorophores to excitation, while stochastic techniques generally exploit the stochastic photophysical and/or photochemical behaviour of some fluorophores to temporally control their emission so they can be localised. Deterministic techniques generate microscopy images with resolutions inferior to 250 nm (*e.g.* 70 nm in the XY plane), whereas stochastic super-resolution provides maps representing the localisations of fluorophores in the field of view; the localisation accuracy of the fluorophore is smaller than the diffraction limit (typically 40 nm in the XY plane). Such type of super-resolution approach can be also termed in most of the cases, localisation microscopy, where single-molecule microscopy is one of the most common subtypes. The power of single-molecule imaging lies in its ability to not only give access to an accurate localisation of a fluorescently labelled biomolecule but also to its dynamical behaviour (*i.e.* conformational changes or molecular interaction) *in vitro* and *in vivo* [30, 31, 32].

Single-molecule imaging relies on the efficient labelling of a biomolecule of interest

with a fluorescent probe. The photophysical properties of the probe (*i.e.* brightness and photostability) are crucial as they will determine what localisation accuracy, time resolution and observation time can be achieved. For instance, the precision of the localisation can be estimated by the following equation [33]:

$$\Delta^2 = \frac{\sigma^2 + \frac{a^2}{12}}{N}\left(\frac{16}{9} + 4\tau\right) \tag{2.2}$$

Where τ is approximately the ratio between the background intensity and the peak signal intensity, σ is the standard deviation from the fit, a is the pixel size, and N is the total photon count. The total amount of photons collected during the acquisition is also termed the photon budget and the larger the photon budget is, the higher the time resolution, observation time and the localisation accuracy will be. One can therefore appreciate the importance of the photostability of the fluorescent probes as it defines how large the photon budget will be.

Small organic molecules ($\backsim$1 nm) such as members of the cyanine family make very bright probes that can be observed up to several minutes with a 200 ms time resolution [34]. For this reason, organic fluorophores are the best option when one wants to perform single-molecule imaging *in vitro*. Nevertheless, biologists ought to observe biomolecules for longer than a few minutes and the limited photostability of organic molecules does not permit such investigations unless more sophisticated approaches are implemented (*e.g.,* DNA paint) [35]. Exploring for longer periods is important as biomolecules may exhibit dynamical behaviour that requires long observation time (>20 min), as processes inside living cells can take up to 20 minutes to occur such as cell division in *Escherichia coli* [36].

The search for more photostable probes led to the development of a new type of probes: fluorescent nanoparticles. Thanks to their superior brightness and tuneable emission spectra, quantum dots (QD) were the first type of inorganic fluorescent par-

ticles used for bioimaging (see table 2.1). These semiconductor nanoparticles are very common probes and have been used for single-molecule imaging to track biomolecules for minutes in living cells [18]. One of the limitations of quantum dots for single-molecule tracking is the intermittency of their fluorescence, which can limit the time resolution and cause the loss of important information during tracking. Despite the great improvements made on quantum dots to reduce the off time (*i.e.* when a quantum dot does not emit light), other nanoparticles were developed to obtain better probes in terms of size, brightness, emission spectra and blinking such as upconversion nanocrystals, carbon dot, polymer dots and fluorescent nanodiamonds (FNDs) [37]. FNDs (above 35 nm in diameter) have the advantage of being biocompatible and showing no photobleaching nor blinking (see table 2.1). Further, unlike other fluorescent nanoparticles, they offer nanosensing capabilities of temperature and magnetic fields. The possibility to perform nanosensing originates from the unique electronic structure of a fluorescent crystal defect in nanodiamonds (NDs): the nitrogen-vacancy (NV) centre. There are other promising fluorescent defects available in diamond such as the silicon vacancy that shows a very narrow emission band but currently NV-centre-containing nanodiamonds are easier to manufacture [38].

A wider implementation of NDs in bioimaging is currently limited by their tendency to aggregate and the low brightness of sub-20-nm particles. The loss of colloidal stability in cell media or biochemistry buffer solutions can be managed by changing the surface chemistry of the NDs [39, 40, 41] although we will show in this thesis that this is not always required (see chapter 5 on page 66). If the problem of aggregation can be managed with chemistry, the limited brightness of the sub-20-nm FNDs is still a significant challenge when one wants to track single-molecules. Indeed, when imaging 10-20-nm FNDs using imaging conditions that are typically used for organic fluorophores (0.1 -1 kW/cm^2 at 20 Hz), small FNDs will appear 10 times dimer than a fluorophore. This

is due to the low number of NV centres per ND (1 or 2) and the low absorption cross section of the defect (see table 2.1). One solution is to use 30-100 nm NDs containing up to 900 NV centres per particle that would appear brighter than organic fluorophores. The other solution is to optimise the imaging conditions so small FNDs can be confidently distinguished from background signals such as cell fluorescence. For instance, the unique electronic structure of the NV centre is such that microwaves can be used to generate background free images [42, 43]. In this thesis, we rather used a high photon collection efficiency microscope coupled with a spectral ratiometric approach to detect small FNDs in cells.

Even though a single NV centre would appear dimer than a single fluorophore with an irradiance of 0.1 -1 kW/cm^2 at 20 Hz, it is worth noting that such irradiance is far from the saturation of the NV centre (>70 kW/cm^2) [44, 45]. It is therefore possible to obtain more photons from the NV centre using a higher irradiance, which will bleach in seconds most of the fluorescent molecules as reported by Fu *et al.* [21]. Higher irradiance could cause phototoxicity when performing continuous live cell imaging for several minutes but not for *in vitro* work and fixed cells.

This thesis will focus more on single-molecule imaging using NV centre in NDs (for more details see 2.4 on page 26), but there have been quite a few reports of super-resolution imaging using FNDs or NV centres in bulk diamond. For instance, Tzeng *et al.* reported a 40-nm lateral resolution using a deterministic technique termed stimulated emission depletion microscopy (STED) [46]. Most of the super-resolution reports on NDs are using stochastic techniques; for example, 2 NV centres 23 nm apart in NDs have been super-resolved using localisation microscopy [47].

Property	Typical organic dye [48]	Quantum dot [48]	Nanodiamond (NV centre) [21, 49, 50, 51, 52]
Size	<1 nm	3–10 nm	>5 nm
Emission spectrum	IR-UV	IR-UV, selected by size	575–800 nm
Emission line width (FWHM)	35–100 nm	30–90 nm	>100 nm
Extinction coefficient	10^4–10^5 $M^{-1}cm^{-1}$	10^5–10^6 $M^{-1}cm^{-1}$	10^4 $M^{-1}cm^{-1}$
Quantum yield	0.5–1.0	0.1–0.8	0.7–0.8
Lifetime	1–10 ns	10–100 ns	25 ns
Photostability	Low	High	Extremely high
Toxicity	From low to high	From low to high	Low

Table 2.1: Comparison of the photophysical properties of organic dyes, quantum dots, and single nitrogen-vacancy (NV) centres [53]

2.2 The nitrogen vacancy in diamond

Driven by the need to discover new photon sources and more information about the formation of natural diamond, physicists have discovered more than 500 optically active crystal defects in diamond [54]. The nitrogen-vacancy (NV) colour centre is naturally present in diamond and is known to give a pink colour to diamond gems. Since its early description in the 1970s, the NV centre has been the most studied fluorescent defect in diamond owing to its varied applications in quantum technologies spanning from quantum optics to quantum sensing [49, 55]. The popularity of the NV centre among quantum physicists is due to its outstanding photostability (*i.e.* hours of observations) and its spin-dependent fluorescence that can be easily manipulated at room temperature. Furthermore, the chemical composition of this crystal defect makes it relatively

facile to incorporate in diamond.

The NV centre consists of a carbon vacancy next to a nitrogen substitution (*i.e.* a carbon atom substituted with a nitrogen atom, see figure 2.1a). The defect has a C_{3v} symmetry and is oriented along a specific crystal plane inside diamond (the [111] plane). The neutral NV centre (NV^0) has 3 electrons originating from the dangling bonds of the 3 nearby carbon atoms and 2 electrons from the nitrogen dangling bond. Although recent progress has been made, little is known about the fine electronic structure of NV^0but we know that it has a doublet ground and excited state ^{2}E and $^2A_2$ with a quartet metastable state $^4A_2$ (see figure 2.2) [56, 49]. NV^0 is most likely to capture a sixth electron from a nearby donor in the lattice (*e.g.* nitrogen substitutions), thus making the defect negative (NV^-) [53]. The six electrons occupy the orbitals a'$_1$, a_1, e_x e_y with two unpaired electrons on e_x e_y . As result, the total spin angular momentum is 1 with a spin multiplicity of 3, thus forming a triplet state [49].

When excited at 532 nm, the NV centre is known to be photoluminescent both in the negative and the neutral charge states, which can be distinguished by a zero-phonon line (ZPL) at 637 nm for NV^- and 575 nm for NV^0 (see figure 2.1b) [49]. In bulk diamond, the fluorescence lifetime of the NV centre is 12 ns in its negative form, and 21 ns in its neutral form but such values can significantly differ in NDs because of the heterogeneity of the defect's nanoenvironment (10-30 ns) [45, 57].

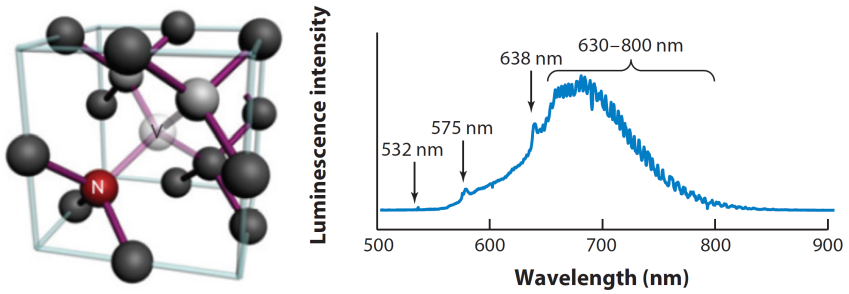

(a) (b)

Figure 2.1: (a) Atomic structure of the NV centre [24]. (b) Typical photoluminescence spectrum of NV centres (room temperature), showing excitation laser (532 nm), the NV^0 ZPL (575 nm), the NV^- ZPL (638 nm) and its vibrational side bands (630–800 nm) [53].

The 637 nm ZPL corresponds to the transition from the ^{3}E to the $^3A_2$ triplet state but intersystem crossing can occur (from ^{3}E to the $^1A_1$ singlet state) thus leading to another radiative transition (1042 nm) from the $^1A_1$ to the ^{1}E singlet states (see figure 2.2). The latter transition is more difficult to observe because its rate is quite low when the ground state is at the spin projection $m_s = 0$. Nevertheless, as shown in figure 2.2, intersystem crossing to the $^1A_1$ is likely to occur if the spin projection is $m_s = \pm 1$, which is a key property of the NV centre's electronic structure. From an experimental point of view, when the electrons are excited to the $m_s = \pm 1$ sub-level with a 2.87 GHz microwave excitation (*i.e.* zero-field splitting), a 10-30 % drop in the fluorescence can be observed depending on the optical set-up used [58], this technique is called optically detected magnetic resonance (ODMR). The possibility to optically probe the NV-centre's spin properties at room temperature combined with its photostability make it an ideal system for quantum sensing (see section 2.5 and chapter 6 for more details). Regarding bioimaging, the broad emission of the NV centre up to the near infrared is very desirable for *in vivo* experiments as the background auto-fluorescence originating from biomolecules is mostly found in green-yellow spectral window (530-600 nm) when

excited at 532 nm.

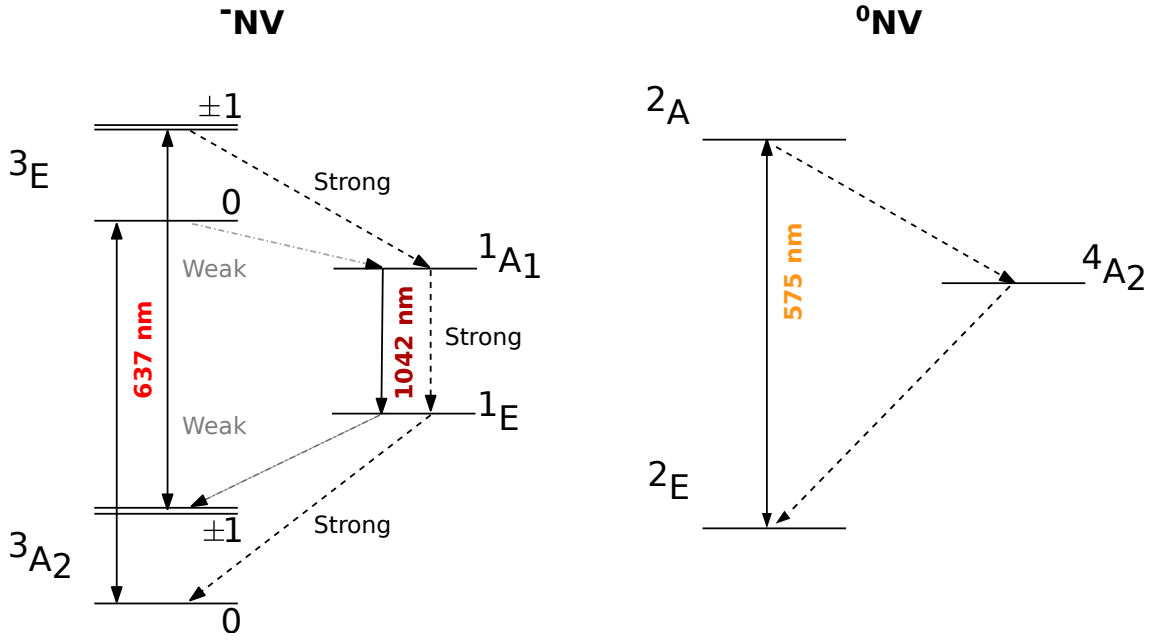

Figure 2.2: Schematic of NV^- and NV^0 electronic structure with the fine structure of the NV^- $^3A_2$ and ^3E levels at room temperature. Figure modified from the publication of Doherty *et al.* in 2013 [49]. The 637 nm ZPL corresponds to the transition from the ^3E to the $^3A_2$ triplet state. Intersystem crossing can occur (from ^3E to the $^1A_1$singlet state) thus leading to another radiative transition (1042 nm) from the $^1A_1$ to the ^1E singlet states. The excited triplet state ^3E is not likely to undergo intersystem crossing to the $^1A_1$ if the spin projection is m_s= 0. However, if m_s=±1 is populated, the intersystem crossing to a singlet state is more likely to occur from ^3E to the $^1A_1$ and the NV centre will relax via the optical transition ($^1A_1$ to the ^1E, 1042 nm). Following relaxation, the colour centre will convert back into a triplet state (*i.e.* transition from ^1E to $^3A_2$, with m_s= 0). The consequence of this conversion at the ground state is that it is possible to spin-polarise the NV centre to m_s= 0 just by optical excitation.

2.3 Synthesis of fluorescent nanodiamonds

The manufacture of FNDs stems from more than 50 years of research in diamond synthesis, which was originally driven by the jewellery and manufacturing industry (*e.g.*, diamond for cutting tools and anti-wear agents). Material scientists and companies started to focus more on NV centre in diamond when two important reports were

published: the observation of single NV centres inside bulk diamond in 1997 and the synthesis of FNDs enriched in NV centres in 2005 [59, 60]. The research on the synthesis of FNDs then intensified such that three different methods are now available for ND production: high-pressure high-temperature (HPHT) synthesis, synthesis by detonation and chemical vapor deposition (CVD).

HPHT synthesis is today the most common method to produce FNDs; in this process, graphite is dissolved using high temperature (>1300 °C), but the extreme pressure applied (> 5 GPa) forces the carbon atoms to crystallise into diamond [61]. Small crystals (up to a few millimetres large) can be produced in a day depending on the purity one wants to achieve. In order to increase the NV content, it is possible to increase the concentration of nitrogen (up to 200 ppm) by adding nitrogen-containing species in the reaction chamber [62]. The microcrystals are then are milled down to nanoparticles (10 nm being the smallest size) using ceramic or metallic beads [63]. HPHT manufacture is the most popular method at the moment because it is more cost effective than CVD and provides a good control of the synthesis conditions (*e.g.,* temperature, nitrogen content etc.). Nevertheless, the yield and the ND's nitrogen content become very low when producing sub-10 nm particles; that is why, synthesis by detonation is preferred for 3-5 nm NDs [61, 64].

The principle behind detonation nanodiamonds (DND) is to detonate explosives in a closed chamber to create, within the duration of the explosion, the great pressure (>20 GPa) and high temperature (> 3000 °C) required for carbon crystallisation. The detonation product is a soot, which contains up to 75%wt. of NDs (3-5 nm in diameter), graphite and other impurities. Acid treatment, centrifugation and ultrasounds are subsequently used to break drown the aggregates and remove contaminants [65]. Despite an early report of a 5-nm detonation ND containing a stable NV centre [66] there is still a debate whether such small nanocrystals can contain a photostable NV centre.

The proximity of the NV centre to the surface, in 5-nm NDs, makes the colour centre very unstable and therefore the probability to find a 5-nm ND with a photostable NV centre is very low [67]. Furthermore, it is difficult to control the crystallisation occurring during the explosion; as a result, the nanocrystals contain impurities and strain that can affect the photostability of the NV centre (*e.g.,* photobleaching or blinking) [66]. The manufacturing process that offers the highest purity of diamond as it allows scientists to finely control the synthesis conditions is CVD.

In general, CVD diamond is grown in a low vacuum chamber (200-0.3m Bar) on a silica substrate (seeded with NDs) in a 2-dimensional fashion [68]. The mechanism of synthesis consists of breaking down gaseous carbon molecules in the chamber using high temperature (>700 °C) and chemically engineer the atmosphere such that diamond is the most stable form of carbon to form on the silicon substrate. As it is possible to control finely the purity of the gas, the temperature and the pressure, CVD produces high quality diamond but the synthesis process is very slow (up to 1 μm/hour). FNDs produced by the milling of CVD diamond are therefore more expensive and not very common in the field of bioimaging; however, they have a great potential for quantum sensing experiments as the purity of CVD FNDs is ideal for high sensitivity measurements.

In all manufacturing processes, the nanoparticles are typically oxygen terminated (*e.g.,* carboxylic acids, ketones, hydroxyl) as the cleaning step involves strong oxidants like sulfuric acid. The other common steps that all the manufacturing processes may include is particle radiation (*e.g.,* electron irradiation) followed by annealing (>700 °C) to generate more NV centres than the ones produced during the synthesis. Irradiation is used to dislodge carbon atoms and create vacancies; the latter will become mobile at elevated temperature (>700 °C) and recombine with nitrogen atoms to form new NV centres.

2.4 Nanodiamonds in single-molecule imaging

In 2005, Yu *et al.* were the first to report bioimaging of FNDs and to stress the great potential of such nanomaterial in biology [60]. Since then, FNDs have been not only implemented in many types of fluorescence microscopy (*e.g.,* wide-field [21], confocal [60] and super-resolution microscopy [46, 69]) but also used in very different biological systems (*e.g.,* bacteria [70], yeast [71], mammalian cells [72] and mice [73]) as NDs have been proven to have very low cytoxicity (excluding DNDs) [23].

In all the mammalian cells that were selected as models (neurons, epithelial cells, immune cells and varied cancer cell lines), most studies revealed no or low cytoxicity when cells were treated with different concentration of NDs (from 0.1 to 1000 μg/mL) [23]. Nonetheless, in some human cells and bacteria, negative effects have been reported on viability when cells were exposed to DNDs at low concentration (5-150 μg/mL) [74, 75]. Fortunately, the decrease in viability can be managed by adding proteins to the DND solution or by changing their surface chemistry [74, 76].

FNDs have a large size (10-50 nm diameter) compared to proteins (mostly 2-30 nm diameter [77]); however, FNDs can be used for *in vitro* single-molecule studies, with rigorous controls on the functional impact of a large probe, as their photostability is unrivalled compared to smaller probes (*e.g.,* organic fluorophores). So far there has not been any reports of *in vitro* single-molecule assays addressing a biological question but there have been significant efforts towards such direction. The first single-molecule experiment using FNDs was published by Bumb *et al.*, who reported an innovative functionalisation of FNDs using silica coating [40]. With their approach they were able to attach a silica-coated FNDs to a single DNA molecule (1.4 μm) and observed the motion of the FND (∼30 nm) as it diffuses in a constrained volume since the nanocrystal is attached to the surface by the DNA strand. In another publication reported by Teeling-Smith *et al.*, the authors functionalised a FND (∼100 nm) to a

double-stranded DNA molecule (λ DNA, 16.5 μm) [78]. They were able to confirm the functionalisation by observing the long fluorescent DNA with FND's fluorescence at one end of the DNA strand. They performed further characterisation for potential quantum sensing experiment but their work had no direct biological relevance.

In vivo single-particle tracking is one of the most exciting applications of FNDs in bioimaging as tracking duration can last for hours without any blinking. In the first extensive characterisation of FNDs for bioimaging, Fu *et al.* were able to track single FNDs inside living cells, a significant proof of concept that led to more single-particle experiments [21]. Then, non-functionalised FNDs were not only tracked inside cells to observe nanotunnels but also tracked in living multicellular organisms such as worms (*Caenorhabditis elegans*) and mice [79, 42]. The ability to follow the trajectory of individual FNDs inside living cells and multicellular organisms can find varied applications but one of the main goals of these experimentations is to pave the way towards tracking biomolecules attached to FNDs, an important experiment if we want to deepen our knowledge of biomolecular interactions.

With a view to investigating the localisation of biomolecules inside cells, FNDs were non-covalently and covalently attached to multiple biomolecules such as proteins (*e.g.*, lysozyme) [80] and imaged inside cells for more than 2 hours [72] but so far there has been only one report where single molecules were covalently attached to a 40-nm FND for *in vivo* single-molecule tracking [39]. Liu *et al.* functionalised the FNDs with a protein involved in cancer (TGF-β: transforming growth factor-beta) by attaching to the FND a polymer (polyethylene glycol) having a streptavidin protein at the end. The streptavidin can then bind specifically to the biotin molecule that was previously added to the molecule of interest (TGF-β). By controlling the stoichiometry, they managed to have on average one TGF-β molecule per FNDs, which was confirmed by particle-size measurements and protein concentration analysis. Single-molecule tracking was

carried out *in vivo* and the specific interaction of the FND-TGF-β conjugates with their respective membrane receptors was also shown. New information about the mechanism by which TGF-β triggers cellular changes was provided thanks to their *in vivo* tracking data.

2.5 Nanodiamonds for nanosensing in biology

Although the first publications on the NV centre as a system for nanosensing employed FNDs in 2008, there have been only a few publications reporting NV sensing using single FNDs in a biological context [25, 26]. Kaufmann *et al.* showed that it was possible to detect down to a few gadolinium atoms with a single FNDs when embedded in a lipid bilayer [81]. Because of the unique electronic structure of the NV centre, the authors were able to spin polarise the NV centre in the $m_s = 0$ state with just optical excitation (see figure 2.2). Following optical excitation, it is possible to measure the relaxation time (form $m_s = 0$ to a mixed state) by looking at the decrease in fluorescence in the first 500 μs since $m_s = 0$ being 20-30 % brighter than the mixed state. For these reasons, the team managed to detect with great sensitivity the presence of 2-6 gadolinium atoms near a single FND just by looking at the change in relaxation time.

In addition to this *in vitro* research there has been significant progress toward NV nanosensing *in vivo.* McGuinness *et al.* were the first to perform ODMR from a FND inside living cells (see section 2.2 for more details) and characterise the spin properties of the NV centre [82, 83] but it is Kuscko *et al.* who managed to make the first measurement of the FND's nano-environment inside living cells [83]. By performing ODMR on a single FND, Kuscko *et al.* quantified the difference of the energy levels between $m_s = 0$ and $m_s = \pm 1$. Such levels have temperature dependence because of the changes in the diamond lattice strain; therefore, using this temperature dependence,

the team achieved nanothermometry inside a living cell.

Despite the fact that the first bioimaging experiments were conducted in 2005, the impact of FNDs on the production of new biological knowledge has been small. As mentioned above (see section 2.1 on page 15), one of the main reasons for not having a widespread use of FNDs in bio-imaging is because sub-10 nm FNDs will appear 10 times dimer than a common organic fluorophore in typical bioimaging conditions although ways to circumvent this problem can be undertaken (see section 2.1 on page 15). The other challenge that FNDs users face is the aggregation of the particles in biological or buffer solutions, although some solutions have been already suggested [40]. Finally, the know-how on the use of FNDs for imaging is not very common and accessible to the bioimaging community such that the researchers using FNDs are either disappointed because of FND misuse or miss an opportunity to use them as they are not aware of their optical and nanosensing properties. Nevertheless, there is much effort now invested in tackling these problems as the interest for FNDs has been growing in the past decade. Indeed, the enthusiasm is clear as shown by the increasing number of publications on FNDs, the new nanodiamond-related start-ups (*e.g.,* Adamas nano, FND biotech, Bikanta etc.) and the large companies that have started marketing FNDs (*e.g.,* Sigma Aldrich) [84].

Chapter 3

Photophysical characterisation of nanodiamonds

3.1 Introduction

Owing to their promising applications in nanosensing and bioimaging, there is a great incentive to synthesise FNDs with better quality; for bioimaging this means brighter sub 10-nm particles while nanosensing experiment requires FNDs with less impurities (*e.g.,* nitrogen or ^{13}C). Thus, there are numerous efforts to manufacture small, bright, and high-purity FNDs that differ by size, nitrogen content and surface chemistry; these FND samples display different NV centre emission spectra and intensity levels due to interactions with the surface, or due to a different number of NV centres per particle [85]. For these reasons, the photophysical characterisation of FNDs is crucial to ensure successful applications in bioimaging, especially using single-molecule microscopy.

An important question in FND characterisation is the proportion of FNDs containing single NV centres, a property paramount for the optimisation of FND manufacture and for FND applications as single-photon sources [86, 87]. The conventional method

to confirm the presence of the single NV centres is to measure the coherence of its emission and calculate the probability of photons being emitted at the same time. However, such photon-correlation experiments require complex instrumentation and have limited throughput, since each measurement needs to be performed individually on FNDs [67, 24]. An alternative method to identify single NV centre is to measure the photon count corresponding to a single NV centre; this, however, is also complicated by the orientation of the two NV centre's orthogonal dipoles [49]. As a result, there is a need for a high-throughput method reporting on the fraction of single emitters in FNDs.

Characterisation methods are also essential for new FND bio-sensing assays. Petrakova *et al.* showed that the charge state of an NV centre could be used to detect chemical changes on the FND surface [88, 89]. Their approach is to measure changes in the FNDs fluorescence (brightness or emission spectra) to differentiate the two photoactive charge states of the NV centre (NV^- and NV^0; NV^+ is non-photoactive), since NV^0 has its emission 60 nm blue-shifted compared to NV^- (see figure 3.1b) [88]. The team then established that the charge state of NV centres in FNDs is affected by specific chemical changes on the FND surface (*e.g.,* modification of functional groups or adsorption of polymers). Nonetheless, the direct charge manipulation of single NV centres by pH in FNDs was not performed because the FNDs used were too large (49 nm) [89]. Indeed (10-20 nm) FNDs would be optimal for such experiments, since they contain shallower NV centres; unfortunately, working with small FNDs poses technical challenges in terms of manufacture and detection capability (*i.e.* small NDs form aggregates and have low brightness) [63].

In this chapter, we report a sensitive and high-throughput wide-field imaging approach that allows us to measure reliably single NV charge states and compare the proportion of single emitters in different FND samples (5-200 nm in size). Such approach provides hundreds of FND fluorescence time traces in seconds, which allows measure-

ments of the proportion of FNDs containing single NV centres, and the detection of spectral shifts that unravel changes in the NV centre charge state. We use this method to study dynamic charge states transitions in multiple FNDs and to demonstrate that the charge state in 10-nm FNDs can be reversibly manipulated by pH, making FNDs promising probes for pH sensing.

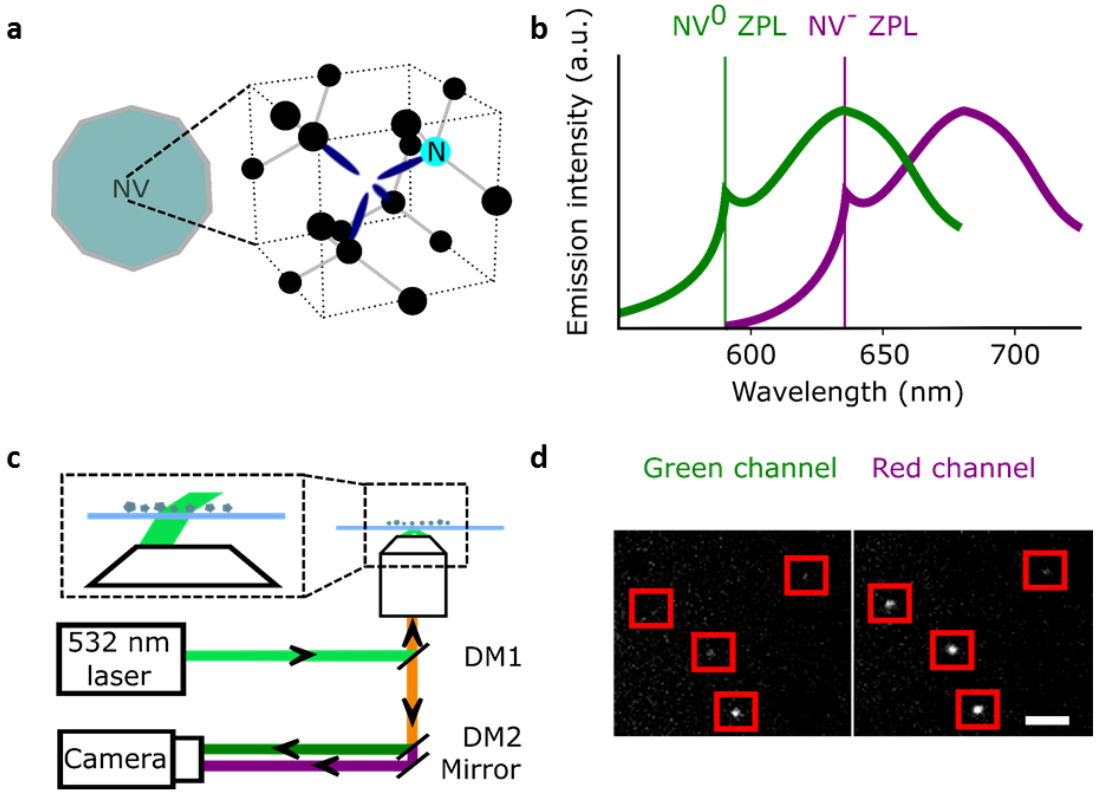

Figure 3.1: Wide-field imaging of FNDs. a, Schematic representation of a ND containing an NV centre including the atomic structure of the defect. b, Emission spectrum of NV^- measured in the 44-nm FNDs and a schematic of the blue shifted emission of the neutral state. c, Simplified representation of the wide-field microscope with NDs immobilised on the microscope slide. The zoomed-in region shows variable-angle illumination; DM1: dichroic with reflective bands at 532 and 638 nm; DM2: 650 nm long pass dichroic. d, Section of the field of view with FNDs. 532 nm excitation at 7.8 kW/cm^2 with variable angle illumination, 100 ms exposure; the red squares represent the FNDs localised by our software (Gapviewer), the photon count for each FND per camera exposure is calculated from a region of interest covering the fluorescent spot; scale bar = 8 μm.

3.2 Photophysical characterisation of different nanodiamond samples

To study the heterogeneity of FND photophysics, we characterised samples of different sizes (5-200 nm), different manufacturing processes and different NV centre content (see section 3.6). The 5 and 10-nm diameter NDs are usually too small to contain more than 2 NVs per ND and have only up to 1% of NDs with NV centre [90]. Since they are undoped, the 50-nm diameter NDs are expected to have up to 10 % of FNDs containing only 1-2 NV centres per particle [91]. The doped 40 and 44-nm diameter NDs contain up to 4 NV/FND with a larger fraction of bright NDs (up to 70 % for the 40-nm, see section 3.6). Finally, the 200-nm doped NDs are all expected to be emitting fluorescence and can have up to 100 NV/FND because of their larger size.

We studied the ND samples using a wide-field two-channel single-molecule fluorescence microscope (see section 3.6). Our large field of view (50 x 80 μm) allowed us to use a low ND density (down to one FND for 40 μm^2, figure 3.1d), ensuring that we are observing single FNDs. We collected 96 to 589 time traces per sample and used all data points to build the photon count distribution of the sum of red and green channels. To detect changes in the emission spectrum, we compared the relative intensities of the red and green channels using the R/G ratio ($R/G\,ratio = \frac{Spot\,intensity_{red}}{Spot\,intensity_{red}+Spot\,intensity_{green}}$). Since the emission of NV^0 is blue shifted (60 nm) compared to NV^-, this ratio offers us a facile way to study the charge of the NV centre. Thanks to the specifications provided by the manufacturer and our confocal and ensemble fluorescence measurements done on the samples, most of the stable fluorescence detected can be attributed to the NV defect (for more information see our publication [92]). Other optically active defects such as the silicon vacancy, the N-V-N and the nitrogen substitution can be neglected based on either their spectral properties or relative scarcity compared to the NV centre.

Our studies of the 50-nm undoped NDs revealed that most time traces showed a total photon count of 1000/100 ms and a R/G ratio of 0.9 (figure 3.2a, left; figure 3.2b). Other traces are brighter (1500 photons/100 ms) with a lower R/G ratio (0.6), as more light is detected in the green channel (figure 3.2a, right). These two populations with distinct R/G ratio can also be seen as a very broad R/G ratio distribution on a 2D histogram (figure 3.2b). We attributed these two R/G ratio states to the different charge states of the NV centre (0.6 for NV^0 and 0.9 for NV^-) based on their respective emission spectra and our detection efficiency for the red and green channels. The photon counts we obtained are 20-fold higher than previously reported for a single NV centre using wide-field imaging and 2-10 times inferior to typical values detected using a confocal setup that usually uses higher irradiance [93, 21, 11].

The 2D histogram for 44-nm NDs shows the same main population as the 50-nm undoped NDs (figure 3.2c); this similarity allows us to assign this intensity to a single NV^- emission, since this sample was manufactured to contain 1NV/FND; we further verified the presence of single NV^- per FND in the 44nm NDs using photon correlation experiments (data not shown). Notably, no clear NV^0 signal at a R/G ratio of 0.6 is observed in these 44-nm NDs, which confirms that the population with a 0.6 R/G ratio in figure 2b is NV^0. The proportion of NV^- in doped FNDs is expected to be high (*e.g.,* >65 % in 40-nm NDs according to the supplier) as ND doping involves high concentration of nitrogen (up to 200 ppm) to improve the probability of NV centre formation; high nitrogen content is known to stabilize NV's negative charge state as nitrogen acts as an electron donor for NV centres [49]. Similar distributions of photon count and R/G ratio were measured in 40-nm doped NDs (figure 3.3a-b, row 5), an expected result based on the comparable size and manufacturing process for the 40 and 44-nm doped NDs.

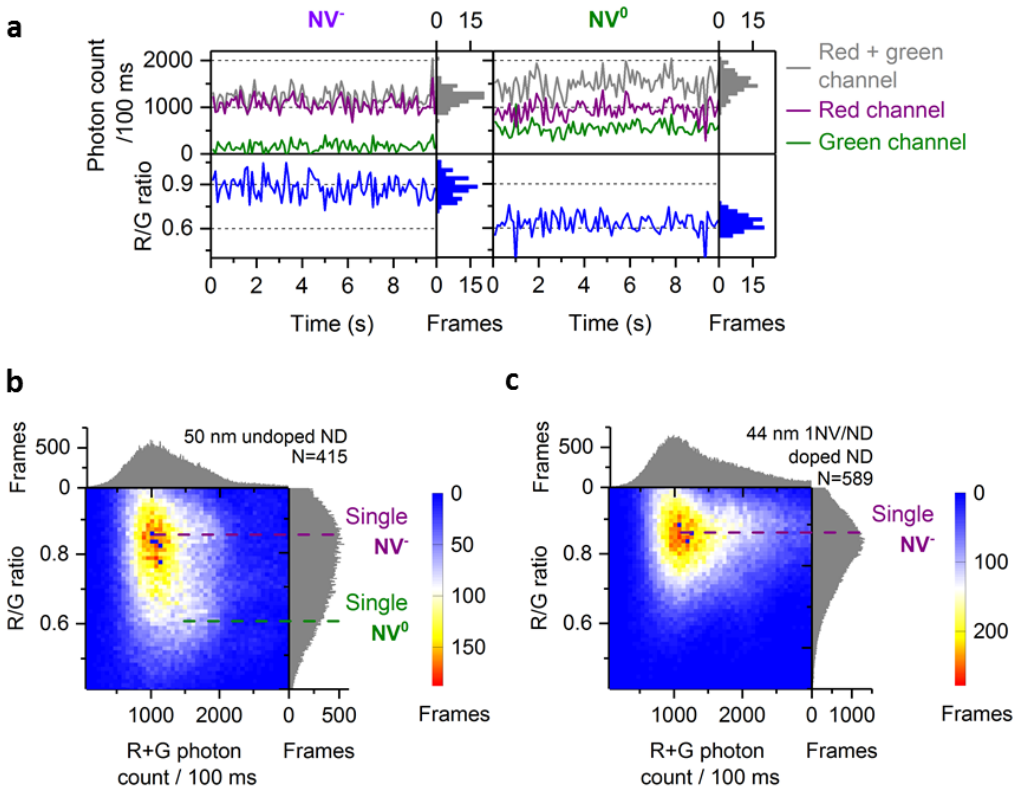

Figure 3.2: Charge states of NV centre in doped and undoped FNDs. a, Typical times traces from 50-nm undoped FNDs corresponding to single NV^- and NV^0. b, 2D histogram of photon count and R/G ratio in 50-nm undoped FNDs; purple and green dotted lines indicate respectively single NV^- or NV^0 fluorescence. c, 2D histogram of photon count and R/G ratio in 44-nm 1NV/ND doped NDs; the purple line indicates the fluorescence from single NV^-. For figure b and c, N is the number of FNDs observed. For all the figures, "Frames" is the frequency of the measurement from a FND (see figure 3.1 for details). The immobilised FNDs were imaged in air using 532 nm excitation 7.8 kW/cm^2 and 100 ms exposure for 25 s.

We then examined sub-20-nm FNDs, which are challenging samples as they contain more unstable NV charge states [90, 94]. In such small particles, the fluorescent defect is closer to charge traps at the surface that can act as electron acceptors to NV^- [66]. We observed that the photon count of the 10-nm doped FNDs mainly originates from single NV centres, which is expected given their small size (figure 3.3a row 3); the distribution of the R/G ratio is centred around 0.7 (figure 3.3b row 3), suggesting that the charge conversion may happen within 100 ms. We attribute this charge state instability to the NV centre's proximity to the surface.

The 5-nm NDs show low brightness, a small bright fraction (<1 %; see section 3.6) and, unlike all the other samples, most of the 5-nm FNDs photobleach within a few seconds. Nonetheless, we can confirm the rare presence of stable and bright FNDs (>2000 photons/100 ms; figure 3.3a row 2), as previously reported [90, 94]. Given the scarcity of such emitters (<0.1% of the total 5-nm NDs) one cannot exclude the possibility that we detected fluorescence from a small subpopulation of NDs having a larger size than 5 nm (*e.g.*, 10-30 nm, as reported by Vlasov *et al.*) [94].

The 200-nm doped NDs exhibit a very broad photon count distribution (figure 3.3, bottom; showing only FNDs with photon count <5000 photons/100 ms (20% of the 200-nm FNDs)). The first maximum of the photon count distribution is above 2000 photons/100 ms, indicating that the sample contains no single NVs per FND, consistent with the probability of having FNDs containing one NV centre being very low in such large doped FNDs. Finally, no NV^0 fluorescence is present in the R/G distribution (figure 3b bottom), very likely due to their size and high nitrogen concentration.

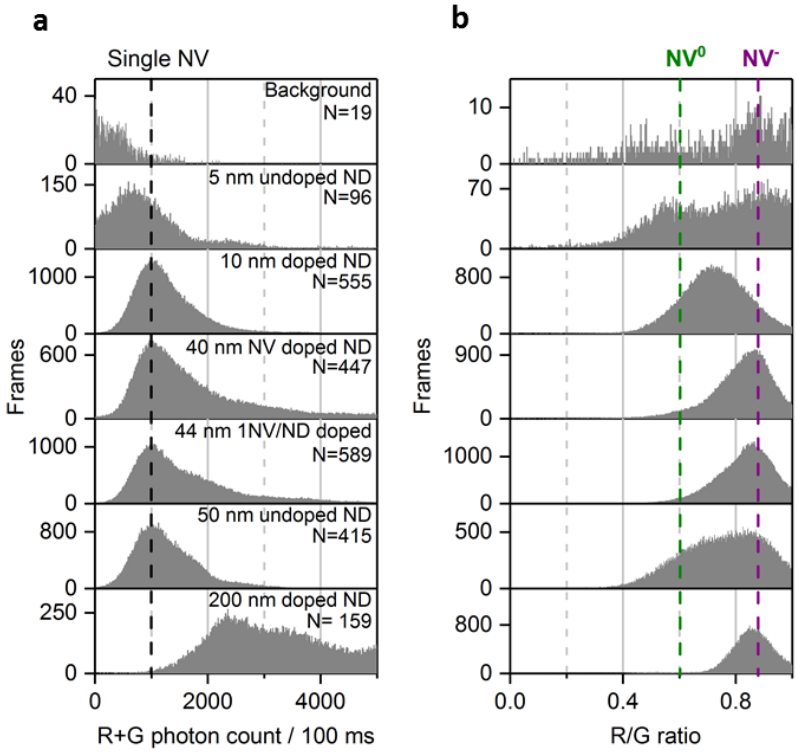

Figure 3.3: Distribution of photon count (a) and R/G ratio (b) in different NDs samples. Black dotted line marks the photon count collected from single NV centre. The background signal is the fluorescence originating from impurities in the microscope slide. The purple and green dotted lines indicate respectively NV^- and NV^0 fluorescence. Using multiple-Gaussian fitting, the proportion of single NV centre (NV^- or NV^0) per FND is estimated be $>$ 70 % for the 50-nm undoped and 10-nm doped FNDs, $<$ 50 % for the 44 and 40 nm-doped FNDs and 0 % for the 200-nm doped FNDs. The same analysis for the 5-nm undoped NDs is not possible because of their low brightness and small sample size. N is the number of FNDs observed and "Frames" is the frequency of the measurement from a FND (see figure 3.1 for details). The immobilised FNDs were imaged in air with 532 nm excitation 7.8 kW/cm^2 100 ms exposure for 25 s.

3.3 Dynamic behaviour of the NV centre in nanodiamonds

To capture dynamic transitions in FNDs occurring in the timescale of seconds, we studied 40-nm FNDs exhibiting NV charge-state transitions. For the population with single NVs, we measured steady fluorescence in 60% of them (figure 3.4a) as opposed to the remaining 40%, in which clear dynamic behaviour was observed. Dynamic traces are mostly due to NV centres with unstable charge states (figure 3.4b (i) and (ii)), which causes in rare cases some on/off blinking (<1 % of the total traces, figure 3.4b (iii)). According to previous studies, fluctuations in ND fluorescence is due to the proximity (<10 nm) between the NV centre and the FND's surface [67, 95]; electron transfer from the NV centre to surface charge traps allows the NV defect to switch from NV^- to NV^0 and then to the non-photoactive NV^+ charge state, causing blinking.

To study the dynamic traces, we first defined the charge states in terms of photon count and R/G ratio using stable time traces (data not shown). We assigned emitters having a photon count of 4000/s and a R/G ratio of 0.6 to single NV^0 (16% of static traces, figure 3.4a top). We also assigned the traces showing a photon count between 2000 and 4000 photons/s and a R/G ratio of 0.7 to 0.8 to time-averaged values of the NV^- and NV^0 states (38% of static traces, figure 3.4a middle); such averaging is consistent with charge conversion in bulk diamonds that may occur within the µs timescale [96]. Finally, we assigned the FNDs emitting 2500 photons/s with a R/G ratio of 0.9 to single NV^- (48 % of static traces; figure 3.4a bottom).

We then collected dynamic and long traces (lasting 30-60 min), which provided enough statistics to compare state transitions within FNDs (N = 32, providing >600 dwells). The dynamic traces showed either two-state or three-state transitions (figure 3.4b (i) and (ii)) with the transition frequency varying among FNDs. To investigate if

these dynamic FNDs share similar states and dwell times, we performed Hidden Markov modelling (HMM) analysis, which showed that a three-state model was sufficient to fit our dynamic traces based on the lower bound values analysis (see section 3.6 on page 49) [97, 92]; the three states identified (NV^- at 0.85, NV^0at 0.67 and a time-averaged state at 0.75, figure 4c) correspond well to those seen in static traces. The slight difference (+/-0.07) between the values from the static and dynamic traces is likely due to small errors in the state allocation by HMM (see section 3.6 on page 49).

We used the dwell times from the HMM analysis to calculate the lifetimes of each NV charge state. Dwell time distributions from the NV^- and NV^-/NV^0states were fitted with a single-exponential decay function (figure 3.4b middle and bottom histograms) while the dwell time distribution from the NV^0 state had to be fitted with a double exponential decay function (figure 3.4b top histogram) as the single exponential decay was clearly missing a long-dwell component. Most of the NV^0 dwells are less than 10 s as shown by the amplitude (A) of the lifetimes (τ): τ_1=3 s $A_{\tau 1}$= 90 %; τ_2=53 s $A_{\tau 2}$=10%. The most representative NV_0 lifetime is shorter than the two other states (τ= 57 s for NV^-/NV^0 and τ=38 s for NV^-, see figure 3.4d), which is expected when using 532 nm excitation, a wavelength known to pump NV^0 back to NV^-, thus making NV^0 lifetime shorter in our imaging conditions [98, 57]. Indeed, based on previous report, we can hypothesise that the transitions between the charge states in NDs occur in a similar fashion as in bulk diamond: the negative charge state can lose an electron to a charge trap (*e.g.,* surface defects) via a two-photon absorption process that will excite the electron into the conduction band. Likewise, the neutral NV centre is most likely to gain back an electron when one of its electrons is excited into the bandgap from the valence band by a two-photon absorption process.

The transition probabilities provided by the HMM are more difficult to interpret because sub-second transitions are likely to occur and might not be detected with

our current time resolution. Nevertheless, the transition matrix shows that NV^0 (0.01 versus 0.0007) is more likely to move to a mixed state (NV^-/NV^0) like NV^- (0.01 versus 0.006), while the mix state is more likely to go to NV^0 (0.24 versus 0.006). This data in addition to the lifetime measurement support the charge-transition model elaborated in bulk diamond in which NV^- can be photoionised and NV^0 pumped back into NV^- with 532 nm excitation [57, 99].

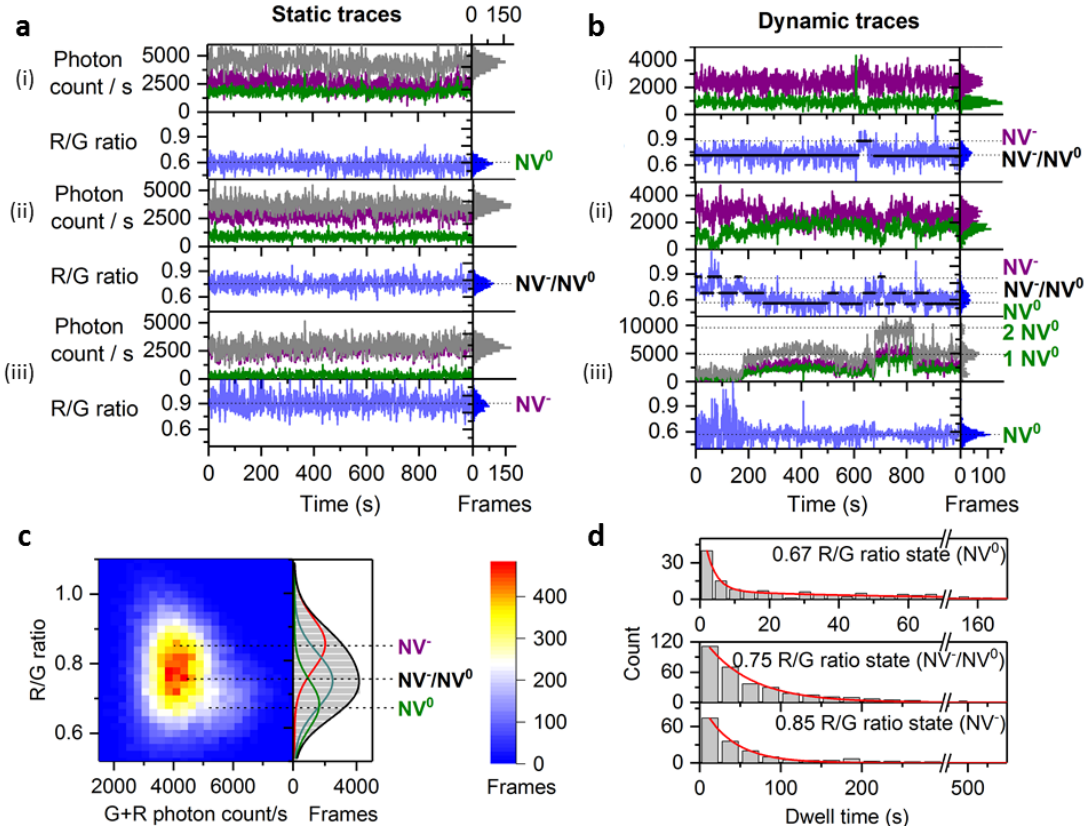

Figure 3.4: States and dynamics of NV centre in FNDs. a, Typical static time traces corresponding to the two different charge states of single NV centres ((i): NV^0 R/G ratio = 0.6 – 4000 R+G photons/s; (iii): NV^-: R/G ratio = 0.9-2000 R+G photons/s) and a time-average of the two charge states ((ii): NV^-/NV^0: R/G ratio = 0.7-0.8 - 2000-4000 R+G photons/s). Red and green photon counts are shown in purple and green, respectively; the sum of red and green photon counts is in grey. b, Typical dynamic traces; the first trace (i) shows two-state transitions as demonstrated by the spectral inversion; the second trace (ii) is more dynamic and shows three-state transitions; the last trace (iii) shows two-level blinking c, 2D histogram of 32 dynamic traces with their R/G ratio distribution on the right side of the figure; the R/G distribution is fitted with 3 Gaussian profiles centred at the R/G ratio values calculated by HMM modelling, which fits well the distribution and the 2D histogram especially the brighter NV^0 population. Gaussian centres: NV^0 R/G ratio = 0.67; time-averaged NV^-/NV^0: R/G ratio = 0.75; NV^-: R/G ratio = 0.85. d, Dwell time analysis of the 3 states by HMM. The distribution of dwell times is fitted with a double exponential decay function for the NV^0 state (top histogram, fitting function shown in red). The lifetimes are τ_1=3 s +/- 0.3 s $A_{\tau 1}$= 90 %; τ_2=53 s +/- 7.7 s $A_{\tau 2}$=10% for NV^0. The distribution of dwell times is fitted with a single exponential decay function for the NV^-/NV^0 and NV^- states (middle and bottom histograms). The lifetimes are: τ= 56 s +/- 1.7 s for NV^-/NV^0; τ= 38 s +/- 1.5 s for NV^-. 32 FNDs were used for the subfigures b, c and d. "Frames" is the frequency of the measurement from a FND (see figure 3.1 for details). The immobilised FNDs were imaged in air using 532 nm excitation 3.4 kW/cm^2 and 1 s exposure for 20 to 60 minutes.

3.4 Effect of the surface chemistry on NV centre fluorescence

Since we could detect different charge states of the NV centre, we investigated our ability to modify the FND's emission by immersing immobilised 10-nm NDs into separate solutions containing DNA, proteins, and a reducing agent (DTT); none of these solutions showed detectable effects on the photon count or the R/G ratio (data not shown). Nevertheless, changes in pH were found to have a clear effect on the NV centre's charge (figure 3.5a and b), where high pH shifts the R/G distribution towards higher values (from 0.7 to 0.8 R/G ratio in figure 3.5a).

The relation between pH and the mode of the R/G ratio distribution is relationship for pH values ranging from 4 to 10. Using this region, we estimated that we can measure the pH of a solution from the mode of the R/G ratio distribution with an accuracy of $\sim$0.4 (average of absolute value of the residuals).

To explore the possibility that these NDs could be used as pH sensors, the reversibility of the effect was tested, by imaging the same field of view (containing 140 FNDs) after consecutive immersions into acidic and basic solutions. The modes of the R/G ratio distribution (figure 3.5c) clearly showed that the effect of pH on the R/G ratio is indeed reversible.

We have also examined whether we have the resolution to detect the increase of the R/G in basic pH on the same FND particle; this was indeed the case (see example in figure 3.5d). In addition to this change in R/G ratio, there was also a decrease of photon count (from 1750 to 1250 photons/100 ms) at pH 12.8. Such increase of R/G ratio and decrease of brightness correlates well with our observation of charge state conversion on the 50-nm undoped and 40-nm doped FNDs (figure 3.2; figure 3.4), with the deviations of the R/G ratio values from 0.6 and 0.9 being attributed to the charge instability in

the 10-nm FNDs. However, our data indicates that the NV centre will stay longer in a charge state (NV^0 for acidic pH or NV^- for basic pH) within 100 ms, leading to changes in the R/G ratio. We do not have such measurement for other pH values so we cannot estimate the accuracy of our pH estimation using the R/G ratio but given the width of the R/G ratio distribution for a single ND, we expect that the accuracy should be enough to detect intracellular pH changes (+/- 1) provided the FND is imaged for long enough (~30 sec).

The mechanism behind this pH-dependent charge transition of NV probably is likely to involve deprotonation of ND surface groups (mainly OH or COOH groups generated during ND acid cleaning, and affecting the ND's surface charge), thus creating more negative charges around the NV centre [100]. Our findings confirm previous reports that FNDs photophysics is affected by surface chemistry and demonstrate that they can be used for pH nanosensing [88, 89].

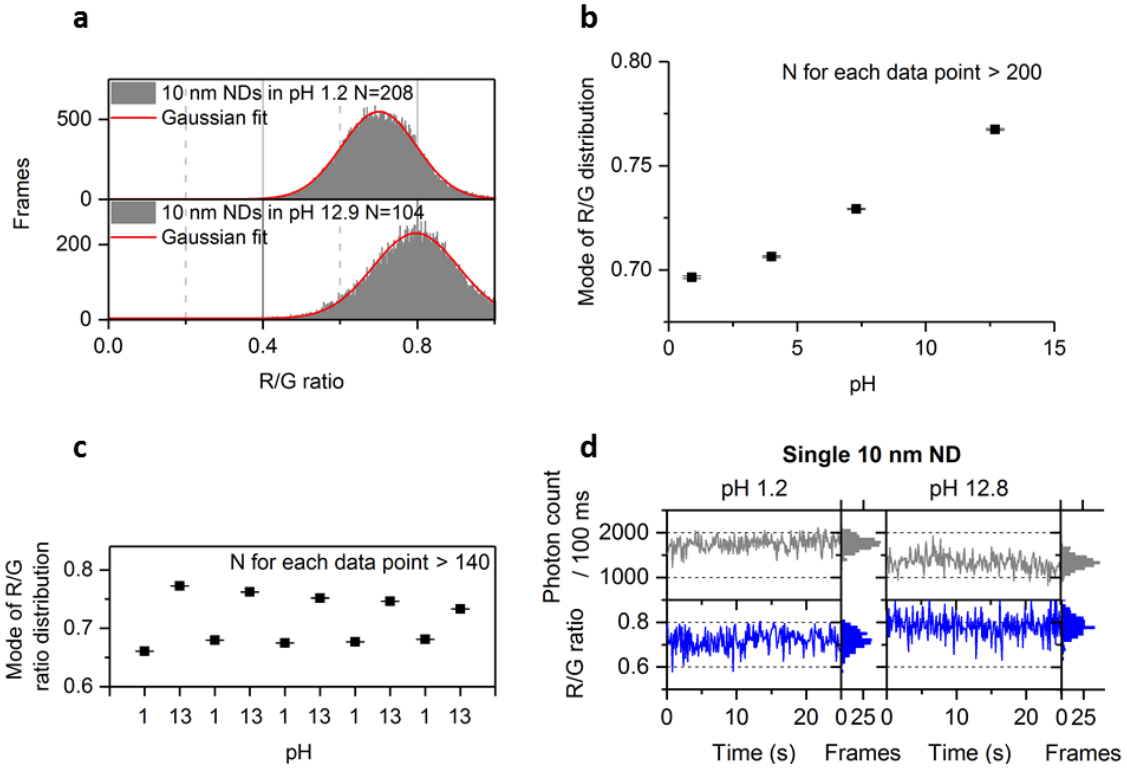

Figure 3.5: Effect of pH on 10-nm FNDs. a, Increase of the R/G ratio distribution in the 10-nm doped FNDs at high pH. Aqueous solutions used: 0.01 M HCl for pH 1.2, and 0.1 M NaOH for pH 12.8. b, Relation of the mode of the R/G ratio distribution with pH following Gaussian fitting of the distribution (0.01 M HCl for pH 1.2, 0.1 M NaOH for pH 12.8 and commercial buffer solutions used for the other pH data points). c, Reversibility of the effect following multiple washing on the same field of view containing more than 140 FNDs (washing was performed using deionized and filtered water; the same acidic/basic solutions as in figure a were used). The convergence of the modes after the first repeat may be due to the washing steps that gradually become less efficient. d, Observation of the charge state conversion on the same FND particle in acidic and basic solutions (same solutions used as in figure a). R+G photon count is shown here. Approximately 75% of the single NV centres observed showed this increase of the R/G ratio in basic solution. The error bars (figure b and c) indicate the standard error from the Gaussian fitting. N is the number of FNDs observed and "Frames" is the frequency of the measurement from a FND (see figure 3.1 for details). The immobilised FNDs were imaged with 532 nm excitation 7.8 kW/cm^2 100 ms exposure for 25 s.

3.5 Discussion

Our work demonstrated that wide-field imaging and automated time-trace analysis is a powerful approach to characterise ensembles of FNDs. By examining large numbers of single FNDs in parallel, we were able to detect single NVs in up to 500 FNDs per sample, providing helpful comparisons of the proportion of single emitters in different samples based on their photon count distribution, a task facilitated by the random orientations of the spin-coated NDs on the microscope slide. We also introduce the use of the R/G ratio to analyse the charge state of the NV centre, a crucial determinant on the FND photophysical behaviour. Our technique can be easily implemented to screen different FNDs samples to investigate the proportion of single NV/ND and the charge stability of the NV centre since measuring >100 FNDs takes only seconds.

We overcome the problem of the sub-optimal orientation of the defect by imaging up to 500 FNDs randomly oriented for each sample, thus ensuring that we have at least enough optimal orientations of FNDs with different charge state or number of NV centre per particle within a sample. Since we used a statistical approach to define the photon count provided by a single NV, it is difficult to confirm that a given FND contains only one NV centre based on a single observation if no charge transitions are observed. For this reason, photon correlation experiments are more suited in this case [87]. However, this limitation could be overcome by investigating the orientation of NV centre using defocused orientation and position imaging [101].

Our results on the charge state instability in 10-nm FNDs or undoped 50-nm FNDs confirm previous reports that established the negative impact of ND size or low nitrogen concentration on the stability of the NV^- [67, 49]. Further, our high-throughput approach allowed studies of small but significant subpopulations of the FNDs, such as the one having dynamic single NV centres; based on 32 dynamic time traces, we could estimate the lifetimes of the NV^- and NV^0 in FNDs. Such a study was not reported

before as confocal or wide-field measurements described lifetimes of NV^- from only a single particle [93, 66].

The lifetimes we measured for NV^- and NV^0 (from 3-60 s) significantly broadens our understanding of dynamic FNDs, as previous studies only report on the on and off lifetimes of FNDs. Indeed, measuring blinking might be easier to perform in FNDs, but since the NV centre has two fluorescent states ($NV^-$and NV^0) and one non-fluorescent state (NV^+), blinking-based studies are ambiguous with regards to the charge transitions involved in the charge-transfer events. The closest report to our results is a study published by Aslam *et al.* who investigated charge state transitions of a single NV centre in bulk diamond, and measured lifetimes for NV^- and NV^0 (57 ms and 465 ms respectively) three orders of magnitude shorter than what we measured; however, those measurements used significantly different conditions such as the fact they study only one NV centre in bulk diamond. Further, they used a different excitation wavelength (593 nm) and as shown in the same paper, the charge transition rates between NV^- and NV^0 are dependant on the excitation irradiance and the wavelength [98].

It is likely that the mixed state NV^-/NV^0 is caused by photoinduced subsecond charge transitions reported by Aslam *et al.*. We do not exclude that the transitions we measured in the second time range are also photoinduced but another phenomenon must occur to increase the lifetime of charges states above 1 s. Owing to the complexity of the system represented by the FNDs we can merely speculate with the following suggestion. Electron donors or acceptors on the ND surface could be stochastically photoactivated and cause the NV centre to change its charge state. It would be possible to test this hypothesis by taking longer recordings of such NDs (3-10h) and compare the lifetimes with the one that we found.

The lifetimes of the mixed state NV^-/NV^0 and NV^- could be fitted with a single-exponential decay function, which is surprising given the heterogeneity of the possi-

ble localisations of the NV centre inside a ND. Different localisations should affect the electron density around the NV centre; for instance, the presence of electronegative/electropositive species on the surface. One can then expect that such differences in the nanoenvironment could lead to different rates and the lifetime distribution would require a multi-exponential fitting. Yet, it is likely that the nanoenvironment of dynamical NV centres in our 40 nm ND sample is not that diverse when considering the following factors. The NV centre is preferentially oriented on the [111] plane and the faces of the NDs are likely to be parallel to the [111] plan as it is the weaker plan [49, 102]. Moreover, modelling and experimental data suggest that there is a 4-8 nm minimum distance from the surface for an NV centre to be still photoactive [67, 103]. We can therefore suggest that the dynamical NV centres are mostly located 4-8 nm away from the surface in a plane that is parallel from the surface [111]. Such restrictions could limit the range of photophysical behaviours that we could observe and explain why single-exponential fitting was suitable for the mixed state NV^-/NV^0 and NV^-. Further modelling work should allow us to confirm this hypothesis.

The presence of a longer component only for NV^0 might be due to sub-seconds transitions into the dark NV^+ state that could slow down the transition from NV^0 to NV^-. The rare cases of blinking in our data set support such hypothesis as we can see transitions occurring from NV^+ to NV^0 (see figure 3.4 on page 41) but with such a limited number of dwells we cannot perform any quantitative analysis. Charge transitions with NV^+ are poorly understood but we can speculate that thermal fluctuations in the lattice could modify the strain in NDs and cause greater charge traps for nearby NV centres. Dislocations and lattice mismatches may have an impact in electronic densities because of the possible recombination of dangling bonds especially under strain or thermally induced lattice expansion [104].

We also showed that FNDs can be directly used for pH nanosensing. In ways similar

to the studies of Petráková *et al.* and Karaveli *et al.*, who showed that the NV charge state in FNDs can be used for sensing (electrical potential or surface chemistry changes), we demonstrated a simple practical implementation of FND sensing without the need for functionalisation or equipment such a spectrograph or microwave generator for spin state manipulation [88, 105, 89]. Notably, pH did not significantly impact the R/G ratio in the 44-nm doped FNDs (data not shown), consistent with the prediction by Petráková *et al.* in 2012, which proposed that only small particles (10-20 nm) could lead to optically detectable transitions of NV's charge because of required proximity to the surface [88]. At the moment, our approach would require calibration before taking a pH measurement but a better understanding of the heterogeneity of FNDs photophysics could permit us to achieve absolute reading without any need of calibration.

In summary, our ability to detect simultaneously hundreds of single NV centres and their charge states is a powerful screening method for material scientists who manufacture FNDs and need a facile and reliable way to characterise their photophysical properties. Such analysis will also interest physicists working on quantum optics applications, who need to screen FND samples for brightness, charge stability, and the fraction of FNDs having a single NV centre. Our capability to study dynamic FNDs directly and in parallel will enhance our fundamental understanding of NV charge transitions in a nanocrystal and our ability to maintain the negative charge state, which is the charge state that is mostly used in FND commercial applications. Considering that FNDs show great photostability compared to organic fluorophores, our findings should foster more applications of single-molecule fluorescence imaging and tracking experiments *in vitro* and in living cells, as well as sensing experiments such as pH monitoring in microfluidics or pH mapping inside biological samples [106]. Finally, our method should also facilitate the development of biosensing assays based on the measurement of the NV charge state conversion and its dynamic behaviour. Such assays will be

helped by further study on the effect of bio-functionalisation on the charge state since the NV centre can be affected by the surface chemistry.

3.6 Materials and methods

Nanodiamond samples

Doped nanodiamonds of 10, 40, 44 and 200-nm in diameter were commercial high-pressure-high temperature (HPHT) samples enriched in nitrogen followed by particle irradiation to generate vacancies (providers: 10 and 40-nm: Adámas nano; 44-nm: FND biotech; 200-nm: Columbus Nanoworks). Following the high temperature annealing of NDs, the vacancies recombine with the nitrogen to form NV centres. When not provided by the manufacturer, the fraction of NDs containing NV was coarsely estimated by dividing the density of FNDs by the density of NDs deposited on the glass surface. The values obtained from 2 to <0.1 % are within the range of values reported in the literature (0.03 to 70%) depending on the size and manufacturing process [63, 90]. The 44-nm NDs were manufactured to contain a maximum proportion of one NV centre per FND. The NV centre's emission spectra were measured in all our samples. The presence of single quantum emitters in the 44-nm sample was confirmed by photon correlation experiments (data not shown). 50-nm NDs were undoped HPHT particles. All the samples were acid cleaned, sonicated and their size distribution was confirmed by single-particle tracking and/or dynamic light scattering.

Microscope and imaging

The particles were spin coated at a very low density (down to 1 FND for 40 μm^2) and imaged using a single-molecule desktop wide-field microscope Nanoimager S (Oxford Nanoimaging) with a 1.4 NA oil immersion objective. The emitted light is split into a

green and red imaging channels with a long pass filter at 650 nm for the red channel (see figure 3.1c). The 1W 532 nm CW laser allows us to detect single NV centres with 10-1000 ms time resolution when used at full intensity (7.8 kW/cm^2). The exposure time of 100 ms was selected for most experiments as it provided the best SNR for a minimal acquisition time (25 s). Illumination for the TIRF objective was at 50° to remove out-of-focus background and no particular light polarisation was applied to the excitation path according to the manufacturer. All the samples were exposed to maximum excitation intensity for 30-60 sec to photobleach other emitting species (*e.g.*, surface defects). The photon count distribution from 80 to 300 particles per sample was collected by imaging different fields of view. A custom-built confocal set-up was used to perform spectral measurement and photon correlation experiments as we previously reported [107]. For pH sensing, the 10-nm NDs were immersed in different buffer solutions using silicon gasket to form wells. A 0.01 M HCl solution was used for pH 1.2, a 0.1 M NaOH solution for pH 12.8, a 1X phosphate-buffered saline solution (PBS) for pH 7 and the pH 4 measurement was carried out using a commercial buffer solution (Hanna instruments). Washing was performed using deionized and filtered water (220 nm pores) and the acquisition was done 1-3 minutes following the solution addition.

Time trace analysis and HMM

The raw image was processed by home-built software (GapViewer) that detects diffraction-limited spots by their intensity. It performs background subtraction for each frame using the intensity around the Gaussian profile of the FNDs emission. The photon count is calculated by adding both channels and the R/G ratio was computed as $R/G\,ratio = \frac{Spot\,intensity_{red}}{Spot\,intensity_{red}+Spot\,intensity_{green}}$. Based on the NV centre emission spectra of the two charge states previously reported [98] and the wavelength dependence of the quantum efficiency from the microscope's sCMOS camera , we expect a R/G

ratio difference of 0.3 between NV^- and NV^0 with NV^0being brighter than NV^-. The stable and dynamic traces were manually selected based on their R/G ratio (within 0.6 and 0.9) and their intensity (0-1500 photons/s for the green channel and 1000-3200 photons/s for the red channel). Some dynamic time traces (<10%) were excluded from the analysis if their R/G ratio transitions were showing more than 3 states because it could indicate the presence of a second but dimmer NV centre. Following HMM processing of the manually selected dynamic and stable time traces (EbFRET, 10 restarts and 0.001 precision) we selected the 3-state model because a 4-state model would only lead to negligeable increase of the lower bound (less than 10) compared to from a 2 to a 3-state model (lower bound increase approx. 30) [97]. Then HMM analysis was run again only with the dynamic traces in order to extract the dwell times (prior strength set with a 0.2 centre). The priors were set using the state's centres found in the first HMM analysis where no priors were set. The durations of the dwell times for each state were extracted and fitted with a single or double exponential decay.

Chapter 4

Tracking of diffusing nanodiamonds

4.1 Introduction

The previous chapter provided a new insight into the photophysical behaviour of FNDs in air and in solutions containing different chemical species (*e.g.,* acid, base, DNA etc). Such findings were produced using NDs immobilised on the glass slide in order to obtain more accurate measurements in comparison to diffusing FNDs. However, one of the main applications of FNDs in bioimaging is to track individual biomolecules inside living cells. Furthermore, one cannot exclude the fact that the FNDs' interaction with the glass surface on which they are immobilised might have an impact on the FND's response to the solution content. For instance, Bradac *et al.* reported that a change of substrate can cause significant changes in the FND's photophysical behaviour. In their study of the blinking of FNDs in air, the authors found that blinking is greatly reduced when the nanoparticles are immobilised on silica compared to borosilicate [67]. The improvement of the FND photostability was due to a difference of the charge transfer between the FNDs and the substrate. As a result, in order to expand our findings on immobilised FNDs, we decided to investigate the photophysics of diffusing FNDs using

single-particle tracking.

Single-particle tracking (SPT) was developed in the 80s to investigate different molecular processes occurring in living cells such as membrane trafficking and molecular motors [108, 109]. In 1981, Ghosh *et al.* managed to track diffusing molecules on the cell membrane and estimated their apparent 2–dimensional diffusion coefficient [109, 110]. The membrane receptors they tracked were labelled with fluorescent probes but in the same period Geerts *et al.* achieved SPT using gold nanoparticles as labels (20-40 nm) [108]. Gold nanoparticles could be easily observed under bright field illumination because of their light scattering properties. The authors introduced nanoparticle tracking in the context of bioimaging but it is only two decades later that the power of SPT had been considered for nanoparticle size characterisation [111].

Nanoparticles are used in many industries such as pharmaceutics and food industries and it is therefore important to control for their size as it may have significant impact on the product's quality. Dynamic light scattering (DLS) is a conventional approach to determine the diameter of nanoparticles; the machine analyses the intensity's fluctuation of the light scattered by an ensemble of nanoparticles to estimate their size. The limitation of this technique is that when measuring an ensemble of particles, the large particles will dominate the signal recorded as the intensity of the scattered light is proportional to the sixth power of the nanoparticle diameter, thus leading to inaccurate measurement. SPT can provide a more accurate and robust measurement of the particle's size as each nanoparticle size is recorded regardless of their size as long as it exceeds the mininal diameter that can be detected. Additionally, DLS measurements can be affected by the fluorescence if the DLS's light source has the right wavelength to excite a fluorescent sample.

More specifically SPT size estimation works by localising particles in the field of view with sub-diffraction accuracy (see section 2.1) from their scattering or in our case

fluorescence emission spot with the view to measuring their individual 2-dimensional displacement. If the track is long enough (*e.g.,* 200 ms for 50 ms exposure), one can calculate the mean square displacement (MSD) which can be used to estimate the diffusion coefficient of the nanoparticle. With this coefficient it is possible to estimate the Stokes radius r of the particle using the Einstein-Stokes equation:

$$D = \frac{k_B T}{6\pi\eta r} \tag{4.1}$$

Where k_B is the Boltzmann constant, T the temperature of the sample and η the dynamic viscosity of the suspension. Because in our case the layer of ions or solvent surrounding the particle is negligible compared to the size of the nanoparticle, the Stokes radius r of the particle can be used to approximate the radius of the particle. Further considerations and more complex models must be taken into account when the particle is not spherical (*e.g.,* DNA strand).

Fluorescence-based SPT on FNDs to estimate their diffusion coefficient has already been reported by Faklaris *et al.* on a 35-nm FNDs but they did not analyse smaller FNDs probably because tracking fast diffusing FNDs is more challenging as their brightness is limited (*i.e.* lower content of NV centre per FND) [44].

In this chapter we report SPT on different NDs sizes down to 5-10 nm; furthermore, unlike previous reports, the dual colour microscope and the tracking algorithm we used allowed us to collect simultaneously photophysical and size information from each track. In addition to unravelling new information on the photophysics of diffusing FNDs, we developed a SPT-based method to investigate the proportion of NDs containing NV centre. Such property is an important aspect of ND characterisation that is difficult to investigate as it usually requires the combination of fluorescence microscopy and atomic force microscopy (AFM).

4.2 Size characterisation of nanodiamonds

Dynamic light scattering and SPT were performed on the same samples (5 and 50-nm ND) to validate SPT as a size characterisation method. In order to overcome the problem of tracking fast diffusing NDs (5-nm) with low SNR we used an 80% glycerol concentration to slow down the particles, optimised imaging conditions and high-performance localisation/tracking software our team has developed.

DLS and SPT analysis gave similar size estimations for the 50 nm particles (+/- 1 nm) despite a higher standard deviation (SD) for SPT (see table 4.1). SPT performed on the 40-nm NV doped NDs showed a hydrodynamic diameter 3-nm inferior to the expected value. Regarding the 5 and 10-nm sample, the diameters measured are greater than the expected size: 25.6 nm for the 10-nm ND sample and 8.1 (DLS) or 12.8 (SPT) for the 5-nm ND. The cause of the discrepancy between the expected size and the measured one (SPT and DLS) may be due to aggregation of the NDs; moreover, concerning the SPT measurement, it is also possible that the size of the NDs is overestimated as SPT might be biased towards larger FND; bigger NDs are more likely to contain multiple NV centres. However, as shown in the section 4.4 and in figure 5.4 in chapter 5 page 74, we know that it is possible to track 10 and 5-nm particles because we could perform SPT on 1 nm fluorescent molecules as their high brightness allows it. Finally, it is worth mentioning that the 5-nm NDs did not show any red fluorescence (*i.e.* localisation from the red channel) that is characteristic of NV centre but were tracked using their green fluorescence, which is probably coming from the surface defect (see section 3.2 on page 33).

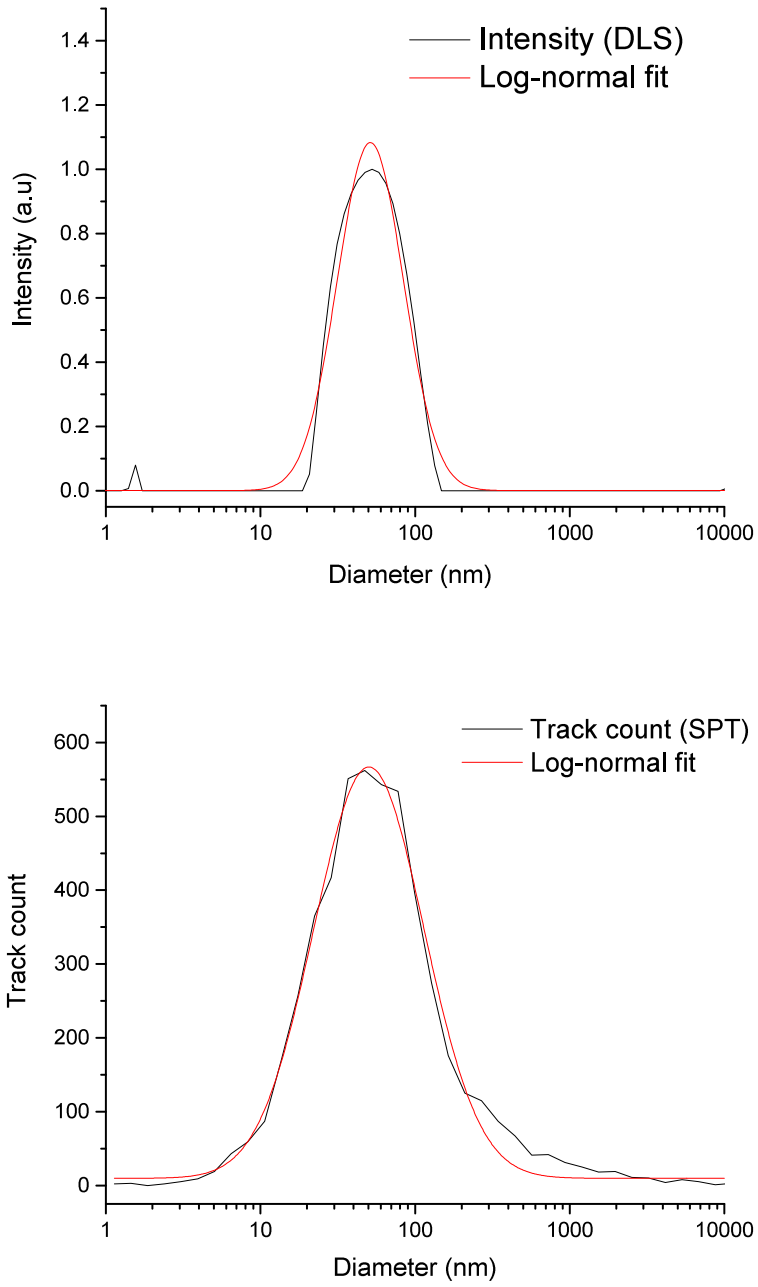

Figure 4.1: Dynamic light scattering (DLS) and single-particle tracking (SPT) measurement on 50-nm NDs. DLS was performed in water and SPT in 80% glycerol.

	DLS		SPT	
	Diameter in nm	SD in nm	Diameter in nm	SD in nm
50-nm ND	51.4	38.5	50.2	135.6
5-nm ND	8.1	4.8	12.8	44.8
10-nm NV-doped ND	N/A		25.6	21.5
40-nm NV-doped ND	N/A		37.0	27.8

Table 4.1: Hydrodynamic diameter measurement (DLS and SPT) on different ND samples. The diameter corresponds to the mode of the log-normal fitted function. The SD is also provided by the fit. N/A: not analysed

4.3 Photophysics of diffusing nanodiamonds

Before analysing the photophysics of diffusing nanodiamonds, the tracking software was tested on fluorescent beads (100 nm in diameter) as a control for the red/green (R/G) ratio measurement. The distribution of the R/G ratio in figure 4.3a is centred around 0.5, which is the expected value (beads are equally bright in both channels). The measurement was then performed on the 40-nm NV doped NDs; the R/G ratio is higher than 0.5 (see figure 4.2 and 4.3b) as found in the chapter 3 but the distribution found is broader suggesting that the charge stability of the NV centre is impaired in solution; furthermore, a bright subpopulation having a ratio of 0.8 can also be distinguished, which might be caused by a different photophysical behaviour from the NV centre. The other samples (50, 10, and 5-nm ND) are not shown here as the low brightness and/or their fast diffusion in solution did not provided a good SNR to do such analysis.

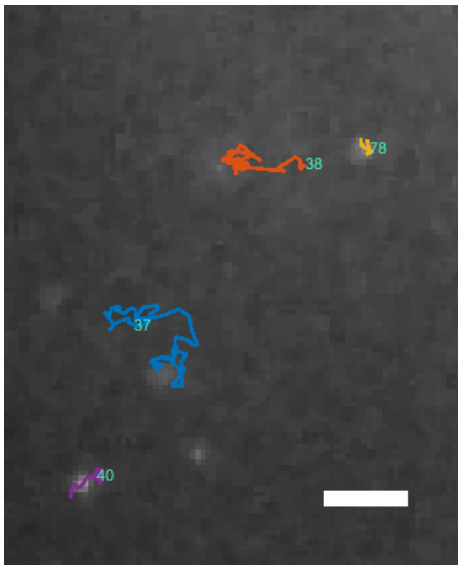

Figure 4.2: Typical tracks of 40-nm NV-doped NDs under 532 nm excitation, 7.8 kW/cm^2, 50 ms exposure time. Scale bar 2 μm.

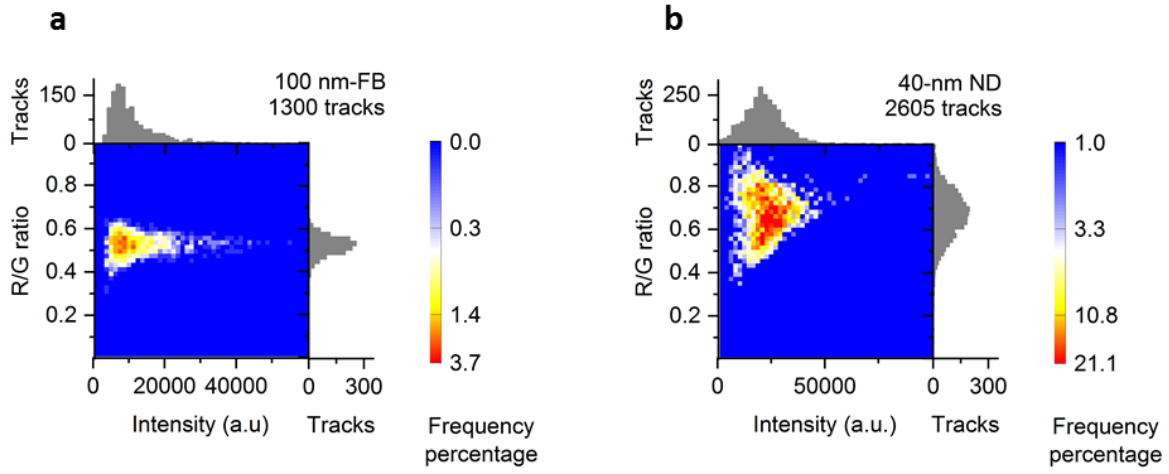

Figure 4.3: Distribution of the R/G ratio versus the track's intensity. 532 nm excitation (a) 140 W/cm^2, 50 ms exposure. (b) 7.8 kW/cm^2, 50 ms exposure.

4.4 Proportion of fluorescent nanodiamonds

The fraction of FNDs in a ND sample is an important part of the sample characterisation as it has major impact on how to use a given ND sample for single photon sources or imaging applications. To investigate such fraction, we labelled the nanoparticles with Cy3b (see section 4.6). On figure 4.5b, most of the coated NDs show a R/G ratio ($\sim$ 0.08) similar to the one measured for free Cy3b ($\sim$ 0.1). The difference in laser power excitation could explain why coated NDs show slightly lower ratio than free Cy3b. Data on figure 4.5c is presented in a simple histogram because the number of tracks was too low to be displayed like in figure 4.5a. Interestingly, a few tracks from coated NDs have a higher ratio than Cy3b ($\sim$ 0.17) even at high intensity where the SNR is increased (see arrow figure 4.5b). It is possible that these particles are the ones containing NV centres. The MSD data also indicated that most of the particles tracked were approximately 50 nm in diameter (data not shown).

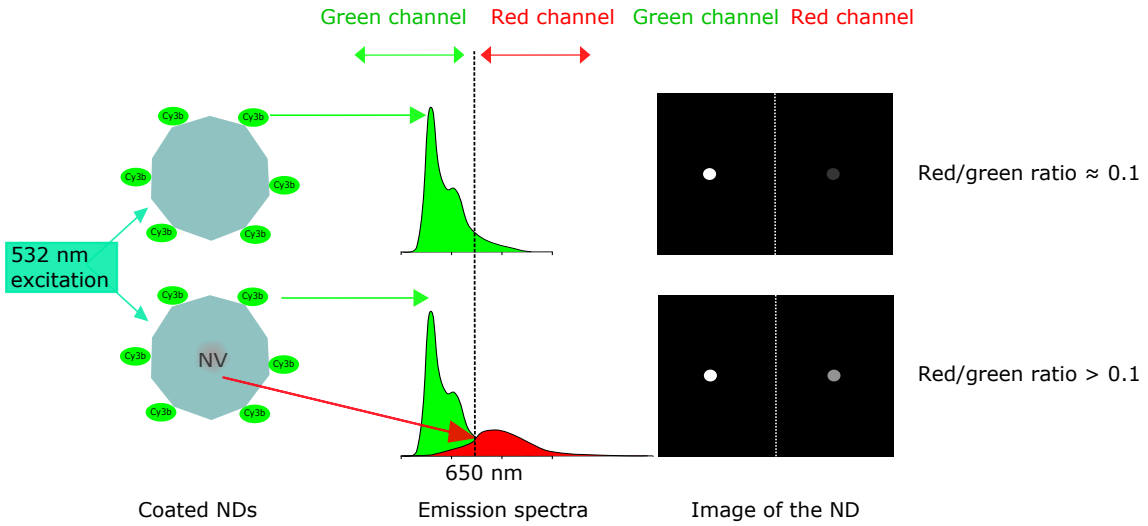

Figure 4.4: Investigating the fraction of fluorescent NDs. NDs are coated with fluorophores (Cy3b) in order to image all the NDs including the non-fluorescent ones. The particles containing NV centres will not only emit light in the green channel but also in the red one. As a result, the R/G ratio will be higher than 0.1, which is the ratio for free Cy3b.

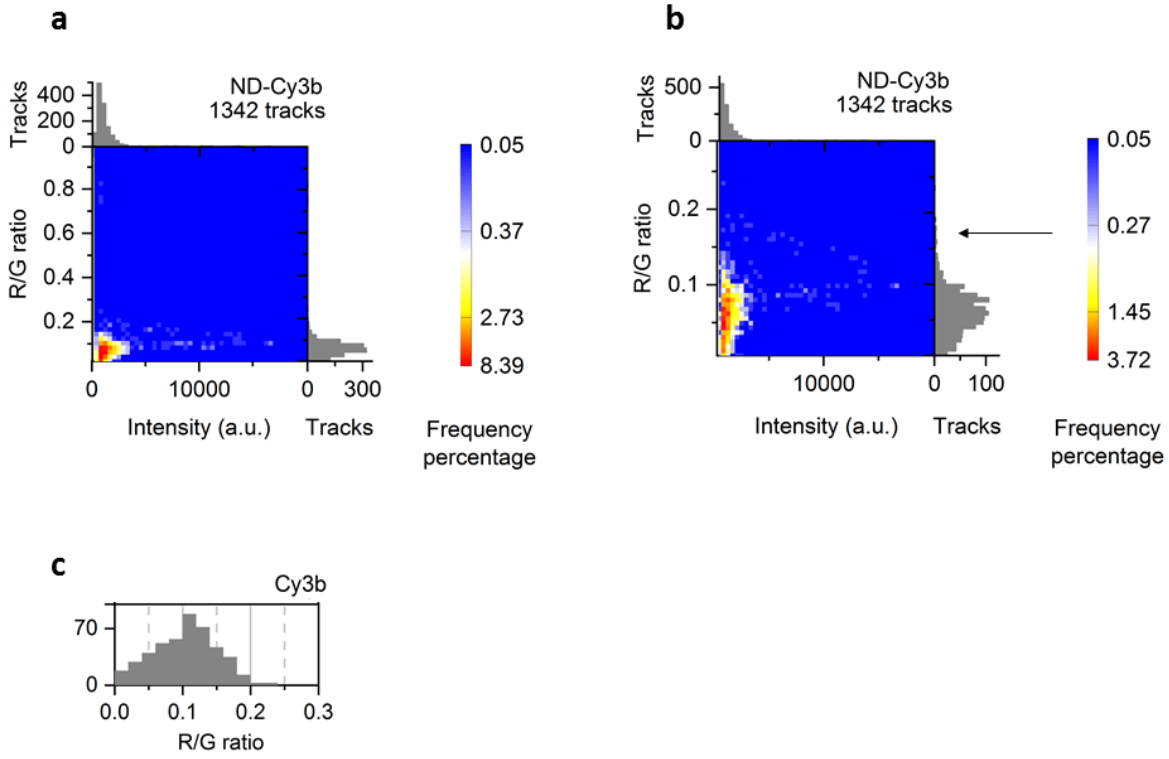

Figure 4.5: R/G ratio for NDs labelled with Cy3b. a, Distribution of the tracks' intensity versus their R/G ratio for labelled NDs (140 W/cm^2, 100 ms exposure). b, enlarged version of the tracks' intensity distribution versus their R/G ratio for labelled NDs. c, Distribution of the track's R/G ratio for free Cy3b (250 W/cm^2, 10 ms exposure).

4.5 Discussion

The size characterisation for 50 and 40-nm particles with SPT provided measurement in good agreement (+/-3 nm) with the expected size and the DLS control. The analysis of the 10 and 5 nm NDs proven to be more challenging as the size was in general overestimated (up to +15 nm). The fact that the hydrodynamic radius found for the 10 nm particles with SPT is 25 nm can be due to either aggregation or an overestimation of the size because SPT can be biased towards larger FNDs if the FNDs population is

not homogenous in terms of brightness. For instance, if the sample contains a small population (*e.g.,* 10%) of 25-nm NDs that contains 2 NV centres per particle, they are at least twice more likely to be detected by the localisation algorithm than the 10 nm NDs containing mostly 1 NV centre per FND, which will also diffuse faster. As a result, SPT can lead to an overestimation of the particle's size when tracking dim and yet fast diffusing NDs. This hypothesis will be proven to be correct in chapter 5. Regarding the analysis of the 5-nm NDs both DLS and SPT showed a diameter superior to the expected size (DLS: +3 and SPT: +8 nm), which shows that the NDs have started to aggregate. Based on the presented data, we demonstrated that SPT is a suitable alternative to measure ND's size distribution provided the sample is bright or large enough (in our case$\geq$ 40 nm). Indeed, it is important for this project to have another technique to measure sizes as DLS analysis is perturbated when the sample contains fluorescent molecules or some large contaminant increasing the size distribution (*i.e.* polydisperse).

TrackCen is an innovative way to characterise the photophysics of diffusing FNDs [112]. Our test on fluorescent beads demonstrated that we are able to detect the expected R/G ratio and that the higher is the intensity and the better is the ratio SD (see figure 4.5). Running this analysis on 40-nm NV-doped FNDs showed a different R/G ratio distribution than when the NDs are immobilised on the glass surface (see figure 3.3). The R/G ratio distribution for the diffusing 40-nm NDs is broader and shows a peak around 0.7 where immobilised 40-nm NDs have a peak at 0.9. This data indicate that the charge state of the NV centre is less stable, which is consistent with the observation that the glass surface is providing electrons to the NV centre as reported by Bradac *et al.* [67]. Nonetheless, we cannot exclude the fact that glycerol may be contributing to the charge instability too. Glycerol is not charged but might have an impact on the surface charge by removing water molecules from the ND's hydration

layer.

The analysis also revealed a subpopulation having both a higher ratio and intensity. Using size measurement, we isolated only the tracks of 40 nm particles and found the same subpopulation; therefore, aggregates could not account for this phenomenon. One explanation is that this subpopulation having a higher R/G ratio corresponds to NV centres in the core of the NDs. This will protect the defect against quenching by the surface or prevent electron transfer from the NV centre to the ND surface. As a result, the crystal defect will not go from NV^- to NV^0 and eventually to NV^+ (non-photoactive, see section 3.3) [98]. If the defect stays in the negative charge state, it will be brighter and emit more in the red compared to unstable NV centres closer to the surface. More data are required to conclude on this last observation but these preliminary results illustrate the potential of our approach for the characterisation of NDs. Moreover, such a technique provides essential spectral insight of NDs in solution, which is a key question when using these nanoparticles for intracellular tracking.

Being able to measure the proportion of FNDs from a given ND sample is an important parameter to know for bioimaging application. For example, if one wants to internalise FNDs for intracellular tracking, the proportion of FNDs has to be known in order to calculate the total amount of NDs to internalise. In the extreme case of detonation NDs in which Reineck *et al.* reported a fraction of 0.03% of FNDs, more than 3000 NDs have to be internalised inside the cell to ensure that there will be at least one FNDs to track; it is clear that such an experiment poses significant challenges as the physiology of the cell will be modified by the addition of such a large volume of NDs even if they have low cytoxicity [90]. So far, the best measurement of proportion of FNDs is usually performed by a combined measurement of the NDs with AFM and confocal microscopy [63]. Such technique is not straightforward, low throughput and requires two types of microscopes. In the last part of the results section, we aimed

to measure the proportion of FNDs with high-throughput and using only one type of imaging (*i.e.* wide-field imaging).

Firstly, the fact that we were able to track the Cy3b fluorescence signal from NDs demonstrated that we are able to successfully conjugate NDs and purify them with no aggregation. This protocol will be useful for the bio-conjugation step in the next chapter. Secondly, regarding the proportion of FNDs in the sample one has to consider the fact that when a ND is labelled with fluorophores, the emission of its NV centre (which is 10 times less bright than Cy3b) has to compete with up to 5000 Cy3b indocarbocyanine molecules from the ND's surface depending on the functionalisation efficiency. Consequently, the red-shift of the NDs containing NV centres is expected to be small. We detected a subpopulation showing a small red-shift (R/G ratio >0.15), which could correspond to NDs containing NV centres. Such subpopulation corresponds to 1.5% of the NDs, which is not very different from the previously reported values (*e.g.*, 5-8% for 100-nm HPHT undoped ND) [67]. Further work is required but our method could be the first one to directly measure the proportion of fluorescent NDs at the single particle level while providing estimation of the size at the same time.

To conclude, using dual-colour SPT we were able to expand the characterisation of NDs with key information on the NDs: hydrodynamic radius, charge stability in freely diffusing NDs and the proportion of FND. The characterisation method we presented in this chapter is not only useful for us to prepare the bio-functionalisation protocol for single-molecule experiment but can be very interesting for material scientists and physicists working on quantum applications of the FNDs. Now that the characterisation techniques are developed, we can use them in our bio-conjugation efforts as presented in the next chapter.

4.6 Materials and methods

Nanodiamond Sample

50-nm HPHT and 5-nm detonation NDs were provided by Prof. Oliver Williams and his team at Cardiff University. In their laboratory, these samples were cleaned by air annealing and sonicated to disperse aggregates. 10 and 40-nm NV-doped NDs were ordered from *Adamas nano* (for more details see section 3.6). All the samples were oxygen terminated and suspended in water. The working concentration was from 30 µM to 150 pM depending on the experiment.

Labelling of nanodiamonds

To investigate the proportion of fluorescent NDs, the nanoparticles were coated with a fluorophore excited by green light (Cy3b). NDs containing NV centres could be detected as they will emit a red signal in addition to the green fluorescence of the Cy3b (see figure 4.4). To conjugate NDs with Cy3b, we incubated the nanocrystals (3.7 nM) with Cy3b molecules having an N-hydroxysuccinimide (NHS) ester function (100 µM) for 3 hours at room temperature. We expected the NHS ester function to execute an electrophilic substitution on the oxygen groups of the NDs' surface such as carboxylic acids or to bind non specifically via hydrophobic interactions as previously reported on carbon nanotubes, which have a very similar chemical structure and composition as the ND's surface [113]. The mixture was purified 10 times from unbound fluorophores using ultracentrifugation at 100000 g (10 minutes 4°C). A negative control containing Cy3b only was performed and did not show any aggregates of the fluorophores (data not shown).

The equation below, derived from Stokes' law was used to estimate the sedimentation rate and choose the appropriate centrifugation speed and duration:

$$v = \frac{d^2 g(\rho_{particle} - \rho_{medium})}{18\eta} \tag{4.2}$$

v is the sedimentation rate, d the ND's diameter, $\rho_{particle}$is the density of the ND, ρ_{medium} the density of the medium (*i.e.* water), g the gravitational force and η the medium viscosity.

Single-Particle Imaging

ND samples (30 µM to 1 µM) were diluted in 80% glycerol and imaged for single-particle tracking (SPT) at room temperature with variable angle illumination (TIRF angle: 40-50° degrees) at least 3 micrometers away from the surface. From 2500 to 70000 frames were recorded depending on the SNR using the microscope described in chapter 3 (see figure 3.1). TrackCen developed by Dr. Barak Gilboa was used to perform localisation and SPT [112]. TrackCen operates in the same way as GapViewer except from a few features; the localisation algorithm implements the centroid method, which is faster than Gaussian fitting and the software also records the displacement of each emitter to calculate their mean square displacement (MSD). The MSD is used to estimate the diffusion coefficient and the hydrodynamic radius of the particle using the Einstein-Stokes equation (see introduction of chapter 4).

Dynamic light scattering (DLS) measurements were done in water using a Viscotek machine; to estimate the diameter of the particles, data from DLS and SPT was fitted using a log-normal function instead of a Weibull function as the bin size provided by the software was systematically logarithmically distributed and could not be changed.

Chapter 5

Biofunctionalised nanodiamonds

5.1 Introduction

Despite the fact that the first bioimaging experimentation with FNDs were conducted in 2005, the impact of FNDs in single-molecule imaging has been limited to method development and proof of principles. More specifically, there have been only three reports of single-molecule experiments using FNDs: two *in vitro* experiments on DNA-FND conjugates [40, 78] and one *in vivo* single-molecule tracking on proteins [39]. As mentioned in chapter 2 (see section 2.4 and 2.5), one of the main limitations of FNDs in single-molecule imaging is their size and their tendency to aggregate in buffers like phosphate-buffered saline (PBS).

When researchers intended to use a FND smaller than the biomolecule of interest, they used 100-nm FNDs to label very long molecules (16.5 μm DNA molecule) [78]. Most proteins of biological interest are around 2-30 nm diameter; consequently, it would be better to use the smallest FNDs available when labelling individual molecules (*i.e.* 10 nm) [77]. However, it is problematic to work with such small FNDs since they have low brightness and a propensity to aggregate. Indeed, the 10-nm NDs will mostly

contain 1 NV centre per ND (see chapter 3 section 3.2), which will require a higher laser power excitation than usual and may cause important phototoxicity when preforming *in vivo* experiments. Phototoxicity can be reduced when using a sensitive microscope with high light collection efficiency and by lowering the time resolution (*i.e.* extending exposure time). The second challenge that small NDs pose compared to 100-nm NDs is that they tend to aggregate more easily; further, such aggregates are also much harder to break up than larger NDs (>50nm). This is because small NDs have a higher surface to volume ratio where electrostatic forces play a more important role than for larger particles. So far, the issue of aggregation has been always tackled by changing the surface chemistry of the ND during the functionalisation process of NDs. Strategies varied from a simple coating with polyethylene glycol [39] to a more complex encapsulation process using silica (see section 2.4) [40]. Changing the surface chemistry to improve the colloidal stability is increasing not only the hydrodynamic radius of the NDs but also the complexity of the functionalisation protocol, which may decrease the yield of the overall functionalisation process.

The experiments detailed in this chapter were conducted in order to address the above-mentioned challenges by combining a simplified functionalisation protocol with sensitive wide-field imaging (see chapter 3) and therefore achieve the production of the smallest functionalised FNDs ever reported. The labelling procedure was inspired by a publication from Be-Ming Chang *et al.* but was extensively shortened because we found that in most cases changing the surface chemistry of the NDs is not required to prevent aggregation of small NDs [80]. With careful optimisation of the protocol we managed to link 10-nm FNDs to a double stranded DNA molecule (∼60 base pair or bp) in order to study the interaction of the DNA with an important enzyme involved in gene expression: RNA polymerase (RNAP).

Understanding how genes are expressed in bacteria (*i.e.* the production of a specific

ribonucleic acid (RNA) or protein from a corresponding gene) is not only essential for fundamental microbiology but also for the design of antibiotics in pharmaceutical industry or in food and agricultural industries. The RNAP is a key enzyme in this process [114]. It is a multi-protein complex (∼20 nm in diameter) that synthesises RNA chains using DNA sequences as templates in a process called gene transcription. The core enzyme is composed of five subunits (β, β', αI, αII and ω) and performs transcription in three main phases: initiation, elongation and termination (see figure 5.1) [114, 115]. Transcription initiation is a well-studied process as it is the first step of gene expression; however, single-molecule studies on transcription initiation are limited by the photobleaching of the fluorescent probes used (less than a second for fluorescent proteins and up to several minutes for small fluorescent organic molecules) [34, 13]. The use of FNDs in single-molecule studies of transcription initiation could lead to great improvements not only in the duration of RNAP tracking *in vivo* and *in vitro* (from seconds to hours of tracking) but also in the temporal and spatial resolution as FNDs can provide a higher photon budget (see equation 2.2 on page 17).

In this chapter we present single-molecule experiments on transcription initiation using 10-nm FNDs. We first describe the optimisation made on the functionalisation protocol, then demonstrate the biological activity from the Cy3-DNA-ND conjugates.

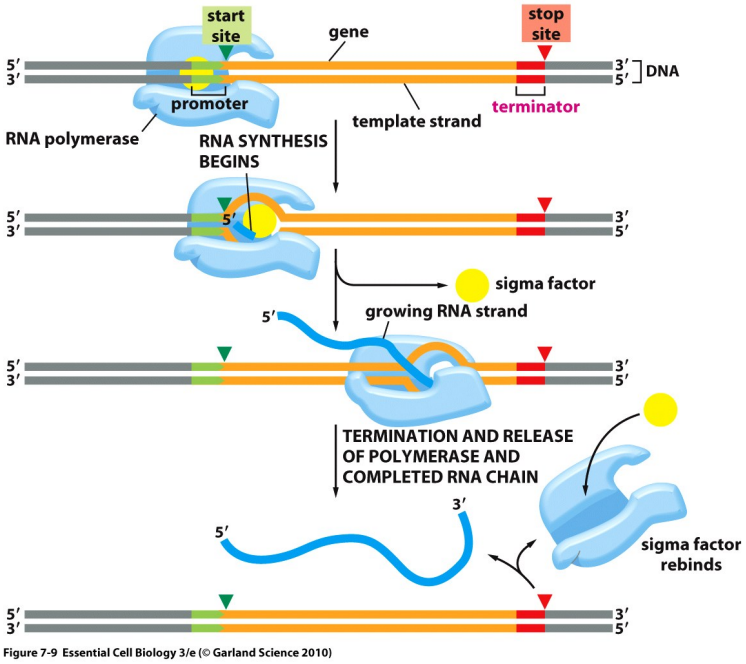

Figure 5.1: Simplified steps of transcription. The initiation phase corresponds to the specific binding of the RNAP to DNA. This phase is only possible with the presence of the σ factor. The extension of RNA to longer lengths is the elongation phase, and the termination occurs when the RNAP dissociates from the DNA.

5.2 Optimisation of the protocol

To investigate DNA-protein interaction with FNDs we attached FNDs to a short DNA strand (60 bp) using a covalent bond created by a bifunctional linker: 1-ethyl-3-(-3-dimethylaminopropyl) carbodiimide hydrochloride (EDC). EDC is known to link two chemical species by reacting with the amine function (-NH_2) of one compound and with the carboxylic function (-COOH) of another chemical (see figure 5.2). Moreover, the DNA strand we selected for this experiment is labelled with a green emitting fluorophore (an indocarbocyanine molecule also called Cy3), which will serve two purposes: to

directly visualise the functionalisation of the ND and to verify the biological activity of the DNA molecule.

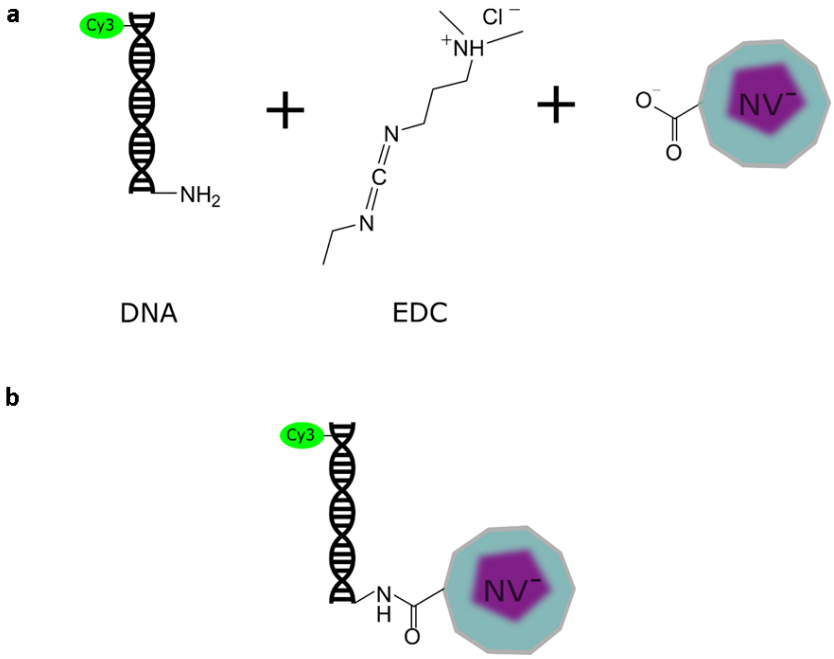

Figure 5.2: ND functionalisation using the EDC bifunctional linker. The presence of carboxylic function in oxygen-terminated NDs is established and was also confirmed by the manufacturer [100].

The labelling protocol described in chapter 4 (see section 4.6) served as a basis to carry out the functionalisation work; nevertheless, attaching DNA molecules to NDs instead of an organic dye (Cy3b) poses few additional challenges that required optimisation. The first issue is that DNA is a biomolecule that ideally requires to be in a buffer solution to preserve its double stranded form. Buffer solutions used to manipulate biomolecules contain salts such as NaCl and KCl in order to stabilise the pH at a given value (*e.g.*, pH 7-8.5). The risk of working with NDs in buffer solutions is that salt can cause ND aggregation [40]. The second problem is that the amount and concentration of labelled DNA is limited compared to organic fluorophores because labelled DNA is more expensive than organic fluorophore. Thus, the protocol has to be improved in

terms of loss and labelling efficiency; this is especially true for the purification step that usually causes significant loss of NDs. Finally, the smaller size of the NDs used (10 nm compared to 50 nm in chapter 4) will make the purification by ultracentrifugation more difficult as the size of the DNA is similar to the NDs (18 nm in length, 60 bp).

There have been many reports on the stabilisation of NDs by chemical treatment since uncoated NDs have been criticised as being unstable in various buffer solutions [65, 46, 72, 116, 117]. Yet, we could not find a study of the NDs colloidal stability (*i.e.* the resistance to aggregation) in the buffer solutions that are mostly used in biochemistry. Such experiment could help us to identify a buffer solution in which both NDs and DNA will be stable. Using the size characterisation methodology we developed in chapter 4 (see section 4.2) we could confirm whether 5 common buffer solutions cause the aggregation of NDs or not (see figure 5.3). The results presented in figure 5.3 revealed that the untreated NDs are actually stable in most of the buffer solutions used (phosphate buffered saline solution [PBS] and KG7 causing a clear loss of colloidal stability [*i.e.* aggregation], see 5.5 on page 86 for details on the buffer composition). MES (2-[N-morpholino]ethane sulfonic acid) and HEPES (4-(2-hydroxyethyl)-1-piperazineethanesulfonic acid) buffers were selected for our functionalisation protocol as their pH range is optimal for not only the coupling reaction (MES pH 4 is ideal for EDC reaction with the carboxylic function of the NDs) but also for the storage of the Cy3-DNA-ND conjugates. TE buffer could not be used as it contains amine that will reduce the efficiency of the EDC linker.

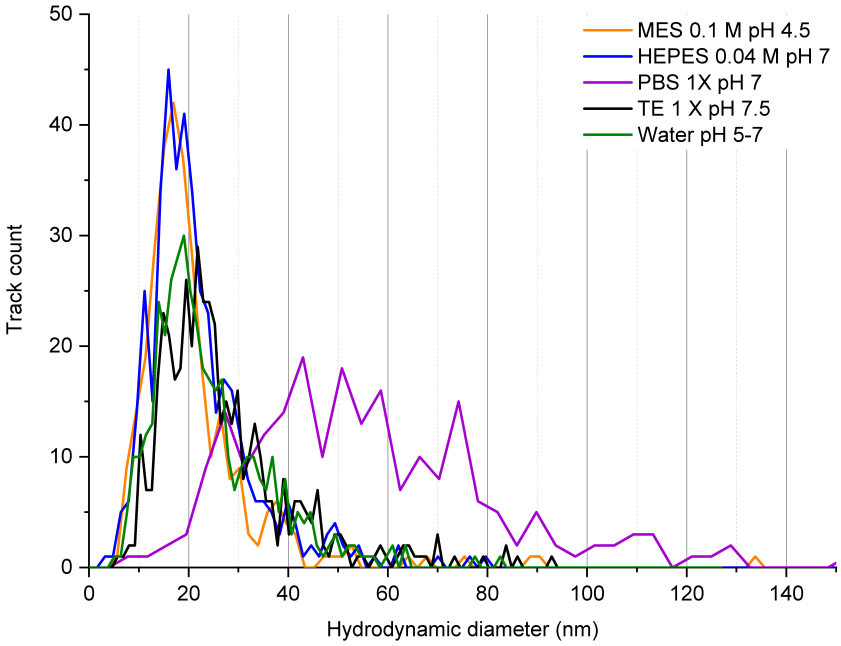

Figure 5.3: Colloidal stability of unfunctionalised FNDs in the most common buffer solutions. The 10-nm NDs were mixed into the buffers for 1-5 minutes and glycerol was added to obtain a 80% glycerol final concentration. The hydrodynamic diameter was estimated from single particle tracking as described in chapter 4 (see section 4.2). KG7 buffer was also tested but caused such large aggregates that they could not be tracked. The expected size of the NDs is between 10-20 nm based on the size characterisation provided by the supplier. All the buffer solutions tested show good stability of the NDs except for PBS and KG7. MES: 2-[N-morpholino]ethane sulfonic acid; HEPES 4-(2-hydroxyethyl)-1-piperazineethanesulfonic acid; PBS: phosphate buffered saline; TE: Tris-EDTA; see section 5.5 for full composition of buffer solutions. The diffusing FNDs were imaged with 532 nm excitation $\backsim$1.3 kW/cm^2 50 ms exposure for 1-2 min.

Using Stokes' law (see equation 4.2 on page 64) we attempted to purify the NDs with 7 rounds of ultracentrifugation (500 000g for 60 min) but could not remove enough free DNA, as shown in figure 5.4. For this reason, we decided to use another approach inspired from the works on gold nanoparticle purification: filtration by centrifugation (Amicon filters) [118]. Amicon tubes contain a porous membrane that can let the DNA through but not the NDs (see materials and method page 86 for more details). Following 8 rounds of centrifugation (5 minutes at 14 000g) the Cy3-DNA-ND conjugates were

well purified from the free DNA, as we only detected the presence of 10-40 nm particles (the expected size of the Cy3-DNA-ND) with no free DNA (see figure 5.4). Because we tracked the Cy3-DNA-NDs via the Cy3 fluorescence from the DNA, we can be confident that the DNA is bound to the NDs. We also performed a control experiment to verify that the DNA is not forming 10-40 nm aggregates that could be misinterpreted as NDs (data not shown).

By finding the right buffer solution and a more suitable purification technique we were able to address the main problems of working with DNA instead of a small organic molecule. Furthermore, the labelling efficiency, which is calculated later in this chapter (see single molecule experiment page 79), was increased by using the N-Hydroxysuccinimide (NHS) compound in addition to EDC in the reaction mix. The next step after making the Cy3-DNA-ND conjugates was to ensure that the NDs or the coupling chemistry did not affect the biological activity of the DNA.

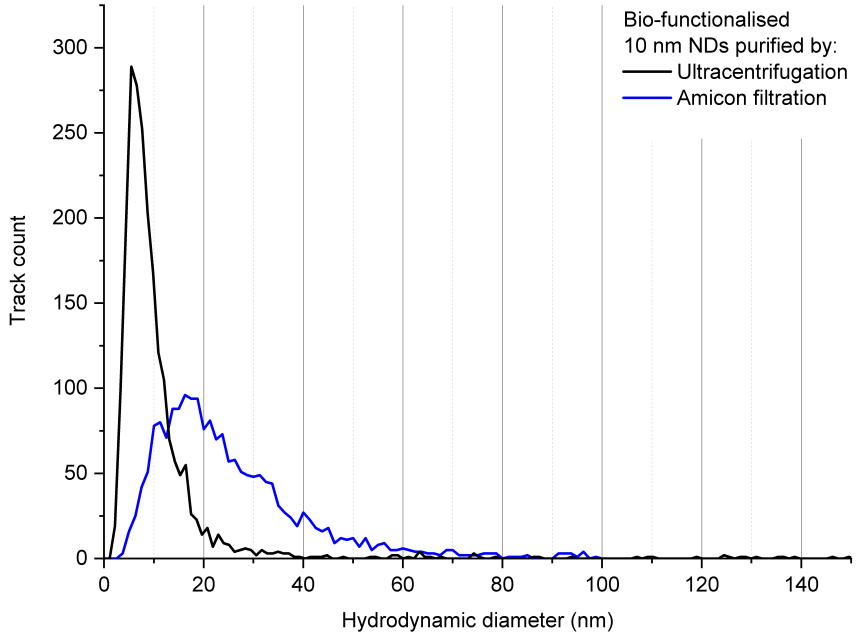

Figure 5.4: Hydrodynamic diameter measurements on the Cy3-DNA-ND conjugates following purification. When purified by ultracentrifugation, the peak of the distribution is around 5 nm, which corresponds to free DNA (the same hydrodynamic size was found when performing SPT on the DNA 18 nm strand - data not shown). In the case of Amicon filtration, the peak is at $\backsim$17 nm, the expected hydrodynamic diameter for the Cy3-DNA-ND conjugates is 10-40 nm. The Cy3-DNA-ND hydrodynamic size distribution is larger than NDs (see figure 5.3) probably because some of the Cy3-DNA-ND conjugates are bound to two or more DNA molecules; single-molecule results later detailed in this chapter will prove this hypothesis to be most likely correct. The difference between the length of the DNA molecule (18 nm) and the hydrodynamic diameter found (5 nm) is due to the fact that the Einstein-Stokes equation assumes that the diffusing molecule/particle is a sphere (see equation 4.1 section 4.1).The diffusing Cy3-DNA-ND were imaged by exciting the Cy3 fluorophore with 532 nm light 0.1 kW/cm^2 50 ms exposure for 1-2 minutes in 80 % glycerol.

5.3 Biological activity of bio-conjugated nanodiamonds

Ensemble measurement

With a view to establishing the biological activity of the DNA strand linked to the ND, we designed an experiment based on the publication by Ko *et al.* [119]. In their report, the team was able to harness a unique property of the Cy3 fluorophore to study the kinetics of the first steps of gene transcription (*i.e.* from DNA to RNA). The beginning of transcription is also called transcription initiation; such bio-molecular process starts by the formation of the holoenzyme, which consists of the RNAP core (formed by the 5 subunits) and the σ factor. The latter is a small protein able to initiate transcription at specific DNA regions [115] once assembled with the RNAP core.

Once the holoenzyme is formed (here abbreviated RNAP), it can proceed to the transcription initiation, a complex process that can be simplified into the 4 steps described below.

- Promoter binding: the RNAP binds specifically to a given sequence in DNA called a promoter sequence (see figure 5.5a).

- Promoter melting: the RNAP separates locally the two DNA strands to carry out the transcription (see figure 5.5a). The region where the double strand DNA is open is termed the transcription bubble and is approximately 12 bp long. Since the DNA is opened, the macromolecular structure formed by the DNA and the RNAP is called the open complex. The opening of DNA (a.k.a. DNA melting) is necessary as the incoming nucleotides need to bind to the DNA template strand for transcription to occur.

- Abortive transcription: the RNAP transcribes a few base pairs but fails to move away from the promoter.

- Promoter escape: the RNAP moves away from the promoter, thus closing the transcription bubble while the enzyme continues to transcribe the gene.

Ko *et al.* aimed to study the kinetics of promoter escape by measuring the change in the fluorescence of Cy3. The photoluminescence of Cy3 is greatly affected by the local environment: fluorescence intensity of a Cy3 molecule linked to a single-strand DNA is approximately twice that of Cy3 linked to a double-stranded DNA. The exact origin of this behaviour is still unclear but it has been established that the environmental sensitivity of Cy3 is ascribed to its cis-trans photoisomerisation. The Cy3 trans isomer has a larger absorption cross section causing the trans isomer to be brighter than the cis conformation. Based on this information and a recent report by Rashid *et al.*, we hypothesise that because of the RNAP binding and formation of the open complex, Cy3's local environment undergoes an increase of viscosity preventing the photoisomerisation of the Cy3 and increasing the fluorescence intensity in a single strand DNA [120]. In addition to this process, the Cy3 molecule in the single strand is free from a partial nucleic acid induced quenching in the double stranded DNA giving rise to an even greater fluorescence enhancement [120].

The experiment by Ko *et al.* that we aim to replicate with our Cy3-DNA-NDs conjugates consists of measuring the fluorescence change of an ensemble of Cy3-DNA molecules as RNAP is added to the solution. The fluorescence increase caused by the RNAP binding and formation of the transcription bubble (see diagram in figure 5.5a) is shown in figure 5.5b. We performed the same experiment using our Cy3-DNA-ND conjugates and also found a fluorescence enhancement when RNAP is added (see figure 5.5c). The increase of fluorescence is lower than for the Cy3-DNA only: fold change of 1.2 for Cy3-DNA-ND compared to 2 for Cy3-DNA. A possible cause for a lower biological activity of the Cy3-DNA-NDs is the fact that a proportion of the Cy3-DNA molecules have non-specific interactions with NDs preventing the formation of the open

complex.

Data presented in figure 5.5c show clearly that some of the Cy3-DNA-NDs are active and not free Cy3-DNA as the Cy3-DNA-NDs were purified just 2 hours before the fluorescence measurements. In order to further rule out that the photoluminescence enhancement was merely caused by free Cy3-DNA we also preformed single-molecule measurements on the Cy3-DNA-NDs.

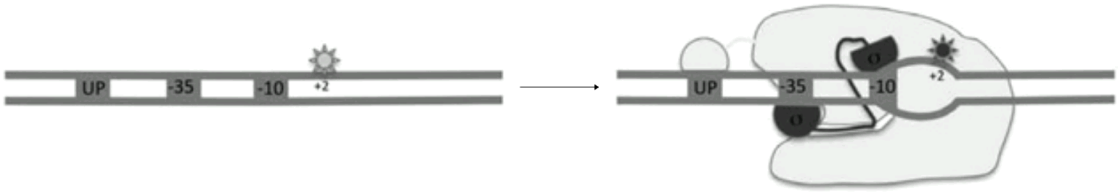

(a)

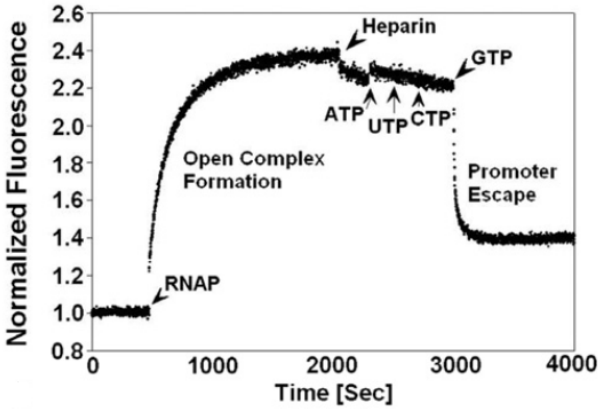

(b)

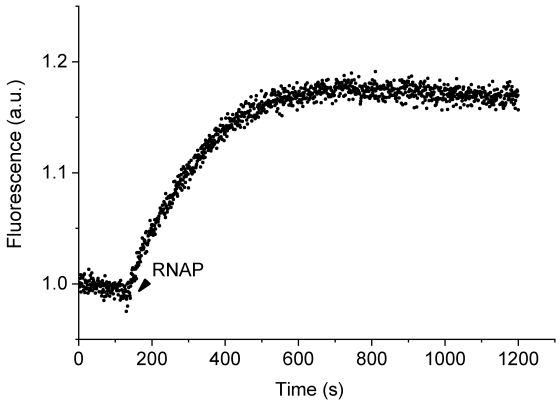

(c)

Figure 5.5: Real-time ensemble measurement of the open complex formation. a, diagram of the fluorescence assay from the publication of Ko *et al.*. UP: upstream promoter, and -35 and -10 indicates promoter sequences interacting with the RNAP. The Cy3 probe is indicated by a little sun at position +2 (with +1 being the position of the first bp transcribed). On the right diagram, the σ factor is indicated in dark grey while the RNAP core is shown in light grey. b, time course of the fluorescence change of Cy3 labelled DNA upon the addition of the RNAP. The fluorescence increases two fold as the open complex is formed. Heparin is added to confirm the specificity of RNAP-DNA interaction and once all the nucleotides (*i.e.* building blocks of RNA: ATP, UTP, CTP, GTP) are added for the RNAP to end transcription initiation, promoter escape leads to a fluorescence decrease as the transcription bubble collapses (data from Ko *et al.*). c, time course of the fluorescence change of Cy3-DNA-ND conjugates upon the addition of the RNAP. Following the addition of the RNAP after $\backsim$ 2 minutes the fluorescence increases in a timescale (<1000s) comparable to the one in figure b. Excitation 540 nm, emission wavelength 563 nm, integration time 1 s.

Single-molecule characterisation

With the help of single-molecule imaging we could measure the labelling efficiency, characterise the photophysics and the biological activity of the Cy3-DNA-NDs conjugates. To make sure that we are working with Cy3-DNA-FNDs all the data presented in this section are from Cy3-DNA-NDs from which the Cy3 emission colocalises with NV fluorescence. The procedure we used to collect Cy3 and NV time traces from single Cy3-DNA-ND particles is presented in figure 5.6. Using such sequential single-molecule measurements, we could count the number of FNDs functionalised with Cy3-DNA as they show typical Cy3 fluorescence. We estimated that the labelling efficiency (using NHS + EDC) can be as high as 30 % while the negative control (DNA + ND with no EDC + NHS) showed lower labelling efficiency (approximately two times less than with EDC + NHS). Our results suggest that Cy3-DNA can adsorb on the NDs in a non-specific manner and that our labelling efficiency estimates might include some adsorption instead of covalent bonding.

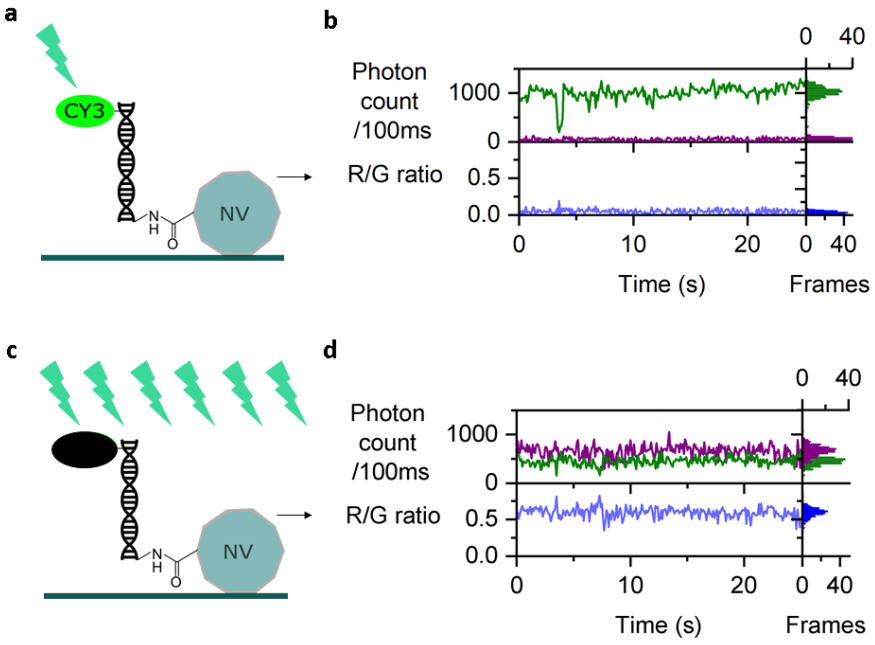

Figure 5.6: Single molecule imaging of the Cy3-DNA-ND conjugates. a, Cy3 probe is excited with relatively low laser power. b, typical time-trace of a Cy3 probe. c, high laser power is used to photobleach the Cy3 probe and excite the NV centre. d, NV centre time-trace that colocalise with the Cy3 signal shown in b. NV and Cy3 fluorescence can be easily distinguished as Cy3 does not emit in the red channel. It is very unlikely that a Cy3-DNA-NDs or free Cy3-DNA happened to be next to a FND because the density of NV localisations is low (localisations per field of view of 50x80μm: Cy3 <1000 and <100 FNDs). The Cy3-DNA-ND conjugates are immobilised on the glass surface by electrostatic forces and are imaged in imaging buffer containing oxygen scavenging system (see materials and method page 86). 532 nm excitation, 100 ms exposure 25 sec: Cy3: 0.1 kW/cm^2 NV$^-$: 1.6 kW/cm^2.

Following the estimation of the labelling efficiency, we then characterised the fluorescence's intensity distribution of the Cy3-DNA-FNDs. First, we needed to study the photon count distribution of the NDs after EDC reaction to make sure that we can interpret confidently the data from the Cy3-DNA-FNDs (for details on the EDC+ND preparation, see materials and method page 86). Controlling the fluorescence of unfunctionalised NDs is important as there are multiple reports of bright and unstable fluorescence originating from NDs surface defects involving graphitic structures [90, 121, 117].

Our analysis of unfunctionalised NDs revealed green fluorescence brighter than the NV centre and photobleachable within a few seconds (data not shown) when exciting with low laser power (0.78 kW/cm^2) as displayed in figure 5.7. Fortunately, the photon count produced by the surface defects is low (>500 photons/100 ms) compared to what was measured from a single Cy3 molecule ($\backsim$ 1000 photons/100 ms see 5.6 page 80). Therefore, we excluded time-traces lower than 900 photons/100 ms to avoid surface defects interfering with our investigation.

The photon count distribution from Cy3-DNA-FNDs without the RNAP is broad (1000-6000 photons/100 ms) with a main peak at 1500 photons/100 ms (see figure (5.7)b). We attributed the principal peak to Cy3-DNA-FNDs attached to a single Cy3-DNA molecule as a photon count of $\backsim$1000/100 ms is expected from Cy3 DNA and surface defects from the same Cy3-DNA-FNDs might participate in the photon count up to 1500 photons/100 ms. The other peaks found in the histogram ($\backsim$ 2200, 3000 and 5500) are more difficult to interpret and such analysis is beyond the objective of the experiment. Nonetheless, the fact that the distribution is broad with other peaks suggest that some of the Cy3-DNA-FNDs are attached to multiple Cy3-DNA molecules (up to 5).

When the RNAP is added to the imaging buffer, the distribution becomes even broader including brighter emitters than without the RNAP (>6000 photons/100ms, see figure 5.7c). Moreover, the peak at 1500 photons/100 ms is now almost as high as the peak at 2200 photons/100 ms, indicating that the proportion of emitters at 1500 photons/100 ms is relatively smaller compared to Cy3-DNA-FNDs without RNAP (see figure 5.7b). The presence of brighter emitters and the smaller proportion of particles emitting 1500 photons/100 ms confirm that the Cy3-DNA attached to the FNDs is still able to bind to the RNAP as shown in the previous section by ensemble measurement (see page 74). The other finding (from fluorimeter analysis) that our experiment cor-

roborates is the fact that not all the Cy3-DNA-FNDs are biologically active. Indeed, after RNAP incubation the peak at 1500 photons/100 ms is still visible, which means that some of the Cy3-DNA-FNDs did not interact with the RNAP probably because of non-specific interaction of the Cy3-DNA with the FND's surface. We also excluded the possibility of some non-specific photophysical effect of the RNAP by showing that a decrease of fluorescence occurs when the RNAP dissociates from the Cy3-DNA (data not shown).

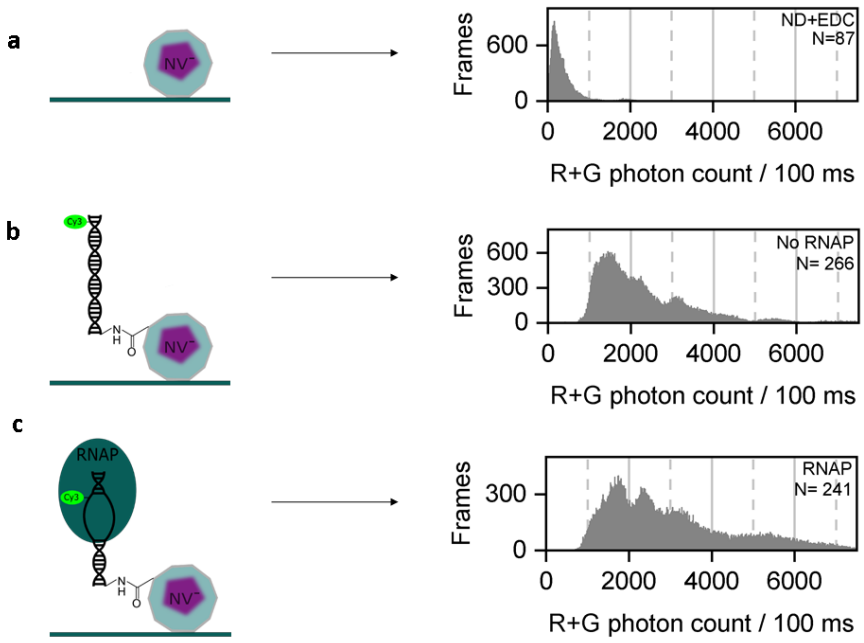

Figure 5.7: Photon count distribution of unfunctionalised FNDs and Cy3-DNA-FNDs (with and without RNAP). a, NDs treated with EDC. The photon count distribution shows that most of the emitters have a photon count of between 150 and 350 photons/100 ms. b, Cy3-DNA-FNDs without RNAP. The Cy3-DNA-FNDs show much brighter emitters that we attributed to Cy3. Only the emitters showing a photon count/100 ms >900 are shown here to exclude fluorescence from the surface defects shown in a. c, Cy3-DNA-FNDs with RNAP (0.35µM following 5-10 minutes incubation at room temperature). The photon count distribution contains brighter emitter thus confirming the biological activity of the Cy3-DNA-FNDs. Likewise, only the emitters showing a photon count/100 ms >900 are shown. The NDs and Cy3-DNA-FNDs conjugates are immobilised on the glass surface by electrostatic forces and are imaged in imaging buffer containing oxygen scavenging system (see materials and method page 86). 532 nm excitation, 100 ms exposure 25 sec. To image Cy3 and surface defect the irradiance was: 0.1 kW/cm^2. In order to image NV$^-$(only for colocalisation) with Cy3 or the surface defects, an irradiance of 1.6 kW/cm^2 was used. Most of the photons are coming through the green channel (data not shown) as expected from the Cy3 (see figure 5.6 page 80).

5.4 Discussion

In this chapter we presented our efforts to attach the FNDs to a Cy3-DNA molecule. Thanks to an optimisation of the labelling protocol, we could form 17-nm Cy3-DNA-FNDs conjugates from 10-13 nm FNDs with sufficient efficiency for us to perform single-molecule experiments and demonstrate their biological activity. It is the smallest bio-functionalised FNDs ever produced, as previous reports used larger FNDs: Bumb *et al.*: 30 nm, Liu *et al.*: 40 nm, Teeling-Smith *et al.*: 100 nm [40, 39, 78]. In order to successfully implement FNDs in single-molecule imaging, it is paramount to be able to work with the smallest FNDs available (*i.e.* 10-nm NDs, since the 5-nm NDs show very little fluorescence see section 3.2 on page 33 in chapter 3) as most of the biomolecules that biologists would like to study are relatively small (2-30 nm).

In addition to providing a protocol to functionalise sub-20 nm FNDs, we also provided a valuable information for ND researchers: a comparable study of the stability of small FNDs in the most common buffers used in biochemistry. Surprisingly only PBS and KG7 buffer led to the aggregation while the other buffers (HEPES, TE and MES) did not affect the colloidal stability of the FNDs. Raw NDs are often described as unstable for biological applications but our findings suggest that in certain buffer solution, raw NDs can be simply used without any further modification of their surface chemistry. Such information will be useful for researchers working not only on bioimaging but also on drug delivery as NDs have been shown to be suitable carriers for intracellular delivery of drugs [65]. The explanation for KG7 and PBS causing aggregation is not clear but we noticed that both of these buffers contain divalent ions (mM concentration is of $HPO4^{2-}$ and Mg^{2+}) unlike TE, HEPES and MES. Further assays are required to elucidate how NDs aggregate in KG7 and PBS, but a likely cause is the interaction of a divalent ion with negative carboxylic functions (COO^-) from two different NDs thus producing a non-covalent crosslinking between the NDs and eventually their aggregation.

Having stable suspension of sub-20-nm Cy3-DNA-FNDs is not the only requirement for the biofunctionalisation to be successful, we also had to test its biological activity. Indeed, for the Cy3-DNA-FNDs to be used in transcriptional studies, the Cy3-DNA molecules have to be able to bind to the RNAP. Inspired by previous works on transcription initiation [119, 122], we used the environment sensitive fluorescence of Cy3 to show at macroscopic and microscopic level that the RNAP is able to interact specifically with the Cy3-DNA-FNDs to perform the first steps of transcription initiation (*i.e.* binding and melting of the promoter). We also note that only Liu *et al.* actually showed that their biofunctionalised FNDs were biologically active while the two other articles reporting single-molecule experiments did not test the functionality of the biomolecule attached to the FNDs [40, 78, 39].

Our control sample where Cy3-DNA was mixed with just NDs revealed that Cy3-DNA adsorbs to the NDs. This was expected as the ability of NDs to non-specifically interact with nucleic acid has already been reported [123]. Nonetheless, labelling efficiency was two times higher (up to 30%) when EDC/NHS was used, which suggests that the covalent binding has occurred. Furthermore, the fact that the RNAP can bind to the Cy3-DNA-FNDs and melt the promoter also supports the assumption that the Cy3-DNA is covalently bound to the FND. It is also consistent with our observation that not all Cy3-DNA-FNDs are biologically active as this inactive population of Cy3-DNA-FNDs could be the one formed by merely adsorption. Although we cannot exclude the scenario of adsorbed DNA reacting with the RNAP, it is a less likely scenario as the adsorbed Cy3-DNA strand will be less accessible to the RNAP because the Cy3-DNA will bind to the DNA in many different orientations and positions. Still, it is difficult to estimate how much of the Cy3-DNA-FNDs are formed by covalent reaction vs adsorption; single-particle tracking experiments with different concentration of salts could force the adsorbed Cy3-DNA molecules to dissociate and permit us to measure

the fraction of Cy3-DNA strand bound to NDs.

5.5 Materials and methods

DNA construct

The double stranded Cy3-DNA was prepared from two single strands synthesised by IBA having the following sequence: non-template strand 5'-(C6-NH_2)GAA ATT GTT ATC CGC TCT CAC AAT TCC ACA CAT TAT ACG AGC CGA AGC ATA AAG TGT CAA GCC T-3', template strand including a promoter sequence 5'-AGG CTT GAC ACT TTA TGC TTC GGC TCG TAT AAT GTG TGG AXT TGT GAG AGC GGA TAA CAA TTT C-3' with X being a thymine base labelled with Cy3. Both oligonucleotides were annealed at and diluted at 2.6 µM in sodium borate buffer 50 mM pH 9.5 just before using the DNA to functionalise the NDs.

Bio-functionalisation of NDs

For the tracking experiment to explore the stability of NDs in buffers we used the following recipes: PBS pH 7: 137 mM NaCl, 2.7 mM KCl, 8 mM Na_2HPO_4, and 2 mM KH_2PO_4; TE pH 7.5 10 mM tris(hydroxymethyl)aminomethane (tris) and 1 mM ethylenediaminetetraacetic acid (EDTA). For KG7 composition see the protocol for single-molecule imaging below.

The 10-nm NDs (concentration estimated to 117 nM) were diluted into MES buffer (0.1 M MES (2-[N-morpholino]ethane sulfonic acid, pH 4.5) and mixed with EDC. Sulfo NHS was also added to improve the labelling efficiency as it is known to form a semi-stable sulfo NHS ester with the EDC-activated carboxylic functions, which can react more efficiently with the amine function of the Cy3-DNA molecules. After 15 minutes incubation under stirring (650 rpm at room temperature), pH was adjusted to

9.5 by exchanging MES buffer with sodium borate buffer (50 mM) using Amicon filters (100KDa). Cy3-DNA was added and left overnight under stirring (650 rpm) in the dark at room temperature. In the case of the control sample with no EDC and no NHS, the DNA was directly added to the ND suspension while the ND + EDC (No DNA) control was made using NDs and EDC only. The negative controls were also left overnight in the dark under stirring (650 rpm) at room temperature. The concentrations for all the reagents were adjusted to respect the following number of molecules for 1 ND: 100 Cy3DNA, 10^6 EDC and 2.5 x 10^6 NHS. The sample was then purified using 7 rounds of washing in 100KDa Amicon filters and then stored at -20°C in HEPES pH 7.

Fluorimeter measurements

A fluorimeter from PTI was used to perform ensemble measurements. Light excitation was performed at 540 nm and the fluorescence emission was collected at 563 nm (emission slit 6 nm, detector slit 6 nm, gain 800-1000). One data point per second. The presence of Cy3 emission spectrum was verified before carrying out the promoter melting experiment (data not shown). A 50 µL reusable cuvette was used to carry out the promoter melting experiment. The concentration of the RNAP was approximately 14 times higher than the Cy3-DNA-FNDs and the experiment was done in HEPES buffer.

Single-molecule imaging

Tracking and immobilised single-molecule experiments were also performed on a Nanoimager S (see materials and methods chapter 3 page 49). Single-particle tracking was performed as described in chapter 4 (see material and methods page 64) but the tracking software used in this chapter was provided by *Oxford Nanoimaging* and the laser power used was lower to prevent Cy3 photobleaching (532 nm excitation at 7-1.4 kW/cm^2).

The Cy3-DNA-FNDs were immobilised on a glass surface using either spin coating or drop casting; silicon gaskets were used to form wells and 30 µL imaging buffer was added to the wells (imaging buffer: KG7 buffer containing 2 mM Trolox, 12.5 µM glucose oxidase, 16 nM catalase, and 8 mM D-glucose; KG7 buffer: 40 mM HEPES-NaOH, 100 mM potassium glutamate, 10 mM MgCl2, 1 mM dithiothreitol, and 5% glycerol). Glucose oxidase and catalase was always added just prior to recording and the RNAP promoter melting experiment recordings were done in a different well between each condition (with or without the RNAP). 7 µL of RNAP holoenzyme from NEBiolabs was added to the well in order to have excess of RNAP and the well was left to incubate for 5-10 minutes at room temperature before recording.

Chapter 6

Nanodiamonds for multimodal imaging

6.1 Introduction

How close are we from being able to detect the magnetic fluctuations produced by a single biomolecule in its native form? Since the works of Balasubramanian *et al.* and Maze *et al.* NV centres in diamond have been used as a nanosensor for varied applications including bio-sensing (*e.g.,* temperature measurement inside living cells, for more details see section 2.5 on page 28) [25, 26, 58]; however, researchers working on NV quantum sensing have been pursuing an important goal: the label-free detection of a single biomolecule in its native form. The possibility to measure the magnetic fluctuations produced by a single biomolecule could make significant contributions to the field of single-molecule experiments as it would be a label-free technique that will not be limited by photobleaching. Such a single-molecule approach could be used to study not only bio-molecular interactions but also conformational changes in proteins or DNA. Much progress has been done towards achieving single-molecule detection

with NV centres, but a couple of challenges remain to be addressed when performing optically-detected magnetic resonance (ODMR) in a biological context.

ODMR based sensing approaches rely on the difference in the absorption and emission properties of the NV centre spin sub-levels: $m_s = 0$ and $m_s = \pm 1$ (see chapter 2 figure 2.2 on page 23). More precisely, $m_s = 0$ is 10-30% brighter than $m_s = \pm 1$; as a result, when a 2.87 GHz microwave excitation drives a transition from $m_s = 0$ to $m_s = \pm 1$, a drop of fluorescence can be observed (see figure 6.1b first ODMR spectra from the bottom). The decrease of fluorescence at resonant frequency is used to measure the difference between the energy levels $m_s = 0$ and $m_s = \pm 1$, but in presence of an external static magnetic field the degenerate $m_s = \pm 1$ level splits into two levels $m_s = +1$ and $m_s = -1$ (see splitting from the second ODMR spectra in figure 6.1b). The energy difference between the two levels $m_s = +1$ and $m_s = -1$ is proportional to the external magnetic field due to the Zeeman interaction. Therefore, it is possible to measure the projection of the external magnetic field on the symmetry axis of the defect using the following equation:

$$B = \frac{h\Delta_\nu}{2g\mu_B} \tag{6.1}$$

Where h is the Planck constant and Δ_ν is the difference between the $m_s = 0$ and $m_s = \pm 1$ sub-level resonant frequencies (not to confound with Δ_ν in 6.1b) [24]. More sophisticated techniques are available such as pulsed ODMR to improve the sensitivity of the magnetometry measurement down to 500 nT $Hz^{-1/2}$ for an AC magnetic field [26, 24]. Further, pulsed measurements allow to probe electron-electron coupling, thus it is possible to investigate the interaction between a NV centre and a spin label. Using such approach, the detection of a single spin-labelled biomolecule using NV centre has been achieved recently [124].

Shi *et al.* reported in 2018 the successful detection of the magnetic field produced

by a single spin-labelled DNA molecule in a buffer solution [125]. To do so, they immobilised a spin-labelled DNA molecule within a 10 nm distance of an NV centre located inside a diamond nanopillar. The nanopillars are nanoscale structures (about 400 nm in height) etched from bulk diamond in order to improve light collection efficiency from the NV centre located at the top of the pillar. The ability to detect electron spin resonance from a spin-labelled DNA molecule in aqueous buffer solutions and at ambient temperature is a great step toward performing magnetic resonance on unlabelled single-molecules; nonetheless, there are some limitations to the aforementioned publication. Firstly, the use of spin label hinders the potential of the technique as it will require covalent modification of the molecule of interest every time a new biomolecule is studied. Further, specific chemical modification of proteins is relatively more challenging to carry out as it may impair its functionality. Secondly, despite the fact that NV centres in bulk diamond are the best option when performing electron spin resonance because of their enhanced photophysical properties (*e.g.,* charge stability), such material is not very compatible with *in vivo* investigations. FNDs are better suited for *in vivo* quantum sensing and they have already been successfully used for quantum measurement inside living cells [83, 82, 58]. However, none of these FNDs *in vivo* sensing investigations account for the study of biomolecules, but instead, they focus on temperature or orientation measurement.

If the long-term goal is to study individual biomolecular interactions *in vivo* with ODMR, we first need to be able to track biomolecules using FNDs fluorescence. As mentioned in the introduction (see section 2.4 on page 26), intracellular single-molecule tracking using NDs has only been reported in eucaryote cells [39]. Such cells are large enough (*e.g.,* 30 µm) for large NDs (up to 100 nm) to be used and have enough intracellular volume to diffuse in. Yet, bacteria like *Escherichia coli* (*E. coli*) is a better biological model when one wants to investigate fundamental gene expression mecha-

nisms as it is an easier organism to work with. As our Cy3-DNA-NDs were designed to study gene transcription (see introduction chapter 5 on page 66) we decided to perform *in vivo* single-molecule experiments with our ND conjugates in *E. coli*.

ND bioimaging in bacteria is more challenging because their small cells (1-3 μm long) limit the size and brightness of NDs that can be used. For instance, a 100 nm NDs would be difficult to internalise and will struggle to diffuse inside the cytoplasm. So far, there have been only two publications on ND imaging with bacteria; the first one was in published in 2007 in which *E. coli* cells were introduced to ND-lysozyme complexes to determine their antibacterial properties [70]. The aim of the experiment was to see if NDs could improve the delivery of lysozyme to *E. coli*; furthermore, the authors imaged the NDs in contact with cells by detecting a characteristic signal in the light scattered by the diamond (*i.e.* Raman signal). Chao *et al.* did not observe any internalisation of the NDs, but in 2014, Wehling *et al.*, who were also interested in the antibacterial properties of NDs, managed to show intracellular aggregates of detonation NDs inside *E. coli* cells [74]. By simply incubating bacteria with detonation NDs for 15 minutes, they were able to incorporate ND aggregates inside the cells as shown by transmission electronic microscopy (TEM). On one hand, the advantage of TEM is to not rely on the presence of the fluorescent NV centres but on the other hand it is not possible to perform any live cell imaging as measurements are done on ultrathin sections of the sample. Fluorescence microscopy has the advantage to be compatible with live-cell work and that is why the report by Hemelaar *et al* in 2017 is the most relevant study to our research project so far. Using a very short electrical pulse (0.9 kV), they were able to permeabilise the cell membranes for a short instant in order to incorporate 70-nm FNDs inside yeast cells (*Saccharomyces cerevisiae*) [71]. The use of electrical shocks to permeabilise cells is called electroporation. It has been used to deliver different materials into cells, but not with FNDs until then [126, 127]. The presence of FNDs in

the yeast's cytoplasm was confirmed by fluorescence microscopy using the NV centre's characteristic emission but no single-particle tracking was performed.

In this chapter we first present relevant results towards achieving ODMR on a bio-functionalised FND with a view to detecting the magnetic field of a biomolecule in its native form. We demonstrate that the functionalisation of FNDs destabilises the charge state of the NV centre thus making ODMR on Cy3-DNA-FNDs impossible. Secondly, we present the first observations of intracellular single-molecule tracking inside *E. coli* cells using electroporated Cy3-DNA-FNDs. The electroporation protocol and data analysis methodology presented here pave the way for long term single-molecule tracking in bacteria to study real-time gene transcription during an entire cell cycle and possibly for hours.

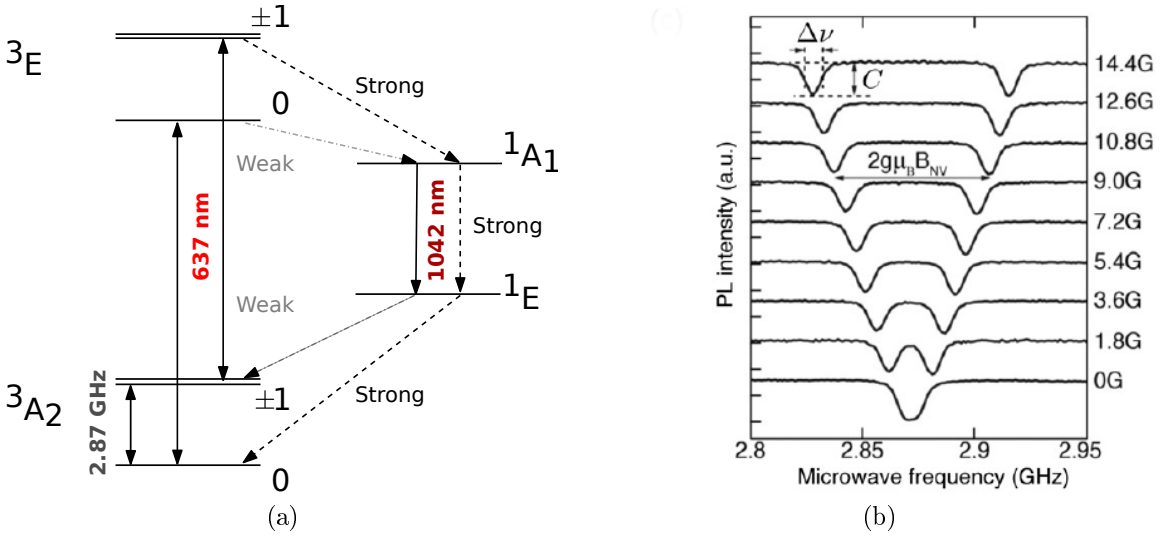

Figure 6.1: (a) Energy level scheme. Optical transitions are shown with solid arrows while the dashed arrows indicate spin selective intersystem crossing (ISC) involving the singlet states $^1A_1$ and ^1E (for more details see chapter 2 figure 2.2 on page 23). (b) Reproduction of the figure in the publication by Rodin *et al.* 2014. ODMR spectra recorded for different magnetic field magnitudes applied to a single NV defect in diamond. The spectra are made by recording the fluorescence intensity while changing the frequency of the microwave excitation [24].

6.2 ODMR on bio-conjugated nanodiamonds

Shazeea Ishmael from Jason Smith's laboratory (Oxford Materials department) performed the ODMR measurements on the 10-nm FNDs in air and on the bio-functionalised FNDs in imaging buffer. The ODMR spectra shown on figure 6.2 presents a zero-field splitting (ZFS) signal at 2.82 GHz for the raw NDs in air. Following our discussion with Jason Smith, we do not know why the peak is found at 2.82 GHz instead of 2.87 GHz but we know this signal corresponds to the ZFS as we observed a splitting of the peak when an external magnetic field is introduced (data not shown). When performing the ODMR on the functionalised NDs (Cy3-DNA-ND) no decrease of the fluorescence was

observed even with a higher number of sweeps accumulated (see figure 6.2 middle spectrum). Nevertheless, the sum of the sweep 40-50 (from the 191 sweeps in the middle spectrum) shows a slight drop of fluorescence at 2.88 GHz, which suggests that charge fluctuation might be responsible for the poor contrast in the measurement.

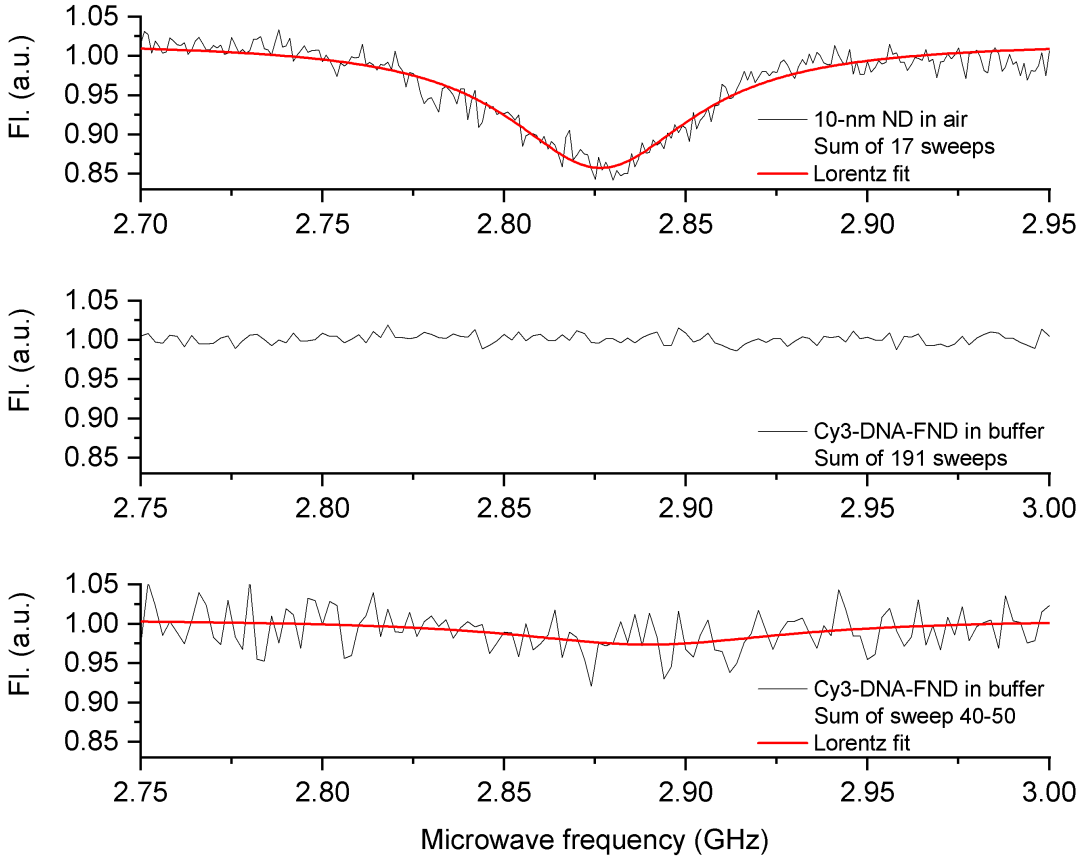

Figure 6.2: ODMR spectra on raw and functionalised single 10-nm FNDs. The spectrum on 10-nm NDs particle in air presents a drop of fluorescence at 2.82 GHz with good contrast ($\backsim$15% decrease in fluorescence). No decrease of fluorescence is detected for the functionalised FNDs (Cy3-DNA-FND). A slight drop of photoluminescence can be observed at 2.88 GHz when taking only the average of the sweep 40 to 50 from the 191 sweeps in the middle spectrum. Fl.: Fluorescence.

6.3 The effect of bio-conjugation on the NV centre

In the previous section, we were able to record a ZFS signal in the raw FNDs but not from the biofunctionalised sample; consequently, we decided to investigate whether the functionalisation protocol may cause charge instability. The charge state of the NV centre in the Cy3-DNA-FNDs was measured in imaging buffer using the method presented in chapter 3 (see section 3.2 on page 33). The R/G ratio distribution from the raw 10-nm FNDs (top histogram) in imaging buffer has a peak around 0.55, which is 0.15 lower than the value reported in figure 3.3 on page 37 (peak at 0.7). We also observed a lower R/G ratio for the 10-nm NDs in water (-0.17) compared to the data presented in chapter 3. This difference of 0.15-0.17 is due to the change of microscope between this chapter and chapter 3. The microscope used for the analysis presented here has probably different filters and/or sCMOS, which results in lower R/G ratio values although the same FNDs are imaged. Considering this 0.15 offset caused by a change of microscope, the R/G distribution of raw FNDs in imaging buffer is similar to the one described in chapter 3: unstable with sub-100 ms fluctuation between NV^- and NV^0. Interestingly, the R/G ratio distribution of Cy3-DNA-FNDs (bottom histogram) is shifted to lower values ($\backsim$0.4) indicating that NV^0 is the main charge state of the NV centre in bio-conjugated FNDs. We further analysed whether DNA or only EDC is destabilising the NV centre and found that charge instability can be produced by EDC only (see measurements in air, figure 6.4 on page 98).

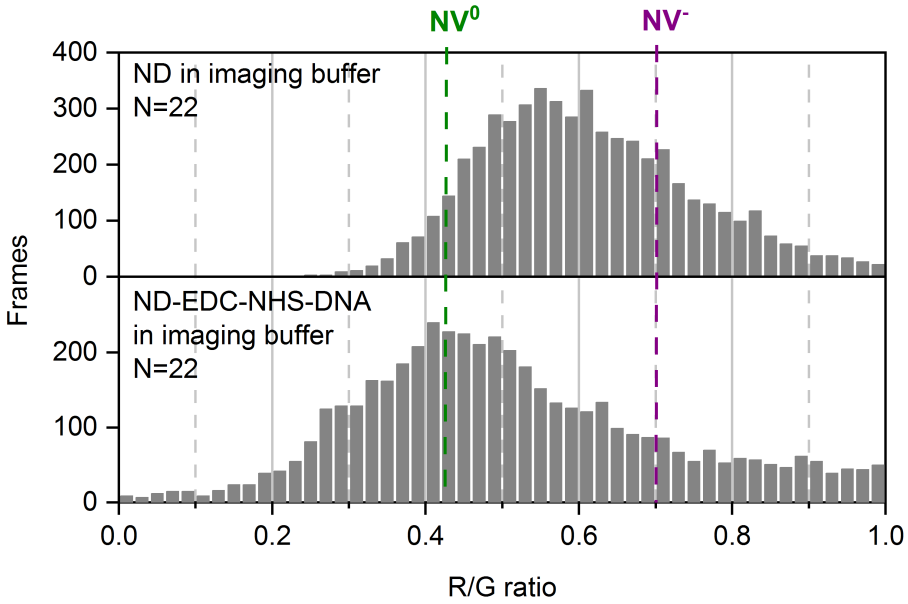

Figure 6.3: R/G ratio distribution of the NV centre in raw 10-nm FNDs and following bio-functionalisation (ND-EDC-NHS-DNA). 532 nm excitation, 100 ms exposure 25 sec, irradiance of 1.3 kW/cm^2. For the ND-EDC-NHS-DNA (*i.e.* Cy3-DNA-FND) sample, the combination of non-specific binding of Cy3-DNA-FNDs with the dissociation of Cy3-DNA-FNDs from the surface caused short increase of R/G ratio from 0.8 up to above 1, a negligible artifact. For more details on the method, see figure 3.3 on page 37.

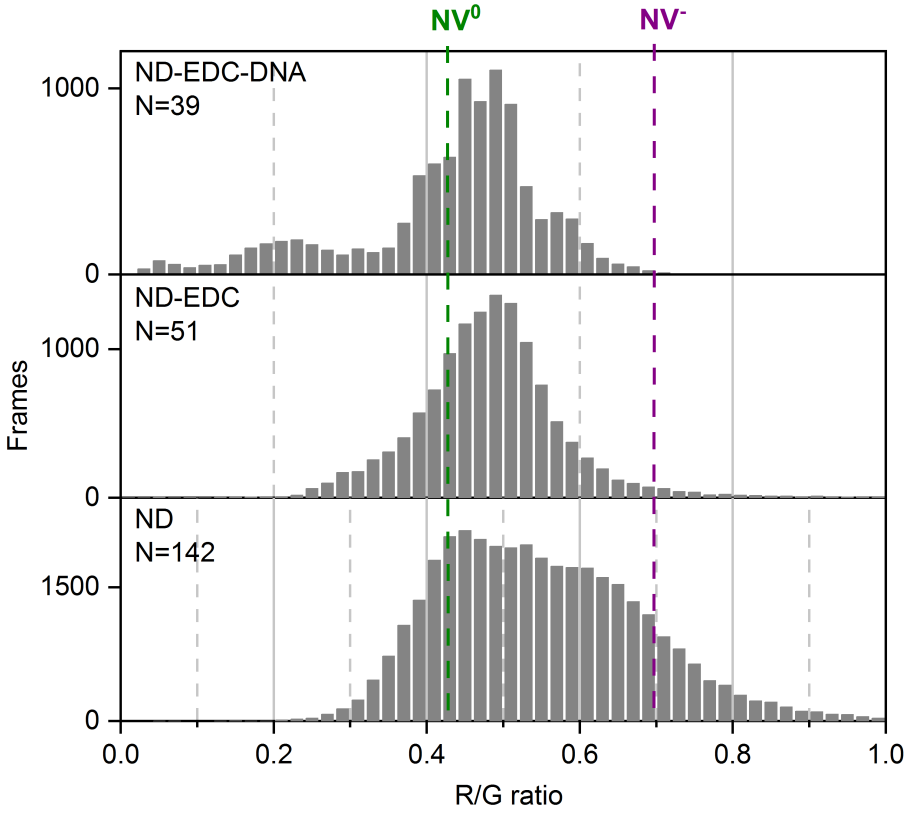

Figure 6.4: R/G ratio distribution of the NV centre in raw 10-nm FNDs and following bio-functionalisation (ND-EDC-DNA, *i.e.* Cy3-DNA-FND) or EDC treatment only (in air). 532 nm excitation, 100 ms exposure 25 sec, irradiance of 1.6 kW/cm^2. The small subpopulation at 0.2 for the ND-EDC-DNA sample is due to aggregated ND-EDC-DNA formed during the drying on the glass surface. The large amount of Cy3-DNA molecules in these aggregates did not bleach, even with higher laser irradiance. For more details on the method, see figure 3.3 on page 37.

6.4 Live-cell tracking of bio-conjugated nanodiamonds

With a view to using Cy3-DNA-FNDs for live-cell transcriptional studies, we electroporated Cy3-DNA-NDs into *E. coli*. The Cy3-DNA-NDs electroporation was done by adapting a protocol previously used to internalise DNA into *E. coli* [126]. Figure 6.5 shows an example of the fluorescence images obtained for cells electroporated with Cy3-DNA-NDs or with TE buffer only (negative control). The negative control shows that *E. coli* cells have some autofluorescence that appears mostly on the green channel (see bottom right image 6.5) with varying intensity: from low (see cell number 5) to high (see cell number 6). Cells electroporated with Cy3-DNA-NDs also have cell autofluorescence (see cell 3) but most cells contain green bright spots (see cells in position 2 and 4) with different levels of density and intensity; for instance, cell 4 contains only 2 spots while cells in position 2 have 3-4 spots per cell. Finally, some bacteria will not contain any spots and show low autofluorescence like cell 1. Since we did not observe the same bright spots in the negative control, we concluded that this signal is coming from the Cy3-DNA.

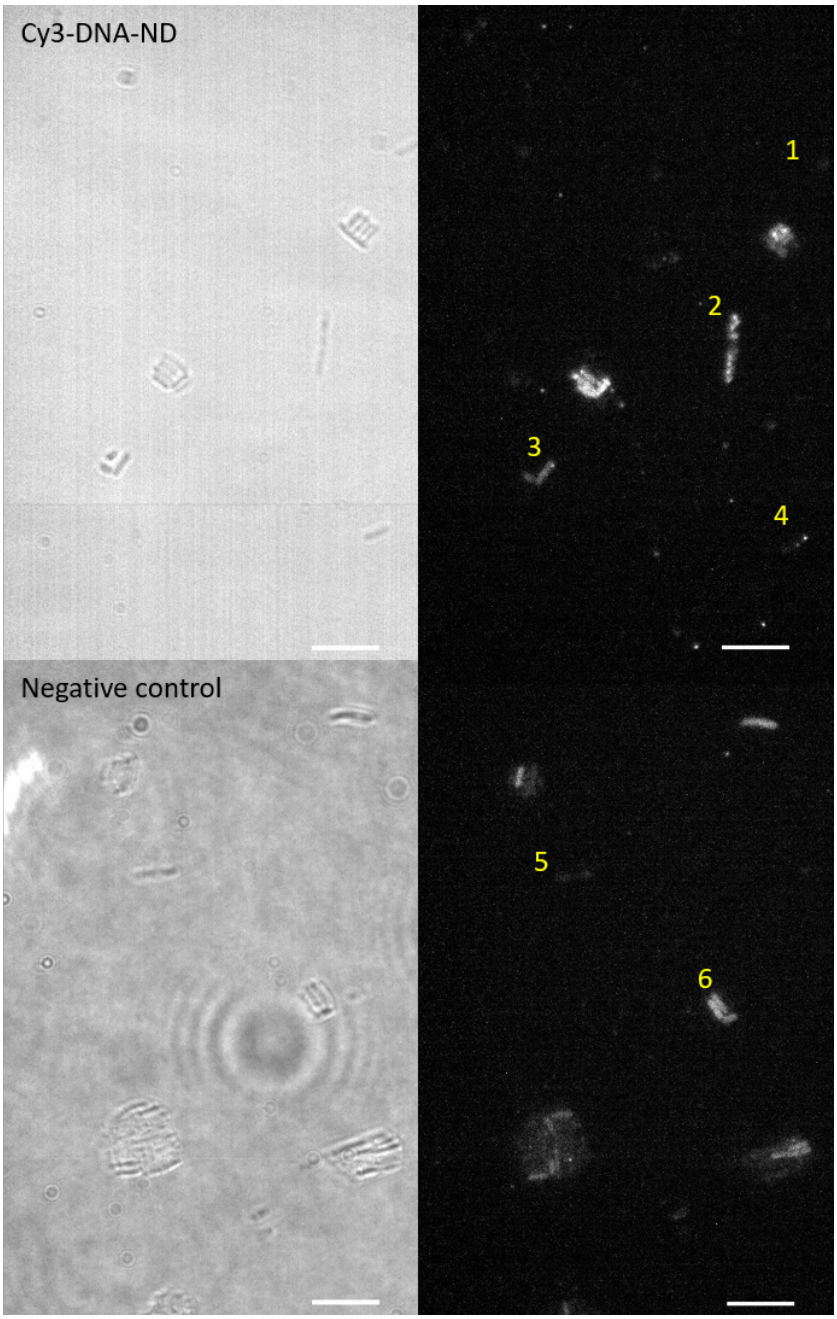

Figure 6.5: *E. coli* cells electroporated with Cy3-DNA-FNDs or TE buffer (negative control). The two pictures on the left are bright field recording showing the cell shape while pictures on the right are the first frames of a fluorescence recording from the green channel. Fluorescence movies were captured with 50 ms exposure for 30-60 sec and low 532 nm excitation (0.1 kW/cm^2) in order to image Cy3 fluorescence. Both Cy3-DNA-FNDs and the negative control images are shown with the same pixel value scaling (*i.e.* contrast and luminosity). Scale bar 8 μm.

When looking at the movies we could also notice that the Cy3-DNAs are diffusing inside the cell (see tracks in figure 6.6), thus concluding that the internalisation of Cy3-DNA or Cy3-DNA-NDs was successful. As discussed in the previous chapter (see discussion chapter 5 on page 85) Cy3-DNA also adsorbs to the NDs, which may cause the release of Cy3-DNA into the solution even after thorough purification because of changes in temperature, salts or Cy3-DNA-ND concentration. Therefore, we cannot exclude the fact that the Cy3 fluorescence captured inside the cells are from free Cy3-DNA.

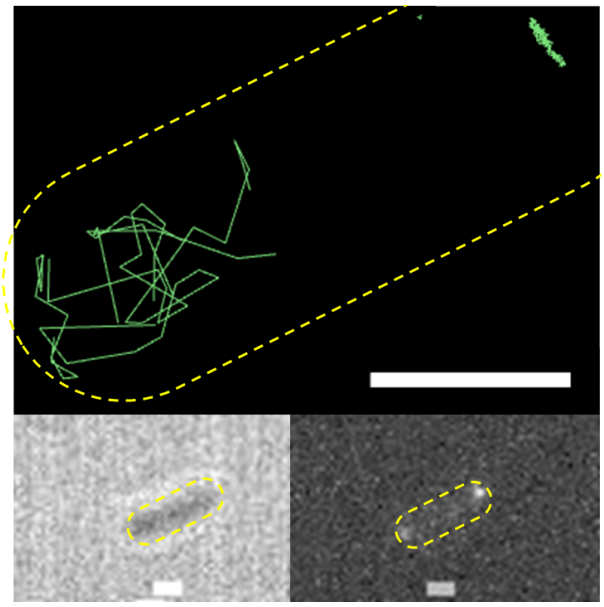

(a) Example 1

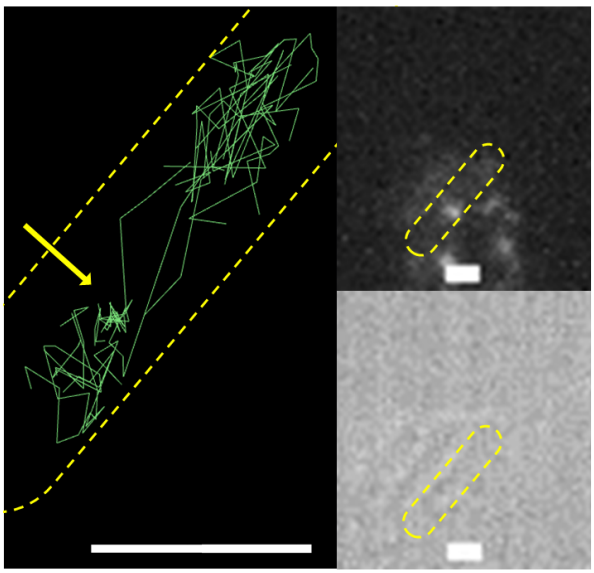

(b) Example 2

Figure 6.6: Example of intracellular tracks following the electroporation of Cy3-DNA-ND in *E. coli*. The tracks were found using a tracking software provided with the microscope. The bright field image is shown in one of the insets and the yellow dotted line is an approximation of the cell wall. The picture with the dark background is one frame of the fluorescence image showing one or two intracellular Cy3 spots. The tracks are shown in green in the larger inset. In example 2, the diffusing emitter is moving inside the cell but stops and stays relatively stationary at the place marked by a yellow arrow. Fluorescence movies were captured with 50 ms exposure for 30-60 sec and low 532 nm excitation (0.1 kW/cm^2) in order to image Cy3 fluorescence. Scale bar 1 μm.

In order to establish that the Cy3-DNA-NDs were internalised, we need to record NV fluorescence from inside the cell. Following low power excitation to track Cy3 fluorescence, cells were submitted to higher irradiance to not only photobleach Cy3 molecules and cell autofluorescence but also to image NV fluorescence. If Cy3-DNA-FNDs were successfully electroporated, we would expect that some cells might show low but photostable NV centre fluorescence in both green and red channel with a $\backsim$0.4 R/G ratio as measured in figure 6.3 on page 97. Two cells out of the 43 cells imaged (two fields of view) appear to have NV fluorescence (see example in figure 6.7). As expected, the fluorescence appears in both channels with an average pixel intensity (both channels) of 17 a.u. and an average R/G ratio of 0.42 (N=4 data points from 2 different cells). The fluorescence signal was not continuous during the recording but appeared stochastically (dark duration up to 30 sec) inside the cell in a similar localisation (up to 300 nm away from the previous spot). In one of the cells shown in figure 6.7 (example 2), the NV fluorescence occurs at the same region of the cell where Cy3 fluorescence is recorded as this cell incorporated 3-4 fluorescent particles, thus suggesting that one of the Cy3-DNA-NDs internalised had an NV centre that we could observe once the Cy3 has photobleached. The cell shown in figure 6.7 (example 1) did not show prior Cy3 fluorescence possibly because the FND was not functionalised (reaction efficiency up to 30% of the NDs) or due to the photobleaching of the Cy3 molecule within the first few seconds of imaging usually required to change field of view and refocus before recording.

To further confirm that this signal is different from cell autofluorescence we compared the pixel intensity and R/G ratio with the ones from the rare fluorescent spots appearing in both channels in the negative control. With an average pixel intensity (both channels) of 6 a.u. and a R/G ratio of 0.7 (N=2 data points), we deduced

that cell autofluorescence detected in both channels are due to dimer red fluorescent molecules that have photophysical properties distinct from the NV centre; moreover, the spots found in the negative control only appeared once in the cell suggesting that these emitters photobleached. It is also worth noting that neither Cy3 nor NV fluorescence was found in the control sample where we attempted to internalise Cy3-DNA-NDs or raw NDs using either electroporation or a 15-min incubation of bacteria with NDs as described by Wehling *et al.* ([74] data not shown).

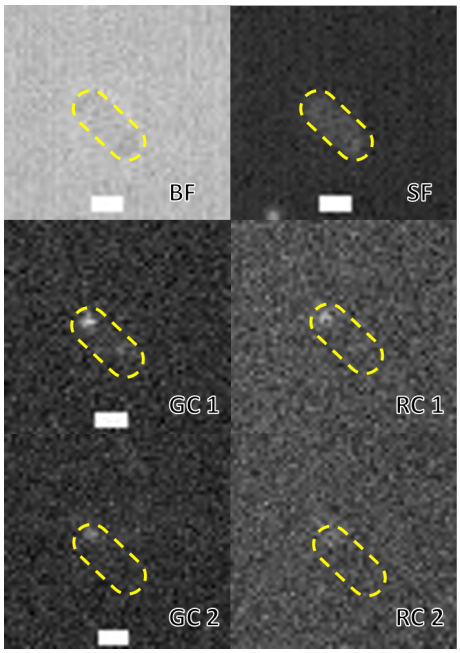

(a) Example 1

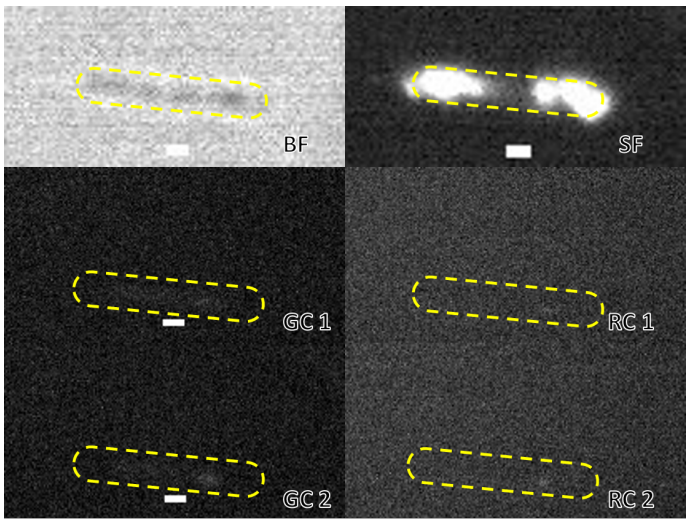

(b) Example 2

Figure 6.7: Example of intracellular NV fluorescence following electroporation of Cy3-DNA-NDs. BF: bright field; SF: sum of all the fluorescence frames (green channel, low power excitation to image Cy3); GC1: green channel first selected frame; RC1: red channel first selected frame; GC2: green channel second selected frame (up to 30 sec after the first frame selected); RC2: red channel second selected frame; The yellow dotted line is an approximation of the cell wall based on the bright field image. For the spots shown: average pixel intensity 17 a.u. (both channels); average R/G ratio of 0.42. All the pixel intensity values and R/G ratios are background corrected. Fluorescence movies were captured with 50 ms exposure for 30-60 sec, 532 nm excitation (0.1 kW/cm^{2}to image Cy3 and for the selected frames 1.3 kW/cm^{2}to image NV centre). Scale bar 1 μm.

6.5 Discussion

Being able to perform ODMR on a single biomolecule would be a great advancement for not only biology but also chemistry and physical chemistry as it would allow to study in real-time and for an indefinite amount of time conformation changes and molecular interactions without using any labels. To achieve such a challenging task, the use of NDs is preferable as they are optimal for *in vivo* measurement. Nonetheless, we found that the labelling protocol we developed is causing considerable charge instability on the 10-nm FNDs, thus preventing to perform ODMR measurements. Our findings are relevant for the diamond community as we were able to show that EDC is a compound responsible for the loss of the NV^- charge state; with EDC being used in many of the bioimaging/bio-sensing work previously reported (in bulk diamond and NDs) [39, 125, 128, 129].

The mechanism by which EDC is causing the loss of charge in the NV centre is still unclear, but we speculate that the positive charge of this molecule can interact with the negative charges of the NDs surface (*e.g.,* carboxylic acids). A likely scenario since EDC is very much in excess in the reaction mixture (10^6 EDC molecules for 1 ND, see materials and method in chapter 5 on page 86). Despite the fact that more experiments and possibly modelling is required to elucidate the mechanism of charge destabilisation, we showed that our method to study charge stability can be not only useful in the context of bioimaging and pH sensing (see chapter 3), but also for the characterisation of NDs for quantum sensing.

Our precise understanding of the photophysical properties of the NV centre in NDs also allowed us to confirm intracellular NV fluorescence in the complex context of *in*

vivo single-molecule microscopy. Following the electroporation of Cy3-DNA-FNDs, we were able to track Cy3 signal inside different *E. coli* cells and in some cases detect the characteristic NV fluorescence. This result suggests that we achieved the first internalisation and single-particle tracking of FNDs inside bacteria, although more cells and data points need to be collected. The NV fluorescence was found in 2 cells out of 47 cells (5%), a low number of observation due to the fact that not all the NDs contain an NV centre (1-0.03%, see section 3.2 on page 33 for more details). Additionally, since this is the first time that such small NDs are tracked inside such small cells we had to perform movie analysis manually as no software was able to detect NV fluorescence accurately. The limitation we had to analyse the recordings reduced our throughput, but it should be easy to collect more observations. Now that we have established how the NV centre behaves inside the cell (low and intermittent fluorescence), we can just image more cells and adjust the parameters of our localisation/tracking algorithm to observe more events.

The intermittence of the NV centre inside the cell is most likely due to a change in the diffusion coefficient inside the cell. We could exclude photoblinking because the 10-nm FNDs do not show blinking, as demonstrated in chapter 3 (see section 3.2 on page 33 for more details). Furthermore, we performed a control experiment to measure the NV fluorescence from 10-nm NDs immersed inside bacterial cell lysate and did not observe blinking (data not shown). In one of the cells, the NV signal is up to 300 nm away from the previous spot, which also corroborates our hypothesis that the FNDs are diffusing too fast to be imaged but can be only observed when the FNDs become stationary for an instant. An example of such behaviour was observed when tracking Cy3 signal inside the cell (see example 2 in figure 6.6 on page 102). The interruption of the FND diffusion might be due to unspecific interaction with the large DNA bacterial chromosome as it is the largest molecule inside the bacteria. Nonetheless, a specific

interaction cannot be excluded since the FND always reappears in a similar region of the cell. It is possible that the FNDs encountered a slow diffusing RNAP cluster (previously described by our lab [13]) where the short gene, present in the Cy3-DNA attached to the FND, is transcribed multiple times by the clustered RNAPs. With more data points, this hypothesis could be confirmed by looking at the tracks formed by the Cy3 fluorescence and investigate the changes in intensity and diffusion coefficient.

The latter conjecture illustrates the fact that even if the fast FNDs could not be tracked with NV fluorescence, there is still many interesting investigations that can be made by just studying the NV signal from stationary FNDs interacting with large bio-molecular clusters or the bacterial chromosome.

Lastly, the fact that we could not internalise raw NDs by electroporation or incubation reveals important limitations of two previous publications of ND imaging in yeast and bacteria. First, internalisation of raw NDs with electroporation is not possible or very inefficient, even if this has been achieved in *S. cerevisiae* [71]. *E. coli* and *S. cerevisiae* are two very different microorganisms; unlike *E. coli*, *S. cerevisiae* is a eukaryote organism that has a different membrane structure and composition. It is more likely that NDs can more easily cross the membrane of *S. cerevisiae* as it is able to perform endocytosis, a process whereby the membrane invaginates to internalise external material. Second, internalisation of raw HPHT NDs inside bacteria by incubation is inefficient or impossible as we could not reproduce the works by Wehling *et al.*. The authors were able to internalise detonation NDs in *E. coli* by incubating the detonation NDs with bacteria for 15 minutes [74]. The possible explanation of this result discrepancy between us and Wehling *et al.* is the type of ND used: detonation NDs and HPHT NDs (*i.e.* the 10-nm NDs) have different surface chemistry. Indeed, detonation NDs usually have more sp^2 carbon on their surface, which might lead to different types of electrostatic interactions between the NDs and the cell membrane [100, 116]. Moreover,

the successful electroporation of functionalised NDs suggests that DNA or EDC have a positive impact on the internalisation efficiency. We hypothesise that DNA is responsible for the increased efficiency as previous reports showed efficient electroporation of DNA inside *E. coli* cells [130, 126].

6.6 Material and methods

ODMR

The Cy3-DNA-ND were prepared as described in chapter 5 (see materials and methods 5.5 on page 86) and spin coated on a borosilicate microscope slide (10-20 µL with a concentration estimated to 100 nM). Silicone gaskets were used to form wells and after the addition of the imaging buffer (see composition in the section 5.5 on page 86) the well was sealed with another slide on the top. A wire passing on the slide were the NDs are immobilised was soldered to the chip to deliver the microwave. Shazeea Ishmael used a custom-built confocal set-up to perform ODMR measurement as Jason Smith's lab previously described [131].

Electroporation

ElectroMAX DH5α-E Competent Cells (Invitrogen) were used for electroporation. For the electroporation 20µL of electrocompetent cells were mixed with one of the following reagents: 9.4 picomoles of Cy3-DNA-ND, 117 picomoles of 10-nm NDs (adamas nano), 1 picomoles of 10-nm NDs, 10 µL of TE buffer (volume max 30 µL, see composition in the section 3.6 on page 49) and incubated 1-3 minutes on ice. The mixture of electrocompetent was placed into an electroporator (MicroPulser, Bio-Rad) and an electric field of 1.4 kV was applied for electroporation with a measured time constant

between 3 and 10 ms. A non-electroporated control was also prepared for the Cy3-DNA-NDs and 10-nm ND sample where the cells incubated at 37°C for 15 min. 500µL of super optimal broth with catabolite repression (SOC, Invitrogen) medium was added immediately after electroporation. Cells were recovered for 20-30 minutes at 37°C under stirring. After recovery, cells were washed with PBS buffer using 3 rounds of centrifugation at 3300g for 1min at 4°C. Cells were then resuspended in 80-150 µL of PBS and placed on 1% agarose pads containing M9 medium. 5µL of cells were pipetted onto the pad and imaged subsequently.

Imaging and data analysis

Imaging was done using a more recent NanoimagerS than in chapter 3 (from ONI, see section 3.6 on page 49 for more details) and the tracking of intracellular emitters was done using the build-in software. The tracking parameters were 1-2 maximum gap between each frame, 1 µm as a maximum distance between frames, 1.5 µm exclusion radius, and a minimum of 4 steps for each tracks. Pixel intensity and R/G ratio measurement were done manually on the raw movies using an image processing software (Fiji) and analysing a 9x9 pixel area centred on the fluorescent spot. The background value was taken on the same location as the fluorescent spot, but 1-3 frames before the appearance of the spot in order to take autofluorescence into account.

Chapter 7

Conclusion

The work detailed in this thesis should help the bioimaging community to implement FNDs. Our first contribution was to develop a characterisation method to analyse the heterogeneity of the ND's photophysical behaviour, a methodology that we extended to diffusing NDs. Such sensitive and quick characterisation method will not only benefit the bioimaging community but also anyone working on application of FNDs as photon sources or as versatile quantum sensors (*e.g.,* magnetometer, thermometer etc.).

Using our high-throughput characterisation capabilities, we learned more about what is causing NV centre's charge state transitions in NDs and their dynamics, a knowledge that has been mainly extrapolated from in bulk studies until now. More precisely, we discovered that the charge state of the NV centre inside 10-nm FNDs responds to pH variations, thus rendering FNDs even more promising bioimaging probes since they could be used as pH nanosensors for microfluidics or intracellular pH mapping. We also investigated the lifetimes of the NV centre's charge states in NDs, an important and yet unexplored property of this crystal defect. For instance, stochastic charge state transitions inside FNDs have been recently used to perform super-resolution microscopy *in vivo* [132]. Finally, we uncovered the detrimental effect of EDC-mediated function-

alisation on the charge stability, thus rendering quantum sensing more problematic to implement on small bio-functionalised FNDs (10-nm). Such a finding will be useful regarding any implementations of diamond (bulk or nanoparticle) for single-molecule quantum metrology, a new application of the NV centre having the potential to greatly impact biochemistry.

Our work on diffusing NDs should allow material scientists to analyse simultaneously the size and the photophysics of FNDs. Furthermore, we detailed a method to estimate the proportion of FNDs in a ND sample that is simpler than the combination of AFM and confocal microscope usually used.

We took advantage of the simultaneous measurement of size and fluorescence properties (*i.e.* intensity and R/G ratio) to take an innovative approach to the bio-functionalisation of NDs. By measuring the FND's colloidal stability, we were able to find appropriate buffers for the coupling reaction and simplify our protocol to make the smallest functionalised FNDs ever manufactured as demonstrated by single-particle tracking using their Cy3-fluorescence. The FND-DNA conjugates maintained biological activity as shown by our ensemble and single-molecule data; we hereby performed *in vivo* single-particle tracking experiments in bacteria (*E. coli*).

In the last chapter we presented the first single-particle observations of FNDs inside bacteria for long term single-molecule experiments. Indeed, *in vivo* single-molecule studies have been typically limited to a few seconds because of photobleaching; FNDs now offer the possibility to study single molecules in live bacteria for at least several minutes (and potentially much longer) provided that phototoxicity is carefully managed. We also showed that FND electroporation is most likely enhanced by DNA, a molecule known to be easily internalised by electric shocks. Such a unique way of internalisation can be used to internalise not only different DNA sequences but also proteins for a wide range of single-molecule experiments. Furthermore, the DNA mediated in-

ternalisation of NDs can also be used as a delivery system for bacterial transformation or the intracellular release of antibiotics.

Nonetheless, two questions should be addressed so that long-term FND *in vivo* single-molecule imaging can be carried out without much disturbance of the cell's biology. First, a better control of the ND's surface would permit us to stabilise the negative charge state for ODMR measurements; additionally, it would allow us to limit non-specific ND-DNA interactions, thus simplifying the interpretation of single-molecule data. A possible solution is to passivate the surface with more negatively charged groups (*e.g.,* very extensive oxygen termination) or a very shallow negatively charged polymer coating. Second, the electroporation of the FND-DNA conjugates needs to be repeated with a greater number of observations to have a better idea of the incorporation efficiency, cell viability and the photophysical behaviour of 10-nm FNDs inside bacteria cells. More repeats should be easier to collect now that the electroporation protocol and routine analysis have been established. Third, the phototoxicity caused by the higher irradiance needed to image 10-nm FNDs must be taken into consideration, especially when the aim is to perform long single-molecule tracking. To manage the photodamage one may use longer exposure time or implement background-free imaging techniques that exploit the spin-dependant fluorescence of the NV centre [42, 43, 58].

The future of FNDs in bioimaging will be most likely a combination of single-molecule tracking and nanosensing, which harnesses either the NV centre's charge state sensitivity to the nano-environment (*e.g.,* pH or temperature) or the spin-dependant fluorescence for nano-magnetometry. To do so, progress in material science to manufacture smaller and brighter FNDs with fewer impurities would be of great use for the bioimaging community. Moreover, diamond technology is already functional for many biological investigations (*e.g.,* single molecule tracking and quantum sensing) and communication about the potential of such technology to biologists is very im-

portant as their usage of FNDs will encourage diamond scientists towards achieving high-performance long duration FND multimodal imaging.

Bibliography

[1] R. Saiki, S. Scharf, F. Faloona, K. Mullis, G. Horn, H. Erlich, and N. Arnheim, "Enzymatic amplification of beta-globin genomic sequences and restriction site analysis for diagnosis of sickle cell anemia," *Science*, vol. 230, no. 4732, pp. 1350–1354, 1985.

[2] G. Binnig, C. F. Quate, and C. Gerber, "Atomic force microscope," *Phys. Rev. Lett.*, vol. 56, pp. 930–933, Mar 1986.

[3] D. J. Billingsley, W. A. Bonass, N. Crampton, J. Kirkham, and N. H. Thomson, "Single-molecule studies of dna transcription using atomic force microscopy," *Physical biology*, vol. 9, no. 2, p. 021001, 2012.

[4] J. Dubochet and A. McDowall, "Vitrification of pure water for electron microscopy," *Journal of Microscopy*, vol. 124, no. 3, pp. 3–4, 1981.

[5] J. Frank, J. Zhu, P. Penczek, Y. Li, S. Srivastava, A. Verschoor, M. Radermacher, R. Grassucci, R. K. Lata, and R. K. Agrawal, "A model of protein synthesis based on cryo-electron microscopy of the e. coli ribosome," *Nature*, vol. 376, no. 6539, pp. 441–444, 1995.

[6] P. N. T. Unwin and R. Henderson, "Molecular structure determination by electron microscopy of unstained crystalline specimens," *Journal of molecular biology*, vol. 94, no. 3, pp. 425–440, 1975.

[7] E. Neher and B. Sakmann, "Single-channel currents recorded from membrane of denervated frog muscle fibres," *Nature*, vol. 260, no. 5554, p. 799, 1976.

[8] S. M. Block, L. S. Goldstein, and B. J. Schnapp, "Bead movement by single kinesin molecules studied with optical tweezers," *Nature*, vol. 348, no. 6299, p. 348, 1990.

[9] W. E. Moerner and L. Kador, "Optical detection and spectroscopy of single molecules in a solid," *Physical review letters*, vol. 62, no. 21, p. 2535, 1989.

[10] M. Orrit and J. Bernard, "Single pentacene molecules detected by fluorescence excitation in a p-terphenyl crystal," *Physical review letters*, vol. 65, no. 21, p. 2716, 1990.

[11] Z. Liu, L. D. Lavis, and E. Betzig, "Imaging live-cell dynamics and structure at the single-molecule level," *Molecular cell*, vol. 58, no. 4, pp. 644–659, 2015.

[12] T. Xia, N. Li, and X. Fang, "Single-molecule fluorescence imaging in living cells," *Annual Review of Physical Chemistry*, vol. 64, no. 1, pp. 459–480, 2013. PMID: 23331306.

[13] M. Stracy, C. Lesterlin, F. G. de Leon, S. Uphoff, P. Zawadzki, and A. N. Kapanidis, "Live-cell superresolution microscopy reveals the organization of rna polymerase in the bacterial nucleoid," *Proceedings of the National Academy of Sciences*, vol. 112, no. 32, pp. E4390–E4399, 2015.

[14] S. Uphoff, R. Reyes-Lamothe, F. Garza de Leon, D. J. Sherratt, and A. N. Kapanidis, "Single-molecule dna repair in live bacteria," *Proceedings of the National Academy of Sciences*, vol. 110, no. 20, pp. 8063–8068, 2013.

[15] A. Van Oijen, J. Köhler, J. Schmidt, M. Müller, and G. Brakenhoff, "3-dimensional super-resolution by spectrally selective imaging," *Chemical Physics Letters*, vol. 292, no. 1, pp. 183–187, 1998.

[16] E. Betzig, G. H. Patterson, R. Sougrat, O. W. Lindwasser, S. Olenych, J. S. Bonifacino, M. W. Davidson, J. Lippincott-Schwartz, and H. F. Hess, "Imaging intracellular fluorescent proteins at nanometer resolution," *Science*, vol. 313, no. 5793, pp. 1642–1645, 2006.

[17] M. J. Rust, M. Bates, and X. Zhuang, "Sub-diffraction-limit imaging by stochastic optical reconstruction microscopy (storm)," *Nature methods*, vol. 3, no. 10, pp. 793–796, 2006.

[18] M. Dahan, S. Lévi, C. Luccardini, P. Rostaing, B. Riveau, and A. Triller, "Diffusion dynamics of glycine receptors revealed by single-quantum dot tracking," *Science*, vol. 302, no. 5644, pp. 442–445, 2003.

[19] M. M. Barroso, "Quantum dots in cell biology," *Journal of Histochemistry & Cytochemistry*, vol. 59, no. 3, pp. 237–251, 2011.

[20] B. Mahler, P. Spinicelli, S. Buil, X. Quelin, J.-P. Hermier, and B. Dubertret, "Towards non-blinking colloidal quantum dots," *Nature materials*, vol. 7, no. 8, p. 659, 2008.

[21] C.-C. Fu, H.-Y. Lee, K. Chen, T.-S. Lim, H.-Y. Wu, P.-K. Lin, P.-K. Wei, P.-H. Tsao, H.-C. Chang, and W. Fann, "Characterization and application of single fluorescent nanodiamonds as cellular biomarkers," *Proceedings of the National Academy of Sciences*, vol. 104, no. 3, pp. 727–732, 2007.

[22] A. Krueger, "New carbon materials: biological applications of functionalized nanodiamond materials," *Chemistry–A European Journal*, vol. 14, no. 5, pp. 1382–1390, 2008.

[23] M. Chipaux, K. J. van der Laan, S. R. Hemelaar, M. Hasani, T. Zheng, and R. Schirhagl, "Nanodiamonds and their applications in cells," *Small*, vol. 14, no. 24, p. 1704263, 2018.

[24] L. Rondin, J. Tetienne, T. Hingant, J. Roch, P. Maletinsky, and V. Jacques, "Magnetometry with nitrogen-vacancy defects in diamond," *Reports on Progress in Physics*, vol. 77, no. 5, p. 056503, 2014.

[25] G. Balasubramanian, I. Chan, R. Kolesov, M. Al-Hmoud, J. Tisler, C. Shin, C. Kim, A. Wojcik, P. R. Hemmer, A. Krueger, *et al.*, "Nanoscale imaging magnetometry with diamond spins under ambient conditions," *Nature*, vol. 455, no. 7213, p. 648, 2008.

[26] J. Maze, P. Stanwix, J. Hodges, S. Hong, J. Taylor, P. Cappellaro, L. Jiang, M. G. Dutt, E. Togan, A. Zibrov, *et al.*, "Nanoscale magnetic sensing with an individual electronic spin in diamond," *Nature*, vol. 455, no. 7213, p. 644, 2008.

[27] C. Singer, "Notes on the early history of microscopy," *Proceedings of the Royal Society of Medicine*, vol. 7, no. Sect_Hist_Med, pp. 247–279, 1914.

[28] M. H. Horrocks, M. Palayret, D. Klenerman, and S. F. Lee, "The changing point-spread function: single-molecule-based super-resolution imaging," *Histochemistry and cell biology*, vol. 141, no. 6, pp. 577–585, 2014.

[29] S. W. Hell and J. Wichmann, "Breaking the diffraction resolution limit by stimulated emission: stimulated-emission-depletion fluorescence microscopy," *Optics letters*, vol. 19, no. 11, pp. 780–782, 1994.

[30] X. Zhuang, L. E. Bartley, H. P. Babcock, R. Russell, T. Ha, D. Herschlag, and S. Chu, "A single-molecule study of rna catalysis and folding," *Science*, vol. 288, no. 5473, pp. 2048–2051, 2000.

[31] R. Crawford, J. P. Torella, L. Aigrain, A. Plochowietz, K. Gryte, S. Uphoff, and A. N. Kapanidis, "Long-lived intracellular single-molecule fluorescence using electroporated molecules," *Biophysical journal*, vol. 105, no. 11, pp. 2439–2450, 2013.

[32] J. J. Sakon and K. R. Weninger, "Detecting the conformation of individual proteins in live cells," *Nature methods*, vol. 7, no. 3, p. 203, 2010.

[33] B. Rieger and S. Stallinga, "The lateral and axial localization uncertainty in super-resolution light microscopy," *ChemPhysChem*, vol. 15, no. 4, pp. 664–670, 2014.

[34] D. Duchi, D. Bauer, L. Fernandez, G. Evans, N. Robb, L. Hwang, K. Gryte, A. Tomescu, P. Zawadzki, Z. Morichaud, K. Brodolin, and A. Kapanidis, "Rna polymerase pausing during initial transcription," *Molecular Cell*, vol. 63, no. 6, pp. 939 – 950, 2016.

[35] R. Jungmann, M. S. Avendaño, J. B. Woehrstein, M. Dai, W. M. Shih, and P. Yin, "Multiplexed 3d cellular super-resolution imaging with dna-paint and exchange-paint," *Nature methods*, vol. 11, no. 3, p. 313, 2014.

[36] W. Ye, M. Gotz, S. Celiksoy, L. Tuting, C. Ratzke, J. Prasad, J. Ricken, S. V. Wegner, R. Ahijado-Guzman, T. Hugel, *et al.*, "Conformational dynamics of a single protein monitored for 24 h at video rate," *Nano letters*, vol. 18, no. 10, pp. 6633–6637, 2018.

[37] D. Jin, P. Xi, B. Wang, L. Zhang, J. Enderlein, and A. M. van Oijen, "Nanoparticles for super-resolution microscopy and single-molecule tracking," *Nature methods*, p. 1, 2018.

[38] I. I. Vlasov, A. S. Barnard, V. G. Ralchenko, O. I. Lebedev, M. V. Kanzyuba, A. V. Saveliev, V. I. Konov, and E. Goovaerts, "Nanodiamond photoemitters based on strong narrow-band luminescence from silicon-vacancy defects," *Advanced Materials*, vol. 21, no. 7, pp. 808–812, 2009.

[39] W. Liu, F. Yu, J. Yang, B. Xiang, P. Xiao, and L. Wang, "3d single-molecule imaging of transmembrane signaling by targeting nanodiamonds," *Advanced Functional Materials*, vol. 26, no. 3, pp. 365–375, 2016.

[40] A. Bumb, S. K. Sarkar, N. Billington, M. W. Brechbiel, and K. C. Neuman, "Silica encapsulation of fluorescent nanodiamonds for colloidal stability and facile surface functionalization," *Journal of the American Chemical Society*, vol. 135, no. 21, pp. 7815–7818, 2013. PMID: 23581827.

[41] Y. Wu, A. Ermakova, W. Liu, G. Pramanik, T. M. Vu, A. Kurz, L. McGuinness, B. Naydenov, S. Hafner, R. Reuter, J. Wrachtrup, J. Isoya, C. FÃ¶rtsch, H. Barth, T. Simmet, F. Jelezko, and T. Weil, "Programmable biopolymers for advancing biomedical applications of fluorescent nanodiamonds," *Advanced Functional Materials*, vol. 25, no. 42, pp. 6576–6585, 2015.

[42] R. Igarashi, Y. Yoshinari, H. Yokota, T. Sugi, F. Sugihara, K. Ikeda, H. Sumiya, S. Tsuji, I. Mori, H. Tochio, Y. Harada, and M. Shirakawa, "Real-time background-free selective imaging of fluorescent nanodiamonds in vivo," *Nano Letters*, vol. 12, no. 11, pp. 5726–5732, 2012. PMID: 23066639.

[43] S. K. Sarkar, A. Bumb, X. Wu, K. A. Sochacki, P. Kellman, M. W. Brechbiel, and K. C. Neuman, "Wide-field in vivo background free imaging by selective magnetic modulation of nanodiamond fluorescence," *Biomedical optics express*, vol. 5, no. 4, pp. 1190–1202, 2014.

[44] O. Faklaris, *Photoluminescent diamond nanoparticles as labels in cells: study of their optical properties and investigation of their cellular uptake mechanism*. PhD thesis, École normale supérieure de Cachan-ENS Cachan, 2009.

[45] T. Plakhotnik and H. Aman, "Nv-centers in nanodiamonds: How good they are," *Diamond and Related Materials*, vol. 82, pp. 87 – 95, 2018.

[46] Y.-K. Tzeng, O. Faklaris, B.-M. Chang, Y. Kuo, J.-H. Hsu, and H.-C. Chang, "Superresolution imaging of albumin-conjugated fluorescent nanodiamonds in cells by stimulated emission depletion," *Angewandte Chemie International Edition*, vol. 50, no. 10, pp. 2262–2265, 2011.

[47] M. Barbiero, S. Castelletto, X. Gan, and M. Gu, "Spin-manipulated nanoscopy for single nitrogen-vacancy center localizations in nanodiamonds," *Light: Science & Applications*, vol. 6, no. 11, p. e17085, 2017.

[48] U. Resch-Genger, M. Grabolle, S. Cavaliere-Jaricot, R. Nitschke, and T. Nann, "Quantum dots versus organic dyes as fluorescent labels," *Nature methods*, vol. 5, no. 9, pp. 763–775, 2008.

[49] M. W. Doherty, N. B. Manson, P. Delaney, F. Jelezko, J. Wrachtrup, and L. C. Hollenberg, "The nitrogen-vacancy colour centre in diamond," *Physics Reports*, vol. 528, no. 1, pp. 1–45, 2013.

[50] J. Tisler, G. Balasubramanian, B. Naydenov, R. Kolesov, B. Grotz, R. Reuter, J.-P. Boudou, P. A. Curmi, M. Sennour, A. Thorel, *et al.*, "Fluorescence and

spin properties of defects in single digit nanodiamonds," *ACS nano*, vol. 3, no. 7, pp. 1959–1965, 2009.

[51] B. R. Smith, D. W. Inglis, B. Sandnes, J. R. Rabeau, A. V. Zvyagin, D. Gruber, C. J. Noble, R. Vogel, E. Ōsawa, and T. Plakhotnik, "Five-nanometer diamond with luminescent nitrogen-vacancy defect centers," *Small*, vol. 5, no. 14, pp. 1649–1653, 2009.

[52] T.-L. Wee, Y.-K. Tzeng, C.-C. Han, H.-C. Chang, W. Fann, J.-H. Hsu, K.-M. Chen, and Y.-C. Yu, "Two-photon excited fluorescence of nitrogen-vacancy centers in proton-irradiated type ib diamond," *The Journal of Physical Chemistry A*, vol. 111, no. 38, pp. 9379–9386, 2007.

[53] R. Schirhagl, K. Chang, M. Loretz, and C. L. Degen, "Nitrogen-vacancy centers in diamond: nanoscale sensors for physics and biology," *Annual review of physical chemistry*, vol. 65, pp. 83–105, 2014.

[54] A. M. Zaitsev, *Optical Properties of Diamond*. Springer-Verlag Berlin Heidelberg, 2001.

[55] G. Davies, M. F. Hamer, and W. C. Price, "Optical studies of the 1.945 ev vibronic band in diamond," *Proceedings of the Royal Society of London. A. Mathematical and Physical Sciences*, vol. 348, no. 1653, pp. 285–298, 1976.

[56] M. S. Barson, E. Krausz, N. B. Manson, and M. W. Doherty, "The fine structure of the neutral nitrogen-vacancy center in diamond," *Nanophotonics*, vol. 8, no. 11, pp. 1985–1991, 2019.

[57] K. Beha, A. Batalov, N. B. Manson, R. Bratschitsch, and A. Leitenstorfer, "Optimum photoluminescence excitation and recharging cycle of single nitrogen-

vacancy centers in ultrapure diamond," *Phys. Rev. Lett.*, vol. 109, p. 097404, Aug 2012.

[58] D. A. Simpson, E. Morrisroe, J. M. McCoey, A. H. Lombard, D. C. Mendis, F. Treussart, L. T. Hall, S. Petrou, and L. C. L. Hollenberg, "Non-neurotoxic nanodiamond probes for intraneuronal temperature mapping," *ACS Nano*, vol. 11, no. 12, pp. 12077–12086, 2017. PMID: 29111670.

[59] A. Gruber, A. Dräbenstedt, C. Tietz, L. Fleury, J. Wrachtrup, and C. Von Borczyskowski, "Scanning confocal optical microscopy and magnetic resonance on single defect centers," *Science*, vol. 276, no. 5321, pp. 2012–2014, 1997.

[60] S.-J. Yu, M.-W. Kang, H.-C. Chang, K.-M. Chen, and Y.-C. Yu, "Bright fluorescent nanodiamonds: No photobleaching and low cytotoxicity," *Journal of the American Chemical Society*, vol. 127, no. 50, pp. 17604–17605, 2005. PMID: 16351080.

[61] F. Bundy, H. Hall, H. Strong, and R. Wentorf, "Man-made diamonds," *Nature*, vol. 176, no. 4471, pp. 51–55, 1955.

[62] J.-P. Boudou, P. A. Curmi, F. Jelezko, J. Wrachtrup, P. Aubert, M. Sennour, G. Balasubramanian, R. Reuter, A. Thorel, and E. Gaffet, "High yield fabrication of fluorescent nanodiamonds," *Nanotechnology*, vol. 20, no. 23, p. 235602, 2009.

[63] J.-P. Boudou, J. Tisler, R. Reuter, A. Thorel, P. A. Curmi, F. Jelezko, and J. Wrachtrup, "Fluorescent nanodiamonds derived from hpht with a size of less than 10nm," *Diamond and Related Materials*, vol. 37, pp. 80–86, 2013.

[64] V. V. Danilenko, "On the history of the discovery of nanodiamond synthesis," *Physics of the Solid State*, vol. 46, pp. 595–599, Apr 2004.

[65] V. N. Mochalin, O. Shenderova, D. Ho, and Y. Gogotsi, "The properties and applications of nanodiamonds," *Nature Nanotechnology*, vol. 7, no. 1, pp. 11–23, 2012.

[66] C. Bradac, T. Gaebel, N. Naidoo, M. Sellars, J. Twamley, L. Brown, A. Barnard, T. Plakhotnik, A. Zvyagin, and J. Rabeau, "Observation and control of blinking nitrogen-vacancy centres in discrete nanodiamonds," *Nature Nanotechnology*, vol. 5, no. 5, pp. 345–349, 2010.

[67] C. Bradac, T. Gaebel, C. I. Pakes, J. M. Say, A. V. Zvyagin, and J. R. Rabeau, "Effect of the nanodiamond host on a nitrogen-vacancy color-centre emission state," *Small*, vol. 9, no. 1, pp. 132–139, 2013.

[68] J. C. Angus, H. A. Will, and W. S. Stanko, "Growth of diamond seed crystals by vapor deposition," *Journal of Applied Physics*, vol. 39, no. 6, pp. 2915–2922, 1968.

[69] M. Pfender, N. Aslam, G. Waldherr, P. Neumann, and J. Wrachtrup, "Single-spin stochastic optical reconstruction microscopy," *Proceedings of the National Academy of Sciences*, vol. 111, no. 41, pp. 14669–14674, 2014.

[70] J.-I. Chao, E. Perevedentseva, P.-H. Chung, K.-K. Liu, C.-Y. Cheng, C.-C. Chang, and C.-L. Cheng, "Nanometer-sized diamond particle as a probe for biolabeling," *Biophysical journal*, vol. 93, no. 6, pp. 2199–2208, 2007.

[71] S. R. Hemelaar, K. J. van der Laan, S. R. Hinterding, M. V. Koot, E. Ellermann, F. P. Perona-Martinez, D. Roig, S. Hommelet, D. Novarina, H. Takahashi, *et al.*, "Generally applicable transformation protocols for fluorescent nanodiamond internalization into cells," *Scientific reports*, vol. 7, no. 1, p. 5862, 2017.

[72] F.-J. Hsieh, S. Sotoma, H.-H. Lin, C.-Y. Cheng, T.-Y. Yu, C.-L. Hsieh, C.-H. Lin, and H.-C. Chang, "Bioorthogonal fluorescent nanodiamonds for continuous long-term imaging and tracking of membrane proteins," *ACS Applied Materials & Interfaces*, vol. 11, no. 22, pp. 19774–19781, 2019.

[73] T.-J. Wu, Y.-K. Tzeng, W.-W. Chang, C.-A. Cheng, Y. Kuo, C.-H. Chien, H.-C. Chang, and J. Yu, "Tracking the engraftment and regenerative capabilities of transplanted lung stem cells using fluorescent nanodiamonds," *Nature nanotechnology*, vol. 8, no. 9, p. 682, 2013.

[74] J. Wehling, R. Dringen, R. N. Zare, M. Maas, and K. Rezwan, "Bactericidal activity of partially oxidized nanodiamonds," *ACS nano*, vol. 8, no. 6, pp. 6475–6483, 2014.

[75] J. Mytych, A. Lewinska, J. Zebrowski, and M. Wnuk, "Nanodiamond-induced increase in ros and rns levels activates nf-Î¹b and augments thiol pools in human hepatocytes," *Diamond and Related Materials*, vol. 55, pp. 95 – 101, 2015.

[76] B. Woodhams, L. Ansel-Bollepalli, J. Surmacki, H. Knowles, L. Maggini, M. de Volder, M. AtatÃŒre, and S. Bohndiek, "Graphitic and oxidised high pressure high temperature (hpht) nanodiamonds induce differential biological responses in breast cancer cell lines," *Nanoscale*, vol. 10, pp. 12169–12179, 2018.

[77] H. P. Erickson, "Size and shape of protein molecules at the nanometer level determined by sedimentation, gel filtration, and electron microscopy," *Biological procedures online*, vol. 11, no. 1, p. 32, 2009.

[78] R. Teeling-Smith, Y. W. Jung, N. Scozzaro, J. Cardellino, I. Rampersaud, J. North, M. Å imon, V. Bhallamudi, A. Rampersaud, E. Johnston-Halperin,

M. Poirier, and P. Hammel, "Electron paramagnetic resonance of a single nv nanodiamond attached to an individual biomolecule," *Biophysical Journal*, vol. 110, no. 9, pp. 2044 – 2052, 2016.

[79] C. P. Epperla, N. Mohan, C.-W. Chang, C.-C. Chen, and H.-C. Chang, "Nanodiamond-mediated intercellular transport of proteins through membrane tunneling nanotubes," *Small*, vol. 11, no. 45, pp. 6097–6105, 2015.

[80] B.-M. Chang, H.-H. Lin, L.-J. Su, W.-D. Lin, R.-J. Lin, Y.-K. Tzeng, R. T. Lee, Y. C. Lee, A. L. Yu, and H.-C. Chang, "Highly fluorescent nanodiamonds protein-functionalized for cell labeling and targeting," *Advanced Functional Materials*, vol. 23, no. 46, pp. 5737–5745, 2013.

[81] S. Kaufmann, D. A. Simpson, L. T. Hall, V. Perunicic, P. Senn, S. Steinert, L. P. McGuinness, B. C. Johnson, T. Ohshima, F. Caruso, J. Wrachtrup, R. E. Scholten, P. Mulvaney, and L. Hollenberg, "Detection of atomic spin labels in a lipid bilayer using a single-spin nanodiamond probe," *Proceedings of the National Academy of Sciences*, vol. 110, no. 27, pp. 10894–10898, 2013.

[82] L. McGuinness, Y. Yan, A. Stacey, D. Simpson, L. Hall, D. Maclaurin, S. Prawer, P. Mulvaney, J. Wrachtrup, F. Caruso, *et al.*, "Quantum measurement and orientation tracking of fluorescent nanodiamonds inside living cells," *Nature Nanotechnology*, vol. 6, no. 6, pp. 358–363, 2011.

[83] G. Kucsko, P. Maurer, N. Y. Yao, M. Kubo, H. Noh, P. Lo, H. Park, and M. D. Lukin, "Nanometre-scale thermometry in a living cell," *Nature*, vol. 500, no. 7460, p. 54, 2013.

[84] N. Prabhakar and J. M. Rosenholm, "Nanodiamonds for advanced optical bioimaging and beyond," *Current Opinion in Colloid & Interface Science*, vol. 39,

pp. 220 – 231, 2019. Special Topic Section: Outstanding Young Researchers in Colloid and Interface Science.

[85] P. Reineck, L. F. Trindade, J. Havlik, J. Stursa, A. Heffernan, A. Elbourne, A. Orth, M. Capelli, P. Cigler, D. A. Simpson, and B. C. Gibson, "Not all fluorescent nanodiamonds are created equal: A comparative study," *Particle & Particle Systems Characterization*, vol. 36, no. 3, p. 1900009, 2019.

[86] A. Beveratos, R. Brouri, T. Gacoin, A. Villing, J.-P. Poizat, and P. Grangier, "Single photon quantum cryptography," *Phys. Rev. Lett.*, vol. 89, p. 187901, Oct 2002.

[87] I. Aharonovich, S. Castelletto, D. A. Simpson, C.-H. Su, A. D. Greentree, and S. Prawer, "Diamond-based single-photon emitters," *Reports on Progress in Physics*, vol. 74, no. 7, p. 076501, 2011.

[88] V. Petrakova, A. Taylor, I. Kratochvilova, F. Fendrych, J. Vacik, J. Kucka, J. Stursa, P. Cigler, M. Ledvina, A. Fiserova, *et al.*, "Luminescence of nanodiamond driven by atomic functionalization: Towards novel detection principles," *Advanced Functional Materials*, vol. 22, no. 4, pp. 812–819, 2012.

[89] V. Petrakova, I. Rehor, J. Stursa, M. Ledvina, M. Nesladek, and P. Cigler, "Charge-sensitive fluorescent nanosensors created from nanodiamonds," *Nanoscale*, vol. 7, pp. 12307–12311, 2015.

[90] P. Reineck, M. Capelli, D. W. M. Lau, J. Jeske, M. R. Field, T. Ohshima, A. D. Greentree, and B. C. Gibson, "Bright and photostable nitrogen-vacancy fluorescence from unprocessed detonation nanodiamond," *Nanoscale*, vol. 9, pp. 497–502, 2017.

[91] C. Laube, T. Oeckinghaus, J. Lehnert, J. Griebel, W. Knolle, A. Denisenko, A. Kahnt, J. Meijer, J. Wrachtrup, and B. Abel, "Controlling the fluorescence properties of nitrogen vacancy centers in nanodiamonds," *Nanoscale*, vol. 11, pp. 1770–1783, 2019.

[92] M. Sow, H. Steuer, S. Adekanye, L. Ginés, S. Mandal, B. Gilboa, O. A. Williams, J. M. Smith, and A. N. Kapanidis, "High-throughput nitrogen-vacancy center imaging for nanodiamond photophysical characterization and ph nanosensing," *Nanoscale*, vol. 12, no. 42, pp. 21821–21831, 2020.

[93] M. Gu, Y. Cao, S. Castelletto, B. Kouskousis, and X. Li, "Super-resolving single nitrogen vacancy centers within single nanodiamonds using a localization microscope," *Opt. Express*, vol. 21, pp. 17639–17646, Jul 2013.

[94] I. I. Vlasov, O. Shenderova, S. Turner, O. I. Lebedev, A. A. Basov, I. Sildos, M. Rähn, A. A. Shiryaev, and G. Van Tendeloo, "Nitrogen and luminescent nitrogen-vacancy defects in detonation nanodiamond," *Small*, vol. 6, no. 5, pp. 687–694, 2010.

[95] M. V. Hauf, B. Grotz, B. Naydenov, M. Dankerl, S. Pezzagna, J. Meijer, F. Jelezko, J. Wrachtrup, M. Stutzmann, F. Reinhard, and J. A. Garrido, "Chemical control of the charge state of nitrogen-vacancy centers in diamond," *Phys. Rev. B*, vol. 83, p. 081304, Feb 2011.

[96] T. Gaebel, M. Domhan, C. Wittmann, I. Popa, F. Jelezko, J. Rabeau, A. Greentree, S. Prawer, E. Trajkov, P. Hemmer, and J. Wrachtrup, "Photochromism in single nitrogen-vacancy defect in diamond," *Applied Physics B*, vol. 82, pp. 243–246, Feb 2006.

[97] J.-W. vanÂ deÂ Meent, J. Bronson, C. Wiggins, and R. Gonzalez, "Empirical bayes methods enable advanced population-level analyses of single-molecule fret experiments," *Biophysical Journal*, vol. 106, no. 6, pp. 1327 – 1337, 2014.

[98] N. Aslam, G. Waldherr, P. Neumann, F. Jelezko, and J. Wrachtrup, "Photo-induced ionization dynamics of the nitrogen vacancy defect in diamond investigated by single-shot charge state detection," *New Journal of Physics*, vol. 15, no. 1, p. 013064, 2013.

[99] P. Siyushev, H. Pinto, M. Vörös, A. Gali, F. Jelezko, and J. Wrachtrup, "Optically controlled switching of the charge state of a single nitrogen-vacancy center in diamond at cryogenic temperatures," *Phys. Rev. Lett.*, vol. 110, p. 167402, Apr 2013.

[100] L. Gines, S. Mandal, Ashek-I-Ahmed, C.-L. Cheng, M. Sow, and O. A. Williams, "Positive zeta potential of nanodiamonds," *Nanoscale*, vol. 9, pp. 12549–12555, 2017.

[101] E. Toprak, J. Enderlein, S. Syed, S. A. McKinney, R. G. Petschek, T. Ha, Y. E. Goldman, and P. R. Selvin, "Defocused orientation and position imaging (dopi) of myosin v," *Proceedings of the National Academy of Sciences*, vol. 103, no. 17, pp. 6495–6499, 2006.

[102] R. Telling, C. Pickard, M. Payne, and J. Field, "Theoretical strength and cleavage of diamond," *Physical Review Letters*, vol. 84, no. 22, p. 5160, 2000.

[103] A. S. Barnard and M. Sternberg, "Substitutional nitrogen in nanodiamond and bucky-diamond particles," *The Journal of Physical Chemistry B*, vol. 109, no. 36, pp. 17107–17112, 2005. PMID: 16853182.

[104] V. M. Acosta, E. Bauch, M. P. Ledbetter, A. Waxman, L.-S. Bouchard, and D. Budker, "Temperature dependence of the nitrogen-vacancy magnetic resonance in diamond," *Physical review letters*, vol. 104, no. 7, p. 070801, 2010.

[105] S. Karaveli, O. Gaathon, A. Wolcott, R. Sakakibara, O. A. Shemesh, D. S. Peterka, E. S. Boyden, J. S. Owen, R. Yuste, and D. Englund, "Modulation of nitrogen vacancy charge state and fluorescence in nanodiamonds using electrochemical potential," *Proceedings of the National Academy of Sciences*, vol. 113, no. 15, pp. 3938–3943, 2016.

[106] J. Han and K. Burgess, "Fluorescent indicators for intracellular ph," *Chemical Reviews*, vol. 110, no. 5, pp. 2709–2728, 2010. PMID: 19831417.

[107] P. R. Dolan, S. Adekanye, A. A. P. Trichet, S. Johnson, L. C. Flatten, Y. C. Chen, L. Weng, D. Hunger, H.-C. Chang, S. Castelletto, and J. M. Smith., "Robust, tunable, and high purity triggered single photon source at room temperature using a nitrogen-vacancy defect in diamond in an open microcavity," *Opt. Express*, vol. 26, pp. 7056–7065, Mar 2018.

[108] H. Geerts, M. De Brabander, R. Nuydens, S. Geuens, M. Moeremans, J. De Mey, and P. Hollenbeck, "Nanovid tracking: a new automatic method for the study of mobility in living cells based on colloidal gold and video microscopy," *Biophysical journal*, vol. 52, no. 5, pp. 775–782, 1987.

[109] L. Barak and W. Webb, "Diffusion of low density lipoprotein-receptor complex on human fibroblasts ," *The Journal of Cell Biology*, vol. 95, pp. 846–852, 12 1982.

[110] R. N. Ghosh and W. W. Webb, "Automated detection and tracking of individual and clustered cell surface low density lipoprotein receptor molecules," *Biophysical journal*, vol. 66, no. 5, pp. 1301–1318, 1994.

[111] V. Filipe, A. Hawe, and W. Jiskoot, "Critical evaluation of nanoparticle tracking analysis (nta) by nanosight for the measurement of nanoparticles and protein aggregates," *Pharmaceutical Research*, vol. 27, pp. 796–810, May 2010.

[112] B. Gilboa, B. Jing, T. J. Cui, M. Sow, A. Plochowietz, A. Mazumder, and A. N. Kapanidis, "Confinement-free wide-field ratiometric tracking of single fluorescent molecules," *Biophysical journal*, vol. 117, no. 11, pp. 2141–2153, 2019.

[113] R. Prakash, S. Washburn, R. Superfine, R. E. Cheney, and M. R. Falvo, "Visualization of individual carbon nanotubes with fluorescence microscopy using conventional fluorophores," *Applied Physics Letters*, vol. 83, no. 6, pp. 1219–1221, 2003.

[114] D. J. Jin, C. Cagliero, C. M. Martin, J. Izard, and Y. N. Zhou, "The dynamic nature and territory of transcriptional machinery in the bacterial chromosome," *Frontiers in microbiology*, vol. 6, 2015.

[115] K. S. Murakami and S. A. Darst, "Bacterial rna polymerases: the wholo story," *Current opinion in structural biology*, vol. 13, no. 1, pp. 31–39, 2003.

[116] O. A. Williams, J. Hees, C. Dieker, W. Jager, L. Kirste, and C. E. Nebel, "Size-dependent reactivity of diamond nanoparticles," *ACS Nano*, vol. 4, no. 8, pp. 4824–4830, 2010.

[117] N. Nunn, M. d'Amora, N. Prabhakar, A. M. Panich, N. Froumin, M. D. Torelli, I. Vlasov, P. Reineck, B. Gibson, J. M. Rosenholm, S. Giordani, and O. Shenderova, "Fluorescent single-digit detonation nanodiamond for biomedical applications," *Methods and Applications in Fluorescence*, vol. 6, p. 035010, may 2018.

[118] F. Benn, N. E. C. Haley, A. E. Lucas, E. Silvester, S. Helmi, R. Schreiber, J. Bath, and A. J. Turberfield, "Chiral dna origami nanotubes with well-defined and ad-

dressable inside and outside surfaces," *Angewandte Chemie International Edition*, vol. 57, no. 26, pp. 7687–7690, 2018.

[119] J. Ko and T. Heyduk, "Kinetics of promoter escape by bacterial RNA polymerase: effects of promoter contacts and transcription bubble collapse," *Biochemical Journal*, vol. 463, pp. 135–144, 09 2014.

[120] F. Rashid, V.-S. Raducanu, M. S. Zaher, M. Tehseen, S. Habuchi, and S. M. Hamdan, "Initial state of dna-dye complex sets the stage for protein induced fluorescence modulation," *Nature communications*, vol. 10, no. 1, pp. 1–14, 2019.

[121] O. Shenderova, S. Hens, I. Vlasov, S. Turner, Y.-G. Lu, G. Van Tendeloo, A. Schrand, S. A. Burikov, and T. A. Dolenko, "Carbon-dot-decorated nanodiamonds," *Particle & Particle Systems Characterization*, vol. 31, no. 5, pp. 580–590, 2014.

[122] A. Feklistov, B. Bae, J. Hauver, A. Lass-Napiorkowska, M. Kalesse, F. Glaus, K.-H. Altmann, T. Heyduk, R. Landick, and S. A. Darst, "Rna polymerase motions during promoter melting," *Science*, vol. 356, no. 6340, pp. 863–866, 2017.

[123] A. Alhaddad, M.-P. Adam, J. Botsoa, G. Dantelle, S. Perruchas, T. Gacoin, C. Mansuy, S. Lavielle, C. Malvy, F. Treussart, *et al.*, "Nanodiamond as a vector for sirna delivery to ewing sarcoma cells," *Small*, vol. 7, no. 21, pp. 3087–3095, 2011.

[124] F. Shi, Q. Zhang, P. Wang, H. Sun, J. Wang, X. Rong, M. Chen, C. Ju, F. Reinhard, H. Chen, J. Wrachtrup, J. Wang, and J. Du, "Single-protein spin resonance spectroscopy under ambient conditions," *Science*, vol. 347, no. 6226, pp. 1135–1138, 2015.

[125] F. Shi, F. Kong, P. Zhao, X. Zhang, M. Chen, S. Chen, Q. Zhang, M. Wang, X. Ye, Z. Wang, *et al.*, "Single-dna electron spin resonance spectroscopy in aqueous solutions," *Nature Methods*, vol. 15, no. 9, pp. 697–699, 2018.

[126] A. Plochowietz, R. Crawford, and A. N. Kapanidis, "Characterization of organic fluorophores for in vivo fret studies based on electroporated molecules," *Phys. Chem. Chem. Phys.*, vol. 16, pp. 12688–12694, 2014.

[127] M. Sustarsic, A. Plochowietz, L. Aigrain, Y. Yuzenkova, N. Zenkin, and A. Kapanidis, "Optimized delivery of fluorescently labeled proteins in live bacteria using electroporation," *Histochemistry and cell biology*, vol. 142, no. 1, pp. 113–124, 2014.

[128] A. D. Salaam, P. Hwang, R. McIntosh, H. N. Green, H.-W. Jun, and D. Dean, "Nanodiamond-dgea peptide conjugates for enhanced delivery of doxorubicin to prostate cancer," *Beilstein Journal of Nanotechnology*, vol. 5, no. 1, pp. 937–945, 2014.

[129] C.-Y. Cheng, E. Perevedentseva, J.-S. Tu, P.-H. Chung, C.-L. Cheng, K.-K. Liu, J.-I. Chao, P.-H. Chen, and C.-C. Chang, "Direct and in vitro observation of growth hormone receptor molecules in a549 human lung epithelial cells by nanodiamond labeling," *Applied physics letters*, vol. 90, no. 16, p. 163903, 2007.

[130] R. Crawford, J. Torella, L. Aigrain, A. Plochowietz, K. Gryte, S. Uphoff, and A. Kapanidis, "Long-lived intracellular single-molecule fluorescence using electroporated molecules," *Biophysical Journal*, vol. 105, no. 11, pp. 2439 – 2450, 2013.

[131] Y.-C. Chen, P. S. Salter, S. Knauer, L. Weng, A. C. Frangeskou, C. J. Stephen, S. N. Ishmael, P. R. Dolan, S. Johnson, B. L. Green, *et al.*, "Laser writing of

coherent colour centres in diamond," *Nature Photonics*, vol. 11, no. 2, pp. 77–80, 2017.

[132] K. K. Narayanasamy, J. C. Price, R. Mesquita-Riberio, M. L. Mather, and I. Jayasinghe, "Self-activated photoblinking of nitrogen vacancy centers in nanodiamonds (sandstorm): A method for rapid single molecule localization microscopy with unlimited observation time," *bioRxiv*, 2020.